8-7-2010

Efficient techniques for scattering from planar and cylindrical structures with edges

Santosh Seran

EFFICIENT TECHNIQUES FOR SCATTERING FROM PLANAR AND CYLINDRICAL STRUCTURES WITH EDGES

By

Santosh Seran

A Dissertation
Submitted to the Faculty of
Mississippi State University
in Partial Fulfillment of the Requirements
for the Degree of Doctor of Philosophy
in Electrical Engineering
in the Department of Electrical and Computer Engineering

Mississippi State, Mississippi

August 2010

EFFICIENT TECHNIQUES FOR SCATTERING FROM PLANAR AND

CYLINDRICAL STRUCTURES WITH EDGES

By

Santosh Seran

Approved:

J. Patrick Donohoe Professor of Electrical and Computer Engineering (Director of Dissertation)	Erdem Topsakal Associate Professor of Electrical and Computer Engineering (Co-Advisor)
Nicholas Younan Professor of Electrical and Computer Engineering (Committee Member)	Robert Smith Associate Professor of Mathematics (Committee Member)
James E. Fowler Professor and Director of Graduate Studies, Electrical and Computer Engineering	Sarah A. Rajala Dean of Bagley College of Engineering

Name: Santosh Seran

Date of Degree: August 7, 2010

Institution: Mississippi State University

Major Field: Electrical Engineering

Major Professor: Dr. J. Patrick Donohoe

Title of Study: EFFICIENT TECHNIQUES FOR SCATTERING FROM PLANAR AND CYLINDRICAL STRUCTURES WITH EDGES

Pages in Study: 117

Candidate for Degree of Doctor of Philosophy

In this work, we present rigorous and efficient methods for analyzing scattering from the following structures

- Tandem Slit loaded with homogeneous material
- Eccentrically loaded cylinder with multiple slits
- Semicircular cylinder and slit
- Dielectric loaded Wedge shaped cylinder
- Circular cylinder with resonant cavities and resonant cavities on circular arc.

For analyzing the material loaded tandem slit configuration, the boundary value problem is formulated into a pair of simultaneous Wiener-Hopf equations via Fourier transformation. After decoupling these equations by elementary transformation, each modified Wiener-Hopf equation is reduced to a Fredholm integral equation of the second kind. The integral equations are then solved approximately to yield the Fourier transform of the diffracted fields. The inverse transform is evaluated asymptotically to obtain the far

field expressions. Measurements and numerical simulations are also performed for several different geometric and material configurations. The analytic solutions compare well with measured and simulated results. The possibility of reducing beamwidth and increasing power coupled through the loaded tandem slit is explored.

The analysis of the eccentrically loaded cylindrical cavity with multiple slits under plane wave illumination is formulated using two distinct approaches: (1) an integral equation/combined boundary condition (IE/CBC) formulation and (2) an integral equation/Neumann series expansion (IE/NS) formulation. The IE/NS formulation is shown to converge faster than the IE/CBC formulation based on the proper edge behavior exhibited by the Neumann series current expansion functions. Results for the backscattered radar cross section (RCS) of several geometries are presented, and the relationships between the RCS and the scatterer characteristics are explored. The applicability of the Neumann series method to find a fast method for evaluating scattering from a metallic strip and semicircular cylinder is presented. The Neumann series of different periodicity is used for studying scattering from wedge shaped cylinder. The Neumann series is also applied to study scattering from a circular cylinder with resonant cavities and resonant cavities on a circular arc. These resonant cavities on a circular arc have superdirective properties, which are useful for high gain antenna design.

DEDICATION

I would like to dedicate this research to my Mother.

ACKNOWLEDGMENTS

I would like to express my deepest gratitude to my advisors Dr. J. Patrick Donohoe and Dr. Erdem Topsakal for all their support, encouragement, and exceptional guidance throughout my PhD journey. This work would not have been possible without their effort and support.

I would like to sincerely thank Dr. Nicholas Younan and Dr. Robert Smith for their valuable time and for serving on my committee. Special thanks to Dr. Robert Smith for his invigorating and highly motivating lecture on complex analysis and also for all the extra help outside the classroom.

I would also like to thank my colleagues Tutku Karacolak, Tuba Yılmaz, Travis and Ginny, the MSU Electromagnetics group for their friendship, assistance, and cooperation during this work.

I would like to thank all my roommates and friends during my PhD study, especially Vijayakrishna Dammalapati, Prabhuram Jagadeesan, and Sundarajan Srinivasan for all the love and affection they have shown during their stay and also for all the fun we had together.

TABLE OF CONTENTS

LIST OF TABLES

LIST OF FIGURES

CHAPTER I

INTRODUCTION

Investigation of diffraction characteristics of canonical structures is useful since it gives insight into new properties that can be exploited for engineering purposes. Also, theoretical investigation can be useful for validating approximate models and design "rules of thumb" that can be applied to more general problems and help in development of improved numerical techniques. Moreover, they provide a standard solution against which general numerical algorithms can be verified.

The diffraction of a plane wave by various slit configurations is an important problem in both theory and application. The tandem slit configuration has been employed in the design of microwave waveguide bandpass filters. Hamid [1] has employed the solution for the diffraction from the thick PEC edge along with the ray-optical approach to determine the reflection coefficient of the multi-cavity thick bifurcation bandpass filter. The multi-cavity thick bifurcation bandpass filter configuration is a series of tandem slits with varying slit widths and spacing. Hamid observed a reduction in bandwidth for thick slit bifurcations when compared to thin slits. This reduction in bandwidth was obtained with a small reduction in the transmission coefficient at the center frequency. The reduction in the transmission coefficient can be explained using the ray-optic approach. The multi-cavity thick bifurcation band pass filter can be considered

as a sequence of thick slits: each slit focusing electromagnetic energy on the next. One way to increase the transmission coefficient is to focus more energy on the next slit's center by reducing the beamwidth of the bifurcations. The beamwidth of the thick slit arrangement is larger than that of the equivalent thin slit for thickness to width ratios below approximately 0.5, while the thick slit beamwidth is smaller than that of the thin slit for thickness to slit ratios greater than this value [2]. The maximum thickness to width ratio used by Hamid in [1] is 0.504, yielding relatively large beamwidths for each thick slit arrangement and degrading the transmission coefficient of the filter. Kashyap [3] has also observed experimentally that the beamwidth of the thick slit is reduced by loading the slit with a dielectric material. The analysis presented here is concerned with the effect on beamwidth when the tandem slit is loaded with a dielectric material. If it is possible to reduce the tandem slit beamwidth through loading, then the thick slit bifurcations could be replaced with the loaded tandem slits to improve the filter transmission coefficient. Simultaneous analysis of the beamwidth and coupled power is required to ensure that an increase in the transmission coefficient is achieved.

The theoretical solution for diffraction from a material loaded tandem slit has not yet been explored in the available literature. Previous analysis of the tandem slit configuration includes diffraction with normal incidence by Allredge [4] using a variational procedure, diffraction with oblique incidence by Kashyap [2] using the Wiener-Hopf technique, and diffraction by a tandem impedance slit in air by Polat [5] using a combination of Wiener-Hopf and mode matching techniques. The analysis of thick tandem slits with offset has been considered by Kiang [6] for penetration studies. Earlier analysis of diffraction by a dielectric loaded single slit has been carried out using

the method of moments [7], dual integral equations [8] and the finite element and boundary integral methods [9]. Diffraction by an open-ended waveguide with extended loading is solved using the Wiener-Hopf technique by Fong [10] and diffraction by a dielectric-loaded slit in a conducting plane is solved by Hurd and Sachdeva using the integral equation method [11]. The problem considered here is diffraction by a tandem slit loaded with a homogeneous dielectric material which is solved using the Wiener-Hopf technique [12]. The formulation for the material loaded tandem slit and numerical results for the transmission coefficient and beamwidth are presented in CHAPTER II.

Electromagnetic field penetration through longitudinal slots in cylindrical geometries has received considerable attention in the literature given the importance of this geometry with regard to electromagnetic compatibility and RCS reduction. The problem of a single slit on a coaxial cable was solved for both TE and TM illumination by Ziolkowski [19] using the dual series approach. Felsen solved the same problem for the TE case using ray-mode parameterization [20], while Arvas solved the problem for TM illumination using the method of moments (MoM) [21]. Yu [22] considered TM illumination of the coaxial geometry with a thick outer boundary by matching the field at the boundary and using the orthogonality of the Fourier series. The scattered fields of a cylinder with a slit were determined in [23] and [24] by incorporating a modal expansion of the aperture fields in the MoM solution. Also, Shumpert and Bulter proposed three methods to study penetration of a slotted conducting cylinder in [25] and [26]. The slotted cylinder with inner and outer lossy coating has been analyzed by Colak in [27] and [28].

In this work, we consider scattering by a loaded cylindrical cavity with multiple longitudinal slits in the outer conductor and an eccentrically located inner conductor. The analysis of the structure using two distinct techniques (Combined boundary condition and Neumann series) is presented in CHAPTER III. The advantage of using Neumann series is that it satisfies the required edge condition along with the boundary condition on the metallic surface. The extension of the Neumann series for the analysis of a thin metallic strip and a semicircular cylinder is presented in CHAPTER IV. The Neumann series method in conjunction with field expansions on the Riemann surface is used to find scattering from a strip. The geometry of a metallic wedge shaped cylinder is also addressed using Neumann series expansion for the field expansions under different periodicity. The analysis of the thin strip and wedge shaped geometry are presented in CHAPTER V. The analysis of resonant cavities on a circular strip is presented in CHAPTER VI.

CHAPTER II

SCATTERING FROM DIELECTRIC LOADED TANDEM SLIT

2.1 Introduction

In this chapter, we analyze the problem of scattering from the material loaded tandem slit using Wiener-Hopf. The Wiener-Hopf formulation of the material loaded tandem slit is described in Section 2.2. The method to solve the Wiener-Hopf equation for the scattered far field is described in Section 2.3. Numerical results for beamwidth and normalized power coupled are presented in Section 2.4.

2.2 Formulation of the Problem

Consider the two-dimensional problem of a material loaded tandem slit as shown in Figure 2.1. The tandem slit is formed by two infinitesimally thin PEC layers covering the planes at $y = +d$ and $y = -d$ with open slits of length l in each plane. The region between the two PEC planes, designated as region 2 ($-d < y < d$), is filled with a homogeneous material of thickness $2d$ while the surrounding medium is free space. The incident plane wave, polarized parallel to the slit edges, is incident from above in region 1 ($y > d$) at an angle ϕ_o. The region on the opposite side of the tandem slit is designated as region 3 ($y < -d$).

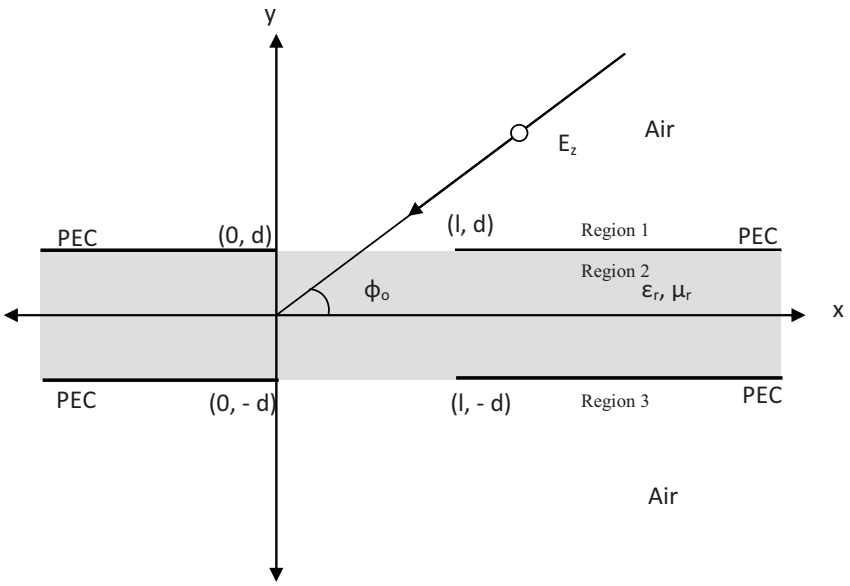

Figure 2.1. Material loaded tandem slit

The Wiener-Hopf solution of the loaded tandem slit is formulated as a boundary value problem. Using appropriate spectral representations for the fields, the boundary value problem is reduced to a pair of simultaneous modified Wiener-Hopf equations. The general form of the modified Wiener-Hopf equation of the second kind is

$$\Psi_-(\alpha) + X(\alpha) + \Psi_+(\alpha)e^{j\alpha l} = \frac{-Y_1(\alpha)}{M(\alpha)} \tag{2.1}$$

The $\Psi_-(\alpha)$, $\Psi_+(\alpha)$ and $Y_1(\alpha)$ functions are unknown, while $X(\alpha)$ and $M(\alpha)$ are known functions. In the above equation, as well as throughout the paper, a subscript of "+" denotes a function which is regular in the upper half-plane [$\mathrm{Im}(\alpha) > \mathrm{Im}(-k_o)$] while a subscript "-" denotes a function which is regular in the lower half-plane [$\mathrm{Im}(\alpha) < \mathrm{Im}(k_o)$], where '$k_o$' is the free space wave number. "Re" and "Im" are used to denote the real and imaginary parts of complex quantities. Functions that are regular over the entire complex plane except the point at infinity are denoted by the subscript "0". The next step is to

decompose the terms in Eq. (2.1) such that each function is analytic either on the upper half plane or the lower-half plane. The decomposition is performed using the Cauchy integral formula for analytic functions. The functions which are analytic on the upper or lower half-plane are bounded in the respective region, since they tend to zero as α tends to infinity. In some cases, the functions must be manipulated to meet the requirement of tending to zero at infinity. This yields a function which is analytic in the upper half-plane equal to a function analytic in the lower half-plane with a region of overlap [-Im(k_o) < α < Im(k_o)]. By the uniqueness theorem for analytic functions, this represents a function which is analytic in the entire complex domain (entire function). Also, this entire function is bounded, and by Liouville's theorem, the entire function is a constant (equal to zero since the analytic function tends to zero at infinity), which yields a pair of coupled integral equations that can be decoupled by elementary transformation to the Fredholm integral equation. The solution of the Fredholm integral equation is obtained approximately by a method used by Jones [13]. The Fourier transform pair used here is defined by

$$\hat{u}(\alpha) = \frac{1}{\sqrt{2\pi}} \int_{-\infty}^{\infty} u(x) e^{j\alpha x} dx \tag{2.2}$$

$$u(x) = \frac{1}{\sqrt{2\pi}} \int_{-\infty}^{\infty} \hat{u}(\alpha) e^{-j\alpha x} dx. \tag{2.3}$$

where the "^" denotes the Fourier transform of the function. The time dependence employed here is $e^{-j\omega t}$.

The TM polarized incident plane is defined by

$$E_z^i = u^i(x,y) = e^{-jk_o(x\cos\phi_o + y\sin\phi_o)} \tag{2.4}$$

Given the structure of the tandem slit and the characteristics of the incident wave, the total electric field has only a *z*-component, allowing a scalar boundary value problem solution. The total electric field in the three distinct regions can be written as

$$u(x,y)=\begin{pmatrix} u_1(x,y)+e^{-jk_o x\cos\phi_o}\left(e^{jk_o y\sin\phi_o}-e^{jk_o(y-2d)\sin\phi_o}\right) & \text{region 1} \\ u_2(x,y) & \text{region 2} \\ u_3(x,y) & \text{region 3} \end{pmatrix} \tag{2.5}$$

The functions $u_1(x,y)$, $u_2(x,y)$ and $u_3(x,y)$ must satisfy Helmholtz's equation for the respective media subject to the following boundary, continuity, edge and radiation conditions:

$$u_1(x,d)=u_2(x,\pm d)=u_3(x,-d)=0 \qquad x\in\{(-\infty,0)\bigcup(l,\infty)\} \tag{2.6}$$

$$u_1(x,d)=u_2(x,d),\;\; u_2(x,-d)=u_3(x,-d) \qquad x\in(0,l) \tag{2.7}$$

$$\frac{\partial u_1(x,d)}{\partial y}-\frac{1}{\mu_r}\frac{\partial u_2(x,d)}{\partial y}=jhe^{-jk_o x\cos\phi_o} \qquad x\in(0,l) \tag{2.8}$$

$$\frac{1}{\mu_r}\frac{\partial u_2(x,-d)}{\partial y}-\frac{\partial u_3(x,-d)}{\partial y}=0 \qquad x\in(0,l) \tag{2.9}$$

$$\frac{\partial u_n(0,d)}{\partial y},\frac{\partial u_n(l,d)}{\partial y}=O(\rho^{-\tau}) \qquad \rho\to 0 \qquad n=1,2 \tag{2.10}$$

$$\frac{\partial u_n(0,-d)}{\partial y},\frac{\partial u_n(l,-d)}{\partial y}=O(\rho^{-\tau}) \qquad \rho\to 0 \qquad n=1,2 \tag{2.11}$$

$$\sqrt{\rho}\left[\frac{\partial u_n}{\partial\rho}-jk_o u_n\right]\to 0 \qquad \rho\to 0 \qquad n=1,3 \tag{2.12}$$

$$\sqrt{\rho}\left[\frac{\partial u_2}{\partial\rho}-jku_2\right]\to 0 \qquad \rho\to 0 \tag{2.13}$$

where

$$h=2k_o\sin\phi_o e^{-jk_o d\sin\phi_o}$$

and $0 < \tau < 1/2$, depending on the medium. Taking the Fourier transform of the Helmholtz equation with respect to x yields the following solution in the transformed domain

$$\hat{u}_1(\alpha, y) = A(\alpha)e^{jK_0(\alpha)y} \tag{2.14}$$

$$\hat{u}_2(\alpha, y) = B(\alpha)e^{jK(\alpha)y} + C(\alpha)e^{-jK(\alpha)y} \tag{2.15}$$

$$\hat{u}_3(\alpha, y) = D(\alpha)e^{-jK_0(\alpha)y} \tag{2.16}$$

where $K_o(\alpha) = \sqrt{k_0{}^2 - \alpha^2}$, $K(\alpha) = \sqrt{k^2 - \alpha^2}$ and 'k' is the wave number of the material between the slits. The branch cut for $K_o(\alpha)$ is shown in Figure 2.2. The functions A(α), B(α) and C(α) are the unknown spectral coefficients to be determined. The branch cut for K(α) is shown in Figure 2.2. The transform solutions in Eqs (2.14), (2.15), and (2.16) can each be written as a sum of terms analytic in the upper half-plane, the lower half-plane and the entire plane such that

$$\hat{u}_1(\alpha, y) = F_-(\alpha, y) + F_0(\alpha, y) + F_+(\alpha, y)e^{j\alpha l} \tag{2.17}$$

$$\hat{u}_2(\alpha, y) = G_-(\alpha, y) + G_0(\alpha, y) + G_+(\alpha, y)e^{j\alpha l} \tag{2.18}$$

$$\hat{u}_3(\alpha, y) = H_-(\alpha, y) + H_0(\alpha, y) + H_+(\alpha, y)e^{j\alpha l} \tag{2.19}$$

where

$$\begin{bmatrix} F_-(\alpha, y) \\ G_-(\alpha, y) \\ H_-(\alpha, y) \end{bmatrix} = \frac{1}{\sqrt{2\pi}} \int_{-\infty}^{0} \begin{bmatrix} u_1(\alpha, y) \\ u_2(\alpha, y) \\ u_3(\alpha, y) \end{bmatrix} e^{j\alpha x} dx, \tag{2.20}$$

$$\begin{bmatrix} F_+(\alpha,y) \\ G_+(\alpha,y) \\ H_+(\alpha,y) \end{bmatrix} = \frac{1}{\sqrt{2\pi}} \int_l^{\infty} \begin{bmatrix} u_1(\alpha,y) \\ u_2(\alpha,y) \\ u_3(\alpha,y) \end{bmatrix} e^{j\alpha(x-l)} dx \tag{2.21}$$

$$\begin{bmatrix} F_0(\alpha,y) \\ G_0(\alpha,y) \\ H_0(\alpha,y) \end{bmatrix} = \frac{1}{\sqrt{2\pi}} \int_0^{l} \begin{bmatrix} u_1(\alpha,y) \\ u_2(\alpha,y) \\ u_3(\alpha,y) \end{bmatrix} e^{i\alpha x} dx \,. \tag{2.22}$$

Combining the boundary conditions of Eq. (2.6) and (2.7) with the expressions in (2.14) and (2.15) gives

$$G_0(\alpha,d) = B(\alpha)e^{jK(\alpha)d} + C(\alpha)e^{-jK(\alpha)d} = F_0(\alpha,d) = A(\alpha)e^{jK_0(\alpha)d}\,, \tag{2.23}$$

$$G_0(\alpha,-b) = B(\alpha)e^{-jK(\alpha)d} + C(\alpha)e^{jK(\alpha)d} = H_0(\alpha,-d) = D(\alpha)e^{jK_0(\alpha)d} \tag{2.24}$$

Solving Eq. (2.23) and (2.24) for B(α) and C(α) yields

$$B(\alpha) = e^{jK_0(\alpha)d}\left(\frac{A(\alpha)e^{jK(\alpha)d} - D(\alpha)e^{-jK(\alpha)d}}{2jSin(2K(\alpha)d)}\right) \tag{2.25}$$

$$C(\alpha) = e^{jK_0(\alpha)d}\left(\frac{D(\alpha)e^{jK(\alpha)d} - A(\alpha)e^{-jK(\alpha)d}}{2jSin(2K(\alpha)d)}\right) \tag{2.26}$$

Differentiating Eq. (2.17) and (2.18) with respect to *y*, inserting the results into the boundary condition of Eq. (2.8) and (2.9), and adding the resulting equations yields

$$\Psi_{1-}(\alpha) + \frac{h[e^{jl(\alpha-k\cos\phi)} - 1]}{\sqrt{2\pi}(\alpha - k\cos\phi)} + \Psi_{1+}(\alpha)e^{j\alpha l} = \frac{-D_1(\alpha)}{L(\alpha)} \tag{2.27}$$

where

$$L(\alpha) = \frac{\mu_r \sin(K(\alpha)d)}{-jK_0(\alpha)\mu_r \sin(K(\alpha)d) + K(\alpha)\cos(K(\alpha)d)}\,, \tag{2.28}$$

$$D_1(\alpha) = F_0(\alpha,d) - H_0(\alpha,-d)\,, \tag{2.29}$$

$$\Psi_{1-}(\alpha) = \overset{\circ}{H}_{-}(\alpha,-d) + \overset{\circ}{F}_{-}(\alpha,d) - \frac{1}{\mu_r}\left(\overset{\circ}{G}_{-}(\alpha,d) + \overset{\circ}{G}_{-}(\alpha,-d) \right) \tag{2.30}$$

$$\Psi_{1+}(\alpha) = \overset{\circ}{H}_{+}(\alpha,-d) + \overset{\circ}{F}_{+}(\alpha,d) - \frac{1}{\mu_r}\left(\overset{\circ}{G}_{+}(\alpha,d) + \overset{\circ}{G}_{+}(\alpha,-d) \right). \tag{2.31}$$

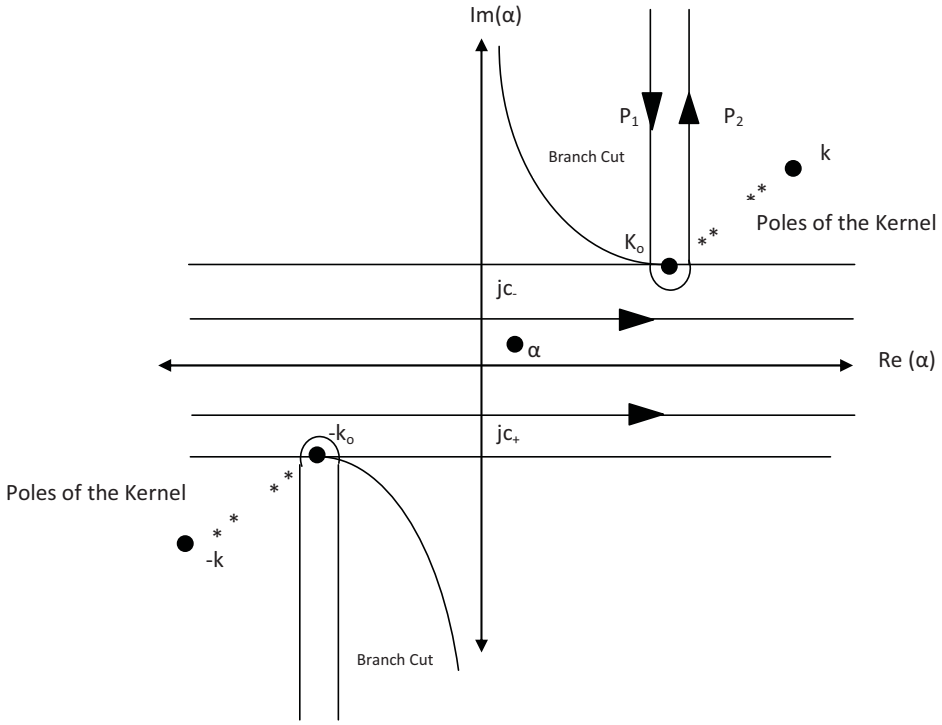

Figure 2.2. Complex α-plane and integration contour.

The dot above the functions in (2.30) and (2.31) denotes a differentiation with respect to *y*. Similarly, differentiating Eq. (2.17) and (2.19) with respect to *y*, inserting the results into boundary conditions Eq. (2.8) and (2.9) and subtracting the resulting equation yields

$$\Psi_{2-}(\alpha) + \frac{h[e^{jl(\alpha - k_o\cos\phi_o)} - 1]}{\sqrt{2\pi}(\alpha - k_o\cos\phi_o)} + \Psi_{2+}(\alpha)e^{j\alpha l} = \frac{-S_1(\alpha)}{M(\alpha)} \tag{2.32}$$

where

$$M(\alpha) = \frac{\mu_r \cos(K(\alpha)d)}{-K(\alpha)\sin(K(\alpha)d) - j\mu_r K_0(\alpha)\cos(K(\alpha)d)}, \tag{2.33}$$

$$S_1(\alpha) = F_0(\alpha, d) + H_0(\alpha, -d), \tag{2.34}$$

$$\Psi_{2-}(\alpha) = \overset{\circ}{F}_-(\alpha, d) - \overset{\circ}{H}_-(\alpha, -d) - \frac{1}{\mu_r}\left(\overset{\circ}{G}_-(\alpha, d) - \overset{\circ}{G}_-(\alpha, -d)\right) \tag{2.35}$$

and

$$\Psi_{2+}(\alpha) = \overset{\circ}{F}_+(\alpha, d) - \overset{\circ}{H}_+(\alpha, -d) - \frac{1}{\mu_r}\left(\overset{\circ}{G}_+(\alpha, d) - \overset{\circ}{G}_+(\alpha, -d)\right). \tag{2.36}$$

Eqs (2.27) and (2.32) are modified Wiener-Hopf equations of the second kind. Given a solution to the first equation, the similar form of the two equations allows for a simple substitution of functions to obtain the solution to the second equation.

2.3 Approximate Solution of the Wiener-Hopf Equation

The first step in the solution process of the Wiener-Hopf equation in (2.27) is to factorize the kernel. The factorization of the kernel is given in APPENDIX A. Multiplying equation (2.27) by $L_+(\alpha)e^{-j\alpha l}$ and applying the well known decomposition theorem [12] yields

$$\begin{aligned}
&\frac{1}{2\pi j}\int_{-\infty-jc_+}^{\infty-jc_+} \frac{\Psi_{1-}(\tau)L_+(\tau)e^{-j\tau l}d\tau}{(\tau-\alpha)} + \frac{he^{-jk_o l\cos\phi_o}[L_+(\alpha) - L_+(k_o\cos\phi_o)]}{\sqrt{2\pi}(\alpha - k_o\cos\phi_o)} \\
&-\frac{h}{2\pi j}\int_{-\infty-jc_+}^{\infty-jc_+} \frac{e^{-j\tau l}L_+(\tau)d\tau}{\sqrt{2\pi}(\tau - k_o\cos\phi_o)(\tau-\alpha)} + \Psi_{1+}(\alpha)L_+(\alpha) = -\frac{D_1(\alpha)e^{-j\alpha l}}{L_-(\alpha)} \\
&+\frac{1}{2\pi j}\int_{-\infty+jc_-}^{\infty+jc_-} \frac{\Psi_{1-}(\tau)L_+(\tau)e^{-j\tau l}d\tau}{(\tau-\alpha)} - \frac{he^{-jk_o l\cos\phi_o}L_+(k_o\cos\phi_o)}{\sqrt{2\pi}(\alpha - k_o\cos\phi_o)} \\
&-\frac{h}{2\pi j}\int_{-\infty+jc_-}^{\infty+jc_-} \frac{e^{-j\tau l}L_+(\tau)d\tau}{\sqrt{2\pi}(\tau - k_o\cos\phi_o)(\tau-\alpha)}
\end{aligned} \tag{2.37}$$

The functions on the left hand side of (2.37) are regular in the upper half-plane [Im(α) > Im(-k_o)], while those on the right-hand side are regular in the lower half-plane [Im(α) < Im($k_o$cosφ$_o$)]. By analytic continuation, the two sides of (2.37) define an entire function. Also, the function is bounded and tends to zero at infinity. Hence, by Liouville's theorem, the entire function is identically equal to zero, and we can write

$$\frac{1}{2\pi j}\int_{-\infty+jc_+}^{\infty+jc_+}\frac{\Psi_{1-}(\tau)L_+(\tau)e^{-j\tau l}d\tau}{(\tau-\alpha)}+\frac{he^{-jk_ol\cos\phi_o}[L_+(\alpha)-L_+(k_o\cos\phi_o)]}{\sqrt{2\pi}(\alpha-k_o\cos\phi_o)} \\ -\frac{h}{2\pi j}\int_{-\infty+jc_+}^{\infty+jc_+}\frac{e^{-j\tau l}L_+(\tau)d\tau}{\sqrt{2\pi}(\tau-k_o\cos\phi_o)(\tau-\alpha)}+\Psi_{1+}(\alpha)L_+(\alpha)=0 \tag{2.38}$$

Multiplying (2.27) by L$_-$(α) and implementing the same procedure as above yields

$$\Psi_{1-}(\alpha)L_-(\alpha)-\frac{he^{-jk_ol\cos\phi_o}}{2\pi j\sqrt{2\pi}}\int_{-\infty+jc_-}^{\infty+jc_-}\frac{L_-(\tau)e^{j\tau l}d\tau}{(\tau-\alpha)(\tau-k_o\cos\phi_o)} \\ -\frac{hL_-(\alpha)}{\sqrt{2\pi}(\alpha-k_o\cos\phi_o)}-\frac{1}{2\pi j}\int_{-\infty+jc_-}^{\infty+jc_-}\frac{e^{j\tau l}L_-(\tau)\Psi_{1+}(\tau)d\tau}{(\tau-\alpha)}=0 \tag{2.39}$$

Following the procedure outlined in [12], we substitute τ=-τ in (2.38) and α = -α in (2.39) and add and subtract the resulting equations, yielding

$$F_+^*(\alpha)L_+(\alpha)-\frac{he^{-jk_ol\cos\phi_o}L_+(k_o\cos\phi_o)}{\sqrt{2\pi}(\alpha-k_o\cos\phi_o)}+\frac{\lambda}{2\pi j}\int_{-\infty+ja}^{\infty+ja}\frac{F_+^*(\tau)L_-(\tau)e^{j\tau l}d\tau}{(\tau+\alpha)}=0 \tag{2.40}$$

where

$$F_+^*(\alpha)=F_+(\alpha)+\frac{he^{-jk_ol\cos\phi_o}}{\sqrt{2\pi}(\alpha-k_o\cos\phi_o)}-\frac{\lambda h}{\sqrt{2\pi}(\alpha+k_o\cos\phi_o)}, \tag{2.41}$$

$$F_+(\alpha)=\begin{cases}\Psi_{1+}(\alpha)+\Psi_{1-}(-\alpha);\lambda=-1\\ \Psi_{1+}(\alpha)-\Psi_{1-}(-\alpha);\lambda=1\end{cases} \tag{2.42}$$

and

$$c_-=-c_+=a. \tag{2.43}$$

The approximate evaluation of the integral in equation (2.40) for large l is given in APPENDIX B. The approximate evaluation of the integral equation introduces approximation in the solution for spectral components. Substituting the integral result into (2.40) gives

$$
\begin{aligned}
&F_+(\alpha)L_+(\alpha)+\frac{he^{-jk_ol\cos\phi_o}L_+(\alpha)}{\sqrt{2\pi}(\alpha-k_o\cos\phi_o)}-\frac{\lambda hL_+(\alpha)}{\sqrt{2\pi}(\alpha+k_o\cos\phi_o)}\\
&-\frac{he^{-jk_ol\cos\phi_o}L_+(k_o\cos\phi_o)}{\sqrt{2\pi}(\alpha-k_o\cos\phi_o)}-\frac{\lambda^2h}{\sqrt{2\pi}}\sum_{n=1}^{p}\frac{\mathrm{Re}\,s\{L_-(s_n)\}e^{js_nl}}{(s_n+k_o\cos\phi_o)(s_n+\alpha)}\\
&+\frac{\lambda^2h{\mu_r}^2e^{jk_ol}e^{j\pi/4}}{\pi\sqrt{2\pi}L_+(k_o)(\alpha-k_o\cos\phi_o)}\left[\int_0^\infty\frac{e^{-ul}u^{1/2}\sqrt{2k_o+ju}\,du}{(k_o+ju+k_o\cos\phi_o)A(u)}-\right.\\
&\left.\int_0^\infty\frac{e^{-ul}u^{1/2}\sqrt{2k_o+ju}\,du}{(k_o+ju+\alpha)A(u)}\right]\\
&+\frac{\lambda hL_-(k_o\cos\phi_o)}{\sqrt{2\pi}(\alpha+k_o\cos\phi_o)}+\frac{\lambda he^{-jk_ol\cos\phi_o}}{\sqrt{2\pi}}\sum_{n=1}^{p}\frac{\mathrm{Re}\,s\{L_-(s_n)\}e^{js_nl}}{(s_n-k_o\cos\phi_o)(s_n+\alpha)}\\
&-\frac{\lambda h{\mu_r}^2e^{-jk_ol\cos\phi_o}e^{jk_ol}e^{j\pi/4}}{\pi\sqrt{2\pi}L_+(k_o)(\alpha+k_o\cos\phi_o)}\left[\int_0^\infty\frac{e^{-ul}u^{1/2}\sqrt{2k_o+ju}\,du}{(k_o+ju-k_o\cos\phi_o)A(u)}\right.\\
&\left.-\int_0^\infty\frac{e^{-ul}u^{1/2}\sqrt{2k_o+ju}\,du}{(k_o+ju+\alpha)A(u)}\right]\\
&+\lambda\sum_{n=1}^{p}\frac{F_+(s_n)\,\mathrm{Re}\,s\{L_-(s_n)\}e^{js_nl}}{(\alpha+s_n)}\\
&-\frac{\lambda F_+(k_o){\mu_r}^2e^{jk_ol}e^{j\pi/4}}{\pi L_+(k_o)}\int_0^\infty\frac{e^{-ul}u^{1/2}\sqrt{2k_o+ju}\,du}{(k_o+ju+\alpha)A(u)}=0
\end{aligned}
\tag{2.44}
$$

The unknown functions $\Psi_{1+}(\alpha)$ and $\Psi_{1-}(\alpha)$ are obtained by substituting $\lambda=+1$ and $\lambda=-1$ into (2.44) and adding and subtracting the resulting equations. Equation (2.32) is manipulated in the same way as (2.27) by replacing $L(\alpha)$ with $M(\alpha)$ and $A(\alpha)$ with $A_1(\alpha)$, where

$$A_1(u) = -\mu_r{}^2 ju(2k_o + ju) + [k^2 - (k_o + ju)^2]\tan^2(b\sqrt{k^2 - (k_o + ju)^2}) \tag{2.45}$$

The unknown functions $\Psi_{2+}(\alpha)$ and $\Psi_{2-}(\alpha)$ are obtained by substituting $\lambda = +1$ and $\lambda = -1$ into the equation corresponding to (2.44) and adding and subtracting the results. From these results, the diffracted field in region 3 ($y < -d$) may be written as

$$\begin{aligned} u_3(x,y) &= \frac{1}{2\sqrt{2\pi}} \int_\Gamma [S_1(\alpha) - D_1(\alpha)]\, e^{-jK_0(\alpha)(y+b) - j\alpha x} d\alpha \\ &= u_{31}(x,y) + u_{32}(x,y) \end{aligned} \tag{2.46}$$

where Γ is the straight line lying in the strip $-\mathrm{Im}(k_o\cos\varphi_o) < \mathrm{Im}(\alpha) < \mathrm{Im}(k_o\cos\varphi_o)$. The evaluation of the integrals in Equation (2.46) via the saddle point method yields

$$
\begin{aligned}
u_{31}(r,\phi) = \frac{1}{2}\sqrt{\frac{k_0}{r}}e^{j(k_o r-\pi/4)}\sin\phi\Bigg\{ & \frac{hL_-(k_o\cos\phi_o)L_-(k_o\cos\phi)}{\sqrt{2\pi}k_o(\cos\phi+\cos\phi_o)} \\
& - \frac{hM_-(k_o\cos\phi_o)M_-(k_o\cos\phi)}{\sqrt{2\pi}k_o(\cos\phi+\cos\phi_o)} \\
& + \frac{he^{-jk_o l\cos\phi_o}L_-(k_o\cos\phi)}{\sqrt{2\pi}}\sum_{n=1}^{p}\frac{\mathrm{Re}\,s\{L_-(s_n)\}e^{js_n l}}{(s_n-k_o\cos\phi_o)(s_n+k_o\cos\phi)} \\
& - \frac{he^{-jk_o l\cos\phi_o}M_-(k_o\cos\phi)}{\sqrt{2\pi}}\sum_{n=1}^{q}\frac{\mathrm{Re}\,s\{M_-(r_n)\}e^{jr_n l}}{(r_n-k_o\cos\phi_o)(r_n+k_o\cos\phi)} \\
& - \frac{h\mu_r^2 e^{-jk_o l\cos\phi_o}e^{jk_o l}e^{j\pi/4}L_-(k_o\cos\phi)}{\pi\sqrt{2\pi}k_o L_+(k_o)(\cos\phi+\cos\phi_o)}\left[T(-k_o\cos\phi_o)-T(k_o\cos\phi)\right] \\
& + \frac{h\mu_r^2 e^{-jk_o l\cos\phi_o}e^{jk_o l}e^{j\pi/4}M_-(k_o\cos\phi)}{\pi\sqrt{2\pi}k_o M_+(k_o)(\cos\phi+\cos\phi_o)}\left[T_1(-k_o\cos\phi_o)-T_1(k_o\cos\phi)\right] \\
& + L_-(k_o\cos\phi)\sum_{n=1}^{p}\frac{\left[F_+^1(s_n)\Big|_{\lambda=1}+F_+^1(s_n)\Big|_{\lambda=-1}\right]\mathrm{Re}\,s\{L_-(s_n)\}e^{js_n l}}{2(s_n+k_o\cos\phi)} \\
& - M_-(k_o\cos\phi)\sum_{n=1}^{q}\frac{\left[F_+^2(r_n)\Big|_{\lambda=1}+F_+^2(r_n)\Big|_{\lambda=-1}\right]\mathrm{Re}\,s\{M_-(r_n)\}e^{jr_n l}}{2(r_n+k_o\cos\phi)} \\
& - \frac{\left[F_+^1(k_o)\Big|_{\lambda=1}+F_+^1(k_o)\Big|_{\lambda=-1}\right]\mu_r^2 e^{jk_o l}e^{j\pi/4}L_-(k_o\cos\phi)\,T(k_o\cos\phi)}{2\pi\,L_+(k_o)} \\
& + \frac{\left[F_+^2(k_o)\Big|_{\lambda=1}+F_+^2(k_o)\Big|_{\lambda=-1}\right]\mu_r^2 e^{jk_o l}e^{j\pi/4}M_-(k_o\cos\phi)T_1(k_o\cos\phi)}{2\pi\,M_+(k_o)}\Bigg\}
\end{aligned}
\tag{2.47}
$$

and

$$
\begin{aligned}
u_{32}(r,\phi) &= \frac{1}{2}\sqrt{\frac{k_o}{r}}e^{j(k_o r-\pi/4)}\sin\phi\times \\
&\left\{ e^{-jk_o l(\cos\phi+\cos\phi_o)}\,\frac{hM_+(k_o\cos\phi_o)M_+(k_o\cos\phi)}{\sqrt{2\pi}k_o(\cos\phi+\cos\phi_o)}\right. \\
&- e^{-jk_o l(\cos\phi+\cos\phi_o)}\,\frac{hL_+(k_o\cos\phi_o)L_+(k_o\cos\phi)}{\sqrt{2\pi}k_o(\cos\phi+\cos\phi_o)} \\
&+ \frac{he^{-jk_o l\cos\phi}L_+(k_o\cos\phi)}{\sqrt{2\pi}}\sum_{n=1}^{p}\frac{\mathrm{Re}\,s\{L_-(s_n)\}e^{js_n l}}{(s_n+k_o\cos\phi_o)(s_n-k_o\cos\phi)} \\
&- \frac{he^{-jk_o l\cos\phi}M_+(k_o\cos\phi)}{\sqrt{2\pi}}\sum_{n=1}^{q}\frac{\mathrm{Re}\,s\{M_-(r_n)\}e^{jr_n l}}{(r_n+k_o\cos\phi_o)(r_n-k_o\cos\phi)} \\
&+ \frac{h\mu_r^2 e^{-jk_o l\cos\phi}e^{jk_o l}e^{j\pi/4}L_+(k_o\cos\phi)}{\pi\sqrt{2\pi}k_o L_+(k_o)(\cos\phi+\cos\phi_o)}\left[T(k_o\cos\phi_o)-T(-k_o\cos\phi)\right] \\
&- \frac{h\mu_r^2 e^{-jk_o l\cos\phi}e^{jk_o l}e^{j\pi/4}M_+(k_o\cos\phi)}{\pi\sqrt{2\pi}k_o M_+(k_o)(\cos\phi+\cos\phi_o)}\left[T_1(k_o\cos\phi_o)-T_1(-k_o\cos\phi)\right] \\
&- e^{-jk_o l\cos\phi}L_+(k_o\cos\phi)\times \\
&\sum_{n=1}^{p}\frac{\left[F_+^1(s_n)\Big|_{\lambda=1}-F_+^1(s_n)\Big|_{\lambda=-1}\right]\mathrm{Re}\,s\{L_-(s_n)\}e^{js_n l}}{2(s_n-k_o\cos\phi)} \\
&+ e^{-jk_o l\cos\phi}M_+(k_o\cos\phi)\times \\
&\sum_{n=1}^{q}\frac{\left[F_+^2(r_n)\Big|_{\lambda=1}-F_+^2(r_n)\Big|_{\lambda=-1}\right]\mathrm{Re}\,s\{M_-(r_n)\}e^{jr_n l}}{2(r_n-k_o\cos\phi)} \\
&+ \mu_r^2 e^{jk_o l}e^{j\pi/4}L_+(k_o\cos\phi)\,T(-k_o\cos\phi)\times \\
&\frac{e^{-jk_o l\cos\phi}\left[F_+^1(k_o)\Big|_{\lambda=1}-F_+^1(k_o)\Big|_{\lambda=-1}\right]}{2\pi L_+(k_o)} \\
&- \mu_r^2 e^{jk_o l}e^{j\pi/4}M_+(k_o\cos\phi)T_1(-k_o\cos\phi)\times \\
&\left.\frac{e^{-jk_o l\cos\phi}\left[F_+^2(k_o)\Big|_{\lambda=1}-F_+^2(k_o)\Big|_{\lambda=-1}\right]}{2\pi M_+(k_o)}\right\}
\end{aligned}
\tag{2.48}
$$

where

$$T(x) = \int_0^{\infty} \frac{e^{-ul} u^{1/2} \sqrt{2k_0 + ju}}{(k_0 + ju + x) A(u)} du \,, \tag{2.49}$$

$$T_1(x) = \int_0^{\infty} \frac{e^{-ul} u^{1/2} \sqrt{2k_0 + ju}}{(k_0 + ju + x) A_1(u)} du \,, \tag{2.50}$$

$$x = r\cos\phi \tag{2.51}$$

and

$$y + d = -r\sin\phi \,. \tag{2.52}$$

The first two terms of u_{31} and u_{32} correspond to the primary diffracted field mentioned by Kashyap [3], while the remaining expressions represent the interaction terms. The 3rd, 4th, 7th, and 8th terms in the u_{31} and u_{32} expressions of (2.47) and (2.48) are dependent on the residues of the kernel function [L (α) and M (α)] and correspond to modes excited within the dielectric media of the loaded tandem slit. Thus, these terms go to zero for the unloaded tandem slit.

2.4 Numerical Results

The Wiener-Hopf solution for the loaded tandem slit is compared to a 2D numerical simulation using *FastFDTD* [14] and experimental measurements for validation purposes. The test article consists of a tandem slit in two parallel, thin PEC layers covering both sides of a dielectric plate of finite area as shown in Figure 2.3. A double-side copper coated sheet of FR4 was utilized for the experimental measurements (width = 457mm, height = 305mm, dielectric thickness =1.3mm) with a centered tandem slit (width = 60mm, height = 240mm). Measurements are made at 10 GHz, using the system arrangement shown in Figure 2. 4. Note that the width of the slit is $2\lambda_o$ at 10 GHz.

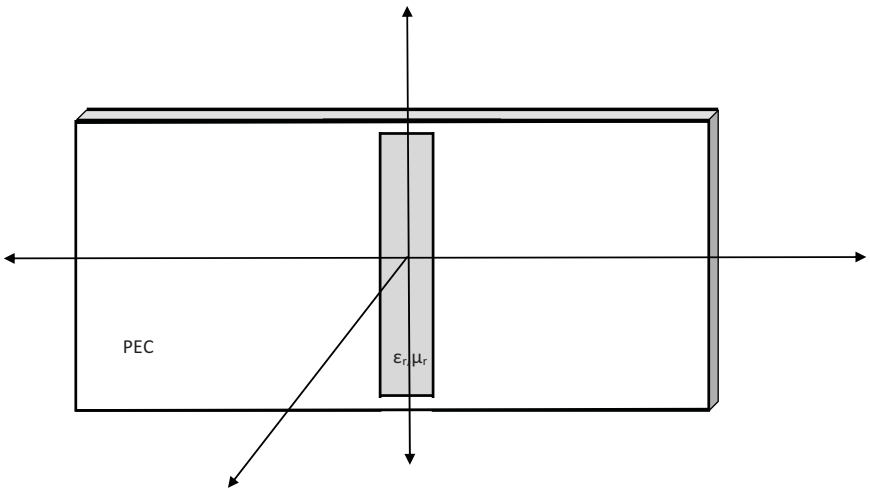

Figure 2.3. Geometry of the FR4 sheet used for loaded tandem slit measurements.

The transmitting and receiving antennas are identical X-band horns (aperture = 7cm x 4.9cm, half-power beamwidth = 31°) connected to an Agilent E8362B network analyzer. The receiving antenna was placed on a rotating arm of calibrated scale at a distance of $15\lambda_o$ from the loaded tandem slit. The distance from the slit to the transmitting antenna was selected such that the transmitting antenna produces almost uniform field on the surface of the slit. This distance was selected to be $15\lambda_o$, where the ratio of the incident field at the edge of the slit to the field at the slit center was measured to be 0.9. Absorbers were placed around the transmitting and receiving antennas to avoid reflections. First, a solid sheet of FR4 (no slit) was placed between the antennas, and the transmission coefficient (S_{12}) is measured over an angle range of -50° to 50° relative to the axis of the transmit antenna, yielding received signals in the noise floor of the measurement system. Then, the solid sheet was replaced with the FR4 sheet with a $2\lambda_o$ slit, and the measurements were repeated.

Additional validation of the Wiener-Hopf solution was provided using *FastFDTD* to provide numerical simulations of several loaded tandem slit geometries. Each 2D FDTD model consists of a tandem slit on dielectric layer of finite width ($20\lambda_o$). The following three loaded tandem slit geometries were simulated (loaded with $\varepsilon_r = 4.2$, loss tangent = 0.012 in each case): (i) l = 60mm, $2d$ = 1.3 mm (ii) l = 90mm, $2d$ = 1.3 mm and (iii) l = 90mm, $2d$ = 5 mm. The structure was excited with a normally incident plane wave and the near fields on the loaded tandem slit were obtained. The radiated far field was obtained from the total near fields via the transformation defined in [15].

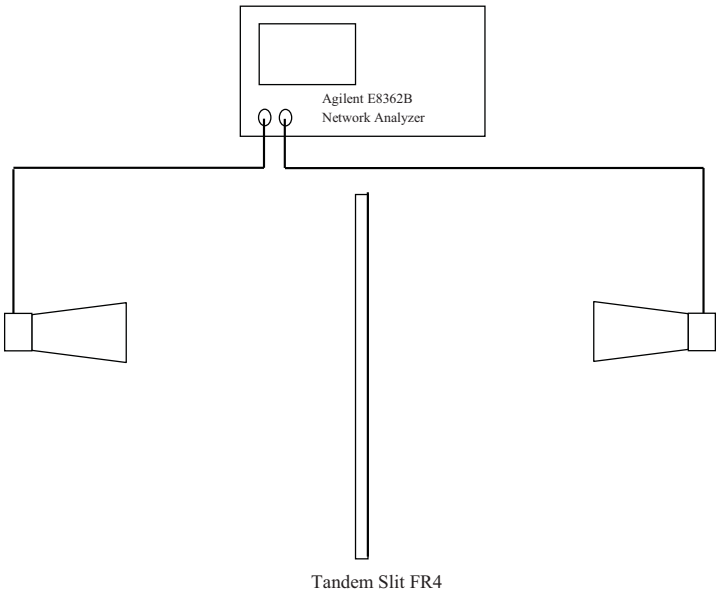

Figure 2.4. System used for loaded tandem slit measurements.

A comparison of the Wiener-Hopf solution, 2D FDTD simulation, and experimental measurements is shown in Figure 2.5 for the loaded tandem slit with l = 60mm and $2d$ = 1.3 mm. The three curves in Figure 2.5 are normalized to the respective

peak values in order to compare the Wiener-Hopf and FDTD solutions with the measured results. The Wiener-Hopf solution is also compared to FDTD simulations for normal incidence on loaded tandem slits with l = 90mm and $2d$ = 1.3 mm in Figure 2.6 and l = 90mm and $2d$ = 5 mm in Figure 2.7. The diffracted fields in Figure 2.6 and Figure 2.7 are determined at a radial distance of 20 λ_o from the tandem slit. Excellent agreement among the numerical, experimental, and theoretical solutions is shown in Figure 2.5, Figure 2.6 and Figure 2.7. The loaded tandem slit solution is also verified against the transmission cross section and normalized far-field pattern for an unloaded tandem slit obtained by Kashyap [2]. In Figure 2.8(a), Kashyap's single slit solution (along with exact solution [2]) is compared to the tandem slit solution with very closely spaced conducting plates (ε_r = 1, d = 1 μm), while Figure 2.8(b) gives the same comparison for an unloaded tandem slit (ε_r = 1, $2k_od$ = 0.984). Figure 2.9 shows a comparison of the normalized far-field pattern for an unloaded tandem slit (l=80mm, d=1μm, frequency =10GHz) obtained by Kashyap with that using the current technique. Again, good agreement is found. In order to quantify the power coupled through the tandem slit, we define

$$\text{Normalized Coupled Power} = \frac{\int_0^{\pi} \frac{|u_3(r,\phi)|^2}{\eta} r d\phi}{l/\eta} = \frac{\int_0^{\pi} |u_3(r,\phi)|^2 r d\phi}{l} \tag{22}$$

where 'r' is taken in the far field and 'l/η' is the incident power falling on the aperture. The field pattern in region 3 of the tandem slit geometry can give rise to multiple lobes, especially in the vicinity of the resonant frequencies. The 6-dB beamwidth is defined here as the angular interval over which the electric field is greater than half the maximum value, irrespective of multiple lobes with minima that may dip below this level. For an

example tandem slit (l = 30mm, $2d$ = 5mm) at 10 GHz, Figure 2.10 shows how the loading material permittivity affects the beamwidth and normalized coupled power. Note that a significant decrease in beamwidth and increase in coupled power occurs for ε_r = 3.5. The effect of the loading material thickness on the beamwidth and normalized coupled power for the corresponding loaded tandem slit (l = 30mm, ε_r = 3.5) is shown in Figure 2.11. Again, it is observed that loading thicknesses of approximately 5mm and 15mm exhibit reduced beamwidth and increased coupled power. As discussed previously in the introduction, microwave filters with material loaded tandem bifurcation designed at these parameter values (l = 30mm, ε_r = 3.5 and $2d$ = 5mm) can be used to increase the filter transmission coefficient. The variation of beamwidth and coupled power as the loaded tandem slit width is varied is shown in Figure 2.13 for ε_r = 3.5 and $2d$ = 5mm. The beamwidth decreases in a step-like pattern with sharp local minima and maxima at the structure resonances, while the coupled power per unit width increases in a nearly linear fashion between resonant peaks. The step changes in the beamwidth are more significant for lower slit widths. Note that the results of Figure 2.10, Figure 2.11, and Figure 2.12 show a decrease in beamwidth for the loaded tandem slit which is generally associated with an increase in coupled power, except for the first resonance in Figure 2.12 where the reduction in beamwidth is not prominent. The parameter 'l' should be varied judiciously since a large value would make the transmission coefficient better, but would also deteriorate the reflection coefficient in the stop band and is also limited by physical constraints like waveguide dimensions.

The time required for the loaded tandem slit Wiener-Hopf solution is compared to that of the *FastFDTD* solution in Table 2.1 for the examples shown in Figure 2.5, Figure

2.6, and Figure 2.7. *FastFDTD* is an accelerated FDTD solver that utilizes the processing capabilities of modern graphics cards to obtain 30 to 50 times faster solutions than standard processors. All computations were performed on a 3.4 GHz machine with 3.5GB of RAM. The *FastFDTD* simulations were implemented on a grid of 2 Mcells over 10 cycles (10^4 timesteps). The computation times for the FDTD simulations in Table 2.1 do not include the post-processing time required to generate the far-field pattern from the aperture fields. No post-processing is required for the Wiener-Hopf solutions. The largest portion of the computation time in the Wiener-Hopf procedure is devoted to the evaluation of the L(α) and M(α) factors. The factorization calculations are faster for thicker tandem slit configurations than for thinner ones due to the faster convergence of integrals which can also be seen in Table 2.1. The Wiener-Hopf solution is roughly four times faster than the corresponding *FastFDTD* solution for the loaded tandem slit geometries considered here. Finally, to obtain the validity limit of the approximate Wiener-Hopf solution, the normalized power coupled obtained from Wiener-hopf procedure is compare to that obtained from *FastFDTD* for slit widths from $0.1\lambda_o$ to $3\lambda_o$. The comparison is shown in Figure 2.13(a) and (b). A very close agreement between these is found confirming the validity of the Wiener-Hopf procedure for '*l*' greater than and equal to $0.1\lambda_o$.

Table 2.1. Computation times using Wiener-Hopf and *FastFDTD*

Figure	Time (seconds) Wiener-Hopf	Time (seconds) 2D FastFDTD
5	63	247
6	63	246
7	58	276

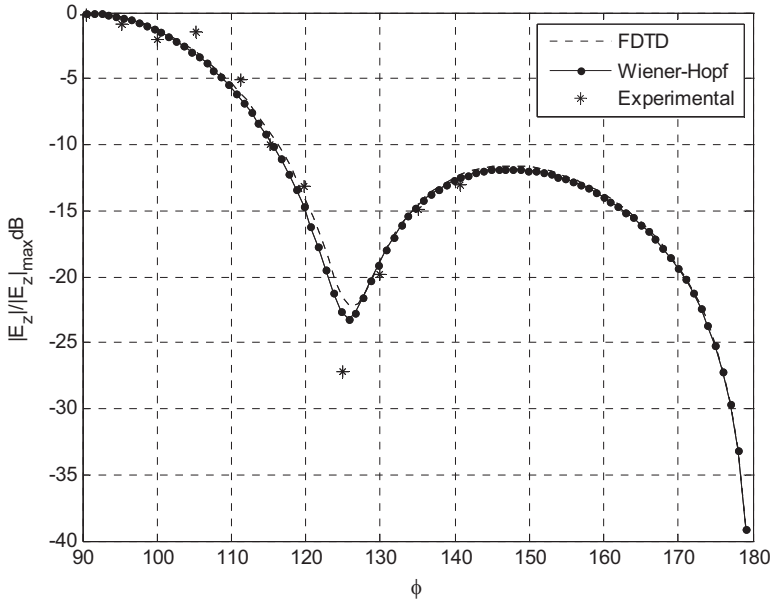

Figure 2.5. Comparison of the normalized diffracted field for a loaded tandem slit (l = 60 mm, $\varepsilon_r = 4.2$, loss tangent = 0.012, $2d$ = 1.3 mm, frequency = 10 GHz)

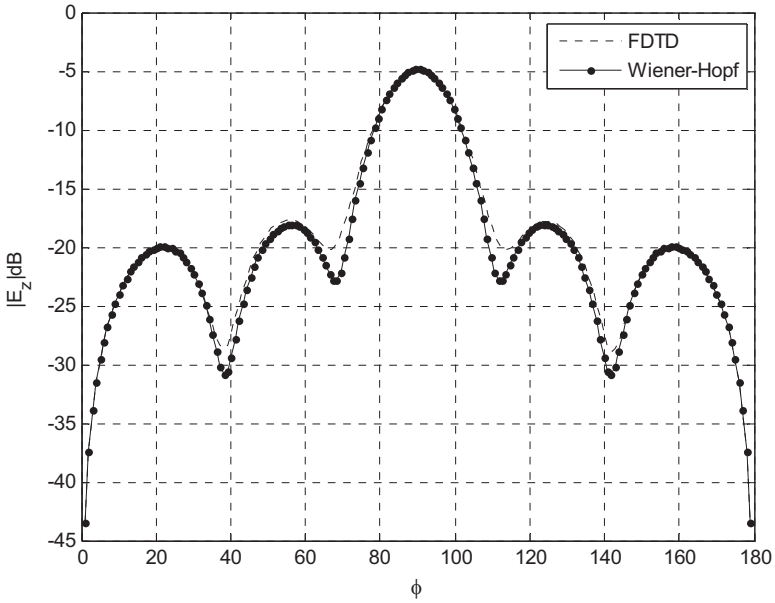

Figure 2.6. Loaded tandem slit diffracted field at $20\lambda_o$ (l = 90 mm, $\varepsilon_r = 4.2$, loss tangent = 0.012, $2d$ = 1.3 mm, frequency = 10 GHz)

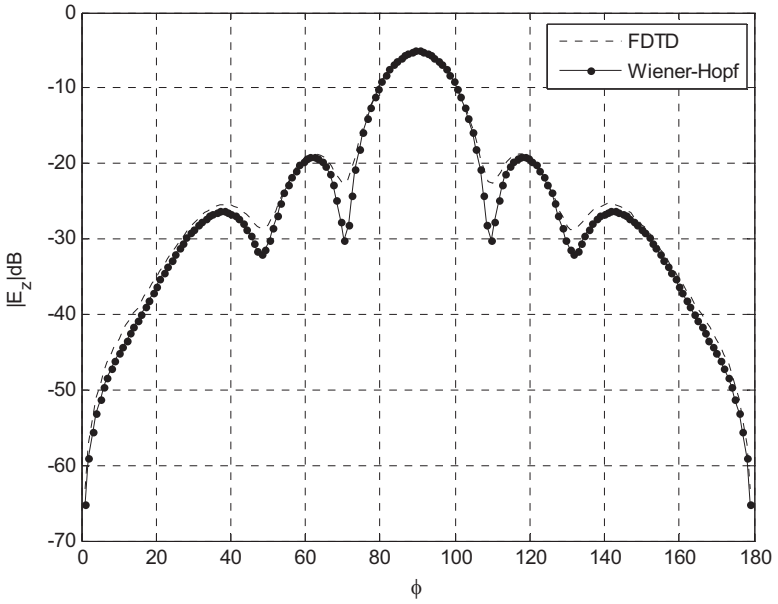

Figure 2.7. Loaded tandem slit diffracted field at $20\lambda_o$ (l = 90 mm, ε_r = 4.2, loss tangent = 0.012, $2d$ = 5 mm, frequency=10 GHz)

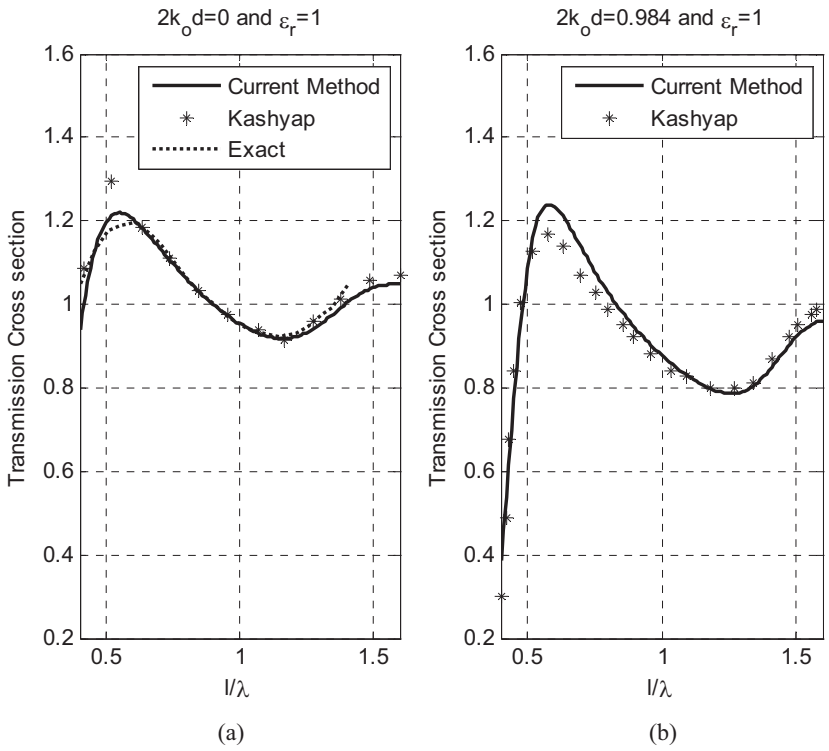

Figure 2.8. Transmission Coefficient verses l/λ for (a) a single slit and (b) an unloaded tandem slit.

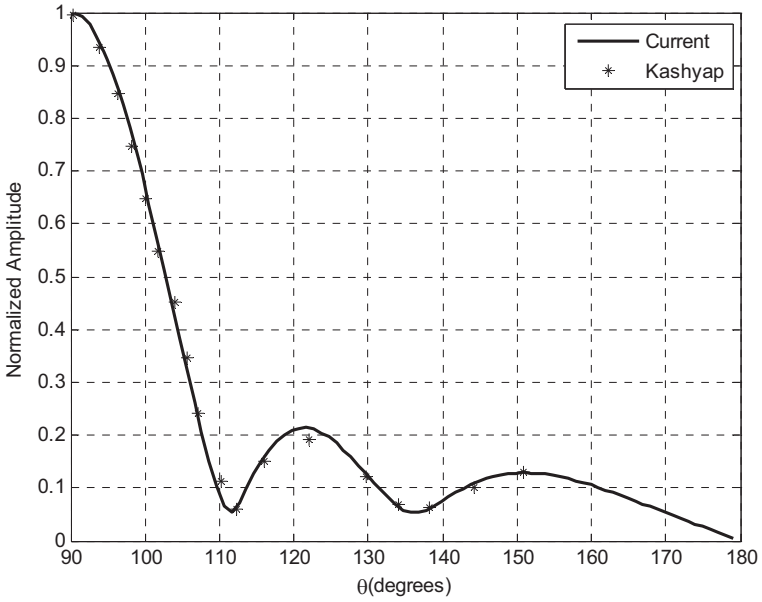

Figure 2.9. Normalized diffracted field for a tandem slit (l = 80mm, ε_r = 1, d = 1 μm, frequency = 10 GHz)

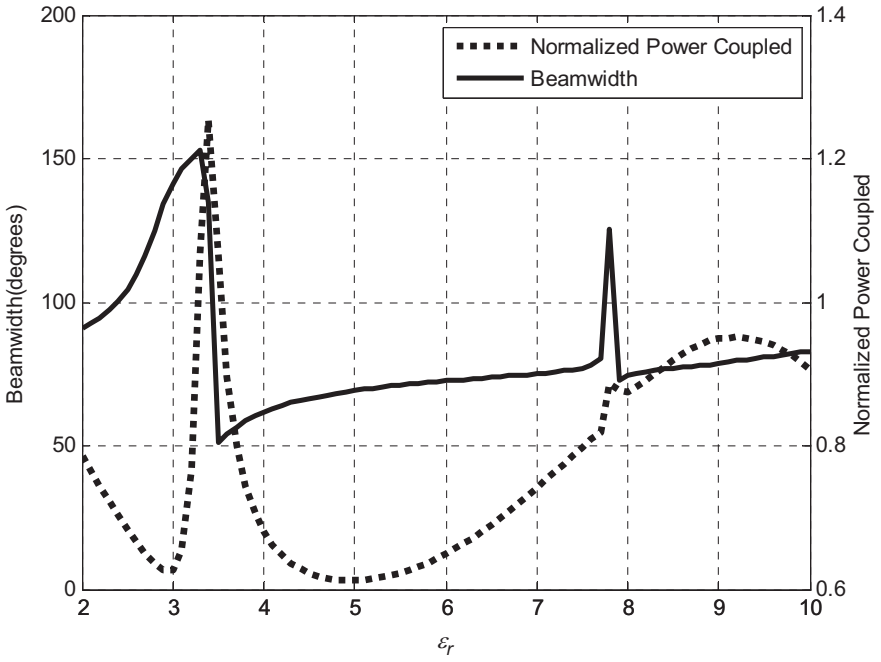

Figure 2.10. Beamwidth (degrees) and normalized power coupled from a loaded tandem slit for different dielectric materials (l = 30 mm, 2d = 5 mm, frequency = 10 GHz)

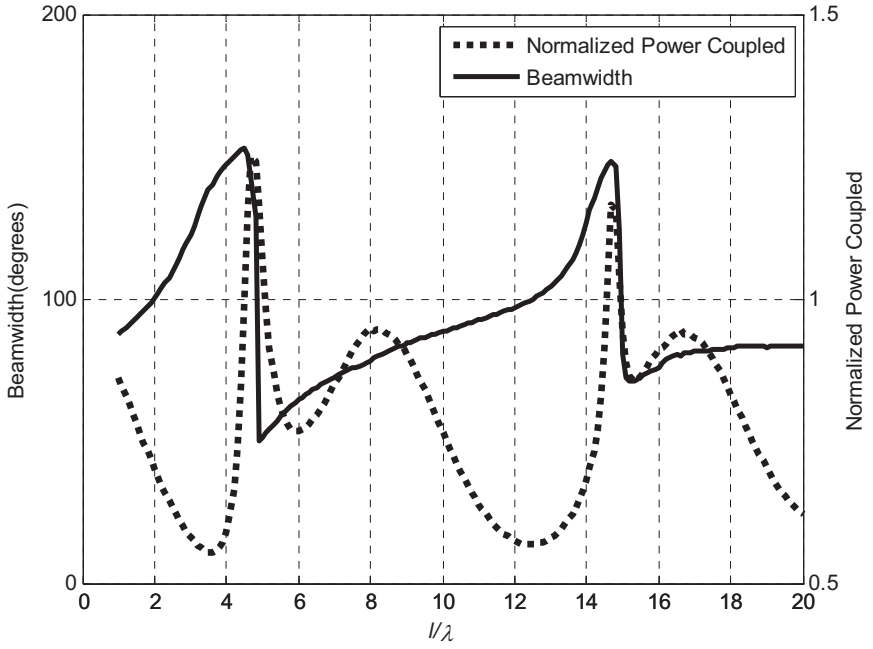

Figure 2.11. Beamwidth (degrees) and normalized power coupled from a loaded tandem slit for different slit thicknesses (l = 30 mm, ε_r = 3.5, frequency = 10 GHz)

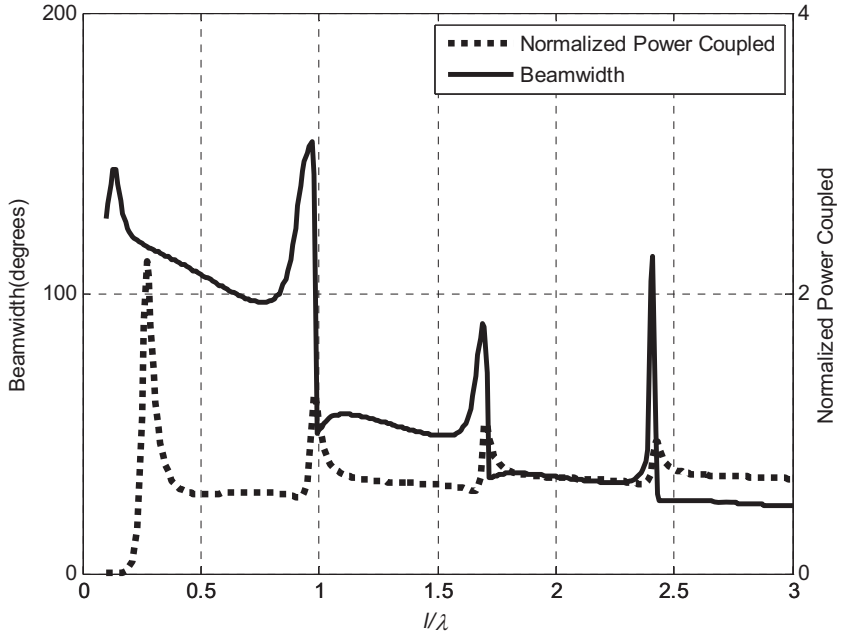

Figure 2.12. Beamwidth (degrees) and normalized power coupled from a loaded tandem slit for different slit widths (2*d* = 5 mm, ε_r = 3.5, frequency = 10 GHz)

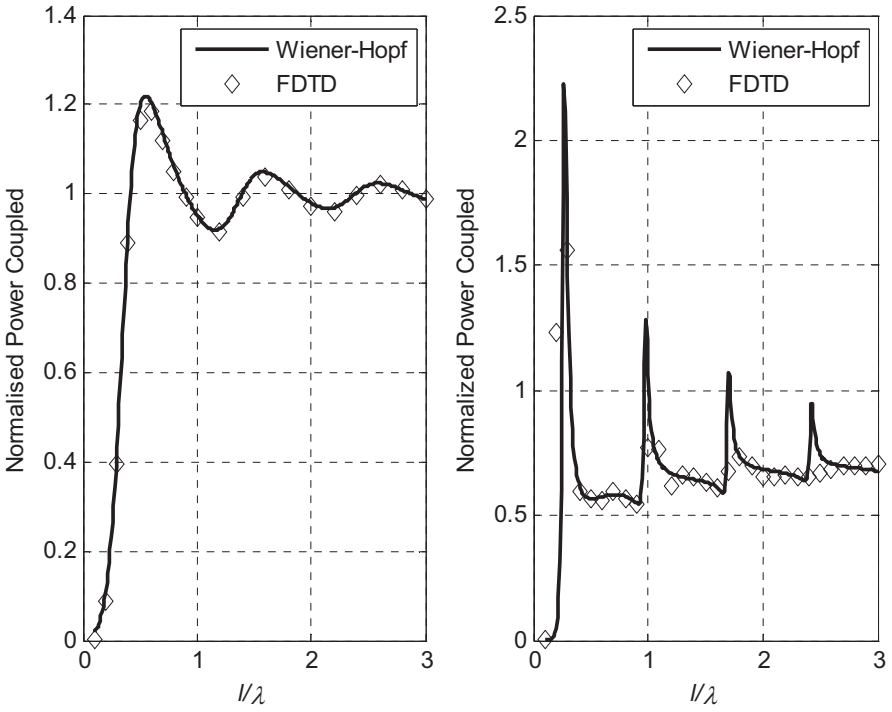

Figure 2.13. Normalized power coupled from a (a) single slit (b) loaded tandem slit ($2d$ = 5mm, $\varepsilon_r = 3.5$).

CHAPTER III

SCATTERING BY A ECCENTRICALLY LOADED CYLINDRICAL CAVITY WITH MULTIPLE SLITS

3.1 Introduction

In this chapter, we consider scattering by a loaded cylindrical cavity with multiple longitudinal slits in the outer conductor and an eccentrically located inner conductor. The details of the scatterer geometry are defined in Section 3.2. The motivation behind the analysis is to characterize the backscattered radar cross section (RCS) relative to the number and position of the slits in the outer conductor and the position of the inner conductor. The first formulation considered is the solution of the integral equation using the combined boundary condition (CBC), which was introduced by Montiel and Neviere in [29]. This formulation is designated as the IE/CBC solution and appears in Section 3.3. Based on slow convergence results for the IE/CBC approach, an integral equation solution utilizing a Neumann series current expansion (IE/NS) is formulated in Section 3.4. TE and TM excitations are considered for both formulations. The backscattered RCS of several geometries are presented in Section 3.5 giving a comparison of the solution approaches.

3.2 Geometry of the problem

The geometry of the eccentrically loaded cylindrical cavity with multiple slits illuminated by a plane wave is shown in Figure 3.1. The radii of the inner and outer perfectly conducting cylinders are defined by a and b, respectively. The outer cylinder, with multiple slits, is assumed to be infinitesimally thin, with its axis lying along the z axis of the cylindrical coordinate system (r, ϕ, z). The exterior and interior regions(w.r.t outer cylinder) are assumed to be ideal dielectrics of permittivities ε_1 and ε_2, respectively. The axis of the inner conductor is located at (r_o, ϕ_o). A shifted cylindrical coordinate system (r', ϕ', z') is used to define the fields internal to the outer cylinder where the axis of the inner conductor lies along the z' axis of the shifted coordinate system. The structure is illuminated by a TM to z (electric field parallel to z-axis) or TE to z (magnetic field parallel to z-axis) plane wave incident at an angle of ϕ_i. The time dependence assumed here is $\exp(-j\omega t)$. The union of all cylindrical coordinate angles ϕ swept over the range of $[0,2\pi]$ by the metal portions of the outer cylinder is defined by Ω_1 while Ω_2 denotes the complement of Ω_1. The wavenumber of the external region is denoted by k and the wavenumber of the internal region is denoted by k_1.

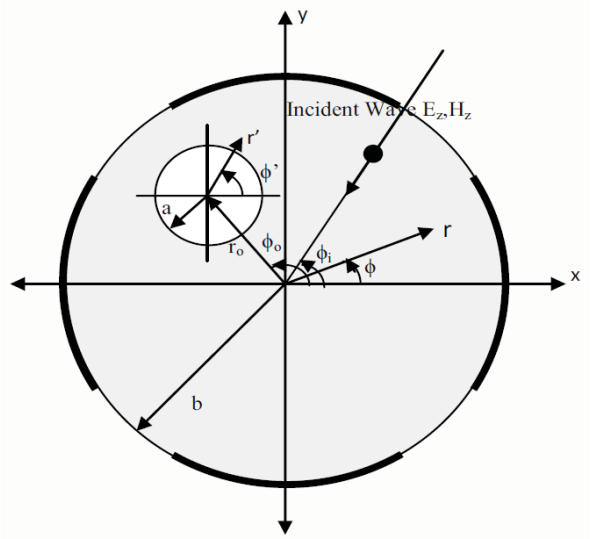

Figure 3.1. TE/TM plane wave incident on an eccentrically loaded cylindrical cavity with multiple slits.

3.3 Integral Equation/Combined Boundary Condition Formulation

The problem is formulated using an integral equation solution for the unknown current density [32] on the eccentrically loaded cylinder with multiple slits. The segmented contour of the outer cylindrical shell with slits is denoted by L_1 and the continuous contour on the surface of the solid inner cylinder is denoted by L_2. We assume that the internal and external media are identical ($k_1 = k$), in order to simplify the expressions. An extension of the formulation to the case of $k_1 \neq k$ can be obtained by replacing the free space Green's function with the dielectric cylinder Green's function. The tangential components of the total electric field (incident plus scattered fields) must be zero on the perfectly conducting surfaces, so that the scattered fields on these surfaces must equal the negative of the incident fields. The integral equations for the resulting currents under TE or TM illumination are formulated by applying Green's theorem to the respective scattered fields.

3.3.1 *Integral Equation - TM case*

The integral equation for the z-directed surface current density J_z^{surf} on the eccentrically loaded cylinder with multiple slits under TM illumination can be written as

$$\sum_{j=1}^{2} \int_{L_j} J_z^{surf}(r_j) H_o^1(k|r_i - r_j|)\, dl_j = -E_z^{inc}(r_i) \tag{3.1}$$

where $i = 1, 2$ and (r_i, r_j) are the radial distances in cylindrical coordinates locating points on the field conductor (conductor i) where the boundary condition is enforced and points on the source conductor (conductor j) where the current is located. Thus, r_1 and r_2 locate points on the contours L_1 and L_2. Expanding the current densities and the incident electric field in terms of Fourier series and utilizing the addition theorem for Hankel functions in (3.1) gives

$$\begin{aligned} &\sum_{m=-\infty}^{\infty} H_m^1(kb) \sum_{n=-\infty}^{\infty} \frac{A'_{n2}\, J_{m-n}(kr_o) e^{-j(m-n)\phi_o}}{H_n^1(ka)} e^{jm\phi} \\ &+ \sum_{m=-\infty}^{\infty} A'_{m1}\, e^{jm\phi} = -\sum_{m=-\infty}^{\infty} a_m J_m(kb) e^{jm\phi}, \phi \in \Omega_2 \end{aligned} \tag{3.2}$$

$$\sum_{m=-\infty}^{\infty} \frac{A'_{m1}}{2\pi b J_m(kb) H_m^1(kb)} e^{jm\phi} = 0, \phi \in \Omega_1 \tag{3.3}$$

$$\begin{aligned} &J_m(ka) \sum_{n=-\infty}^{\infty} \frac{A'_{n1} J_{m-n}(kr_o) e^{-j(m-n)(\phi_o+\pi)}}{J_n(kb)} + A'_{m2} = \\ &-\sum_{n=-\infty}^{\infty} a_n J_{m-n}(kr_o) e^{-j(m-n)(\phi_o+\pi)} J_m(ka) \end{aligned} \tag{3.4}$$

where

$$A'_{m1} = 2\pi b J_m(kb) H_m^1(kb) A_{m1} \tag{3.5}$$

$$A'_{m2} = 2\pi a J_m(ka) H_m^1(ka) A_{m2} \tag{3.6}$$

A_{m1} and A_{m2} are Fourier coefficients of the current density on the surface L_1 and L_2 respectively and a_n defines the amplitude of the incident plane wave. For simplicity, (3.2) and (3.3) can be written as

$$f(x) = 0 \qquad \phi \in \Omega_2 \tag{3.7}$$

$$g(x) = 0 \qquad \phi \in \Omega_1 \tag{3.8}$$

Following the technique used by Guizal [30], (3.7) and (3.8) can be combined into a single equation that holds for all ϕ in [0,2π] such that

$$g\chi(\phi)\, f(x) + [1 - \chi(\phi)]\, g(x) = 0 \tag{3.9}$$

where $\chi(\phi)$ is the characteristic function of the set Ω_2, defined by

$$\chi(\phi) = \begin{cases} 1 & \phi \in \Omega_2 \\ 0 & elsewhere \end{cases} \tag{3.10}$$

and g is a parameter introduced for numerical purposes. The function $\chi(\phi)$ is periodic with respect to ϕ and can be expanded in terms of a Fourier series as

$$\chi(\phi) = \sum_{p=-\infty}^{\infty} \chi_p \exp(jp\phi) \tag{3.11}$$

By substituting (3.4) and (3.2) and applying the combined boundary condition along with orthogonality of the Fourier coefficients yields

$$
\begin{aligned}
&A'_{m1} - \sum_{k=-\infty}^{\infty} A'_{k1}\Big[f_{1mk} + \chi_{m-k} \\
&- \sum_{p=-\infty}^{\infty} \chi_{m-p} f_{1pk} - \frac{g\,\chi_{m-k}}{2\pi\, bJ_k(kb)H_k^1(kb)}\Big] \\
&= -a_m J_m(kb) + \sum_{k=-\infty}^{\infty} a_k f_{2mk} + \sum_{p=-\infty}^{\infty} \chi_{m-p} a_p J_p(kb) \\
&- \sum_{p=-\infty}^{\infty} \chi_{m-p} \sum_{k=-\infty}^{\infty} a_k f_{2pk}
\end{aligned}
\tag{3.12}
$$

where

$$
\begin{aligned}
&f_{1mk} = H_m^1(kb) \times \\
&\sum_{n=-\infty}^{\infty} \frac{J_n(ka)J_{m-n}(kr_o)J_{k-n}(kr_o)e^{-j(2n-k-m)\phi_o}}{H_n^1(ka)J_k(ka)}
\end{aligned}
\tag{3.13}
$$

$$
\begin{aligned}
&f_{2mk} = H_m^1(kb) \times \\
&\sum_{n=-\infty}^{\infty} \frac{J_n(ka)J_{m-n}(kr_o)J_{k-n}(kr_o)e^{-j(2n-k-m)\phi_o}}{H_n^1(ka)}
\end{aligned}
\tag{3.14}
$$

The solution of the linear system of equations in (3.12) gives the A'_{m1} coefficients. The A'_{m2} coefficients can then be determined using (3.4), yielding the overall field. The normalized RCS for the TM case can be calculated as

$$
\begin{aligned}
\frac{\sigma}{\pi b} = \frac{16\pi b}{k} \Bigg| &\sum_{n=-\infty}^{\infty} A_{m1} J_n(kb) e^{j\left[n\phi - (2n+1)\frac{\pi}{4}\right]} \\
+ \frac{a}{b} &\sum_{m=-\infty}^{\infty} e^{j\left[m\phi - (2m+1)\frac{\pi}{4}\right]} \\
&\sum_{n=-\infty}^{\infty} A_{n2} J_n(ka) J_{n-m}(kr_o) e^{j(n-m)\phi_o} \Bigg|^2
\end{aligned}
\tag{3.15}
$$

3.3.2 *Integral Equation - TE case*

The integral for the surface current density on the eccentrically loaded cylinder with multiple slits under TE illumination is given by

$$\begin{aligned}&\frac{\partial}{\partial n_i}\sum_{j=1}^{2}\int_{L_j} J_{\phi}^{surf}(r_j)\frac{\partial}{\partial n_j}H_o^1(k|r_i-r_j|)dl_j\\&=-\frac{\partial H_o^1(r_i)}{\partial n_i}\end{aligned} \tag{3.16}$$

where n_i defines the normal to the curve L_i. Following the same procedure defined for the TM case, we find

$$\begin{aligned}&A'_{m1}-\sum_{k=-\infty}^{\infty}A'_{k1}\Big[f_{1mk}+\chi_{m-k}\\&-\sum_{p=-\infty}^{\infty}\chi_{m-p}f_{1pk}-\frac{g\chi_{m-k}}{2\pi bk^2J_k'(kb)H_k^{1\prime}(kb)}\Big]\\&=-ka_mJ_m'(kb)+k\sum_{k=-\infty}^{\infty}a_kf_{2mk}\\&+\sum_{p=-\infty}^{\infty}k\chi_{m-p}a_pJ_p(kb)-k\sum_{p=-\infty}^{\infty}\chi_{m-p}\sum_{k=-\infty}^{\infty}a_kf_{2pk}\end{aligned} \tag{3.17}$$

where

$$\begin{aligned}&f_{1mk}=H_m^{1\prime}(kb)\times\\&\sum_{n=-\infty}^{\infty}\frac{J_n'(ka)J_{m-n}(kr_o)J_{k-n}(kr_o)e^{-j(2n-k-m)\phi_o}}{H_n^{1\prime}(ka)J_k'(ka)}\end{aligned} \tag{3.18}$$

$$\begin{aligned}&f_{2mk}=H_m^{1\prime}(kb)\times\\&\sum_{n=-\infty}^{\infty}\frac{J_n'(ka)J_{m-n}(kr_o)J_{k-n}(kr_o)e^{-j(2n-k-m)\phi_o}}{H_n^{1\prime}(ka)}\end{aligned} \tag{3.19}$$

$$A'_{m1}=2\pi k^2bJ_m'(kb)H_m^{1\prime}(kb)A_{m1} \tag{3.20}$$

$$A'_{m2} = 2\pi k^2 a J_m'(ka) H_m^1'(ka) A_{m2} \tag{3.21}$$

The solution throughout the internal and external regions is obtained by solving the linear system in (3.17). The resulting normalized RCS for the TE case is

$$\frac{\sigma}{\pi b} = 16\pi bk \left| \sum_{n=-\infty}^{\infty} A_{m1} J_n'(kb) e^{j\left[n\phi - (2n+1)\frac{\pi}{4}\right]} + \frac{a}{b} \sum_{m=-\infty}^{\infty} e^{j\left[m\phi - (2m+1)\frac{\pi}{4}\right]} \times \sum_{n=-\infty}^{\infty} A_{n2} J_n'(ka) J_{n-m}(kr_o) e^{j(n-m)\phi_o} \right|^2 \tag{3.22}$$

3.4 Integral Equation/Neumann Series Formulation

The efficiency of the integral equation solution can be enhanced significantly by utilizing a Neumann series expansion for the current on each of the individual conductors that make up the cylinder with multiple slits (cylinder segments). The basic functions of the Neumann series can be defined so that the proper edge behavior for the currents on the cylinder segments is exhibited for either the TE or TM case. A general function of ϕ defined on the unit circle can be expressed in terms of a Fourier series as

$$f(\phi) = \sum_{n=-\infty}^{\infty} D_n e^{jn\phi} \tag{3.23}$$

where D_n are the Fourier coefficients. Consider first a cylinder with a single slit, where the angle range of the conductor is $\phi \in [-\phi_w, \phi_w]$. As shown in [35], each Fourier coefficient of the expansion in (3.23) can be expressed in terms of the following Neumann series expansion:

$$D_n = \sum_{p=0}^{\infty} \chi_p \frac{J_{v+p}(n\phi_w)}{(n\phi_w)^v} \tag{3.24}$$

where v is a parameter chosen based on the required edge behavior, and the inverse Fourier transform for each term in (3.24) [36] is given by

$$\begin{aligned} &\sum_{n=-\infty}^{\infty} \frac{J_{v+p}(n\phi_w)}{(n\phi_w)^v} e^{jn\phi} \\ &= \begin{cases} G(p,v)[1-(\phi/\phi_w)^2]^{v-1/2} C_p^v(\phi/\phi_w) & \phi \in [-\phi_w, \phi_w] \\ 0 & otherwise \end{cases} \end{aligned} \tag{3.25}$$

where $G(p,v)$ is function of p and v only, and $C_p^v(\phi/\phi_w)$ is the Gegenbauer polynomial. The proper behavior of the field at the edges of the cylinder is given by $v = 0$ for the TM case and $v = 1$ for the TE case. For the eccentrically loaded cylinder with N_s multiple slits, we assume that the center of s^{th} cylinder segment is located by the angle ϕ_{so} and spans a total angle range of $2\phi_{sw}$. Expressing the Fourier coefficient A_{m1} of the original integral equation formulation in terms of the Neumann series yields

$$A_{m1} = \sum_{s=1}^{N_s} \sum_{p=0}^{\infty} \chi_{sp} J_p(m\phi_{sw}) e^{-jm\phi_{so}} \tag{3.26}$$

The current density for the TM case becomes

$$\begin{aligned} J_z^{surf}(\phi) &= \sum_{s=1}^{N_s} \sum_{m=-\infty}^{\infty} \sum_{p=0}^{\infty} \chi_{sp} J_p(m\phi_{sw}) e^{jm(\phi-\phi_{so})} \\ &= \begin{cases} \sum_{s=1}^{N_s} \sum_{p=0}^{\infty} \dfrac{\chi_{sp}}{\sqrt{1-\left(\dfrac{\phi-\phi_{so}}{\phi_{sw}}\right)^2}} C_p^0\left(\dfrac{\phi-\phi_{so}}{\phi_{sw}}\right) & |\phi-\phi_{so}| \le \phi_{sw} \\ 0 & otherwise \end{cases} \end{aligned} \tag{3.27}$$

Substituting (3.26) into (3.2) and (3.4), combining the results, and testing with

$$C_m^0\left(\frac{\phi-\phi_{ko}}{\phi_{kw}}\right)\left[1-\left(\frac{\phi-\phi_{ko}}{\phi_{kw}}\right)^2\right]^{-1/2}$$

yields the required TM linear system.

$$\begin{aligned}
&2\pi b\sum_{s=1}^{N_s}\sum_{p=0}^{\infty}\chi_{sp}\sum_{n=-\infty}^{\infty}J_n(kb)H_n^1(kb)J_p(n\phi_{sw})J_m(n\phi_{sw})e^{jn(\phi_{ko}-\phi_{so})}\\
&-2\pi b\sum_{s=1}^{N_s}\sum_{p=0}^{\infty}\chi_{sp}\sum_{g=-\infty}^{\infty}H_g^1(kb)J_p(g\phi_{sw})\\
&\qquad\times e^{-jg\phi_{so}}\sum_{m=-\infty}^{\infty}\frac{J_m^1(ka)}{H_m^1(ka)}J_{m-g}(kr_o)e^{-j(m-g)(\pi+\phi_{so})}\\
&*\sum_{n=-\infty}^{\infty}J_{n-m}(kr_o)e^{-j(n-m)\phi_{so}}H_n^1(kb)J_m(n\phi_{sw})e^{jn\phi_{ko}}\\
&-\sum_{m=-\infty}^{\infty}\frac{J_m(ka)}{H_m^1(ka)}\sum_{g=-\infty}^{\infty}a_gJ_{m-g}(kr_o)e^{-j(m-g)(\phi_{so}+\pi)}\\
&*\sum_{n=-\infty}^{\infty}J_{n-m}(kr_o)e^{-j(n-m)\phi_{so}}H_n^1(kb)J_m(n\phi_{sw})e^{jn\phi_{ko}}\\
&=-\sum_{n=-\infty}^{\infty}a_nJ_n(kb)J_m(n\phi_{sw})e^{jn\phi_{ko}}
\end{aligned}\tag{3.28}$$

Similarly, expanding the Fourier coefficients of the TE case as

$$A_{m1}=\sum_{s=1}^{N_s}\sum_{p=0}^{\infty}\chi_{sp}\frac{J_{p+1}(m\phi_{sw})}{m\phi_{sw}}e^{-jm\phi_{so}}\tag{3.29}$$

and following the same procedure as outlined for the TM case yields the required TE linear system.

$$
\begin{aligned}
&2\pi b\sum_{s=1}^{N_s}\sum_{p=0}^{\infty}\chi_{sp}\sum_{n=-\infty}^{\infty}k^2 J_n'(kb)H_n^{1\,\prime}(kb)\frac{J_{p+1}(n\phi_{sw})J_{m+1}(n\phi_{sw})}{(n\phi_{sw})^2}e^{jn(\phi_{ko}-\phi_{so})}\\
&-2\pi b\sum_{s=1}^{N_s}\sum_{p=0}^{\infty}\chi_{sp}\sum_{g=-\infty}^{\infty}kH_g^{1\,\prime}(kb)\\
&\times\frac{J_{p+1}(g\phi_{sw})}{g\phi_{sw}}e^{-jg\phi_{so}}\sum_{m=-\infty}^{\infty}\frac{J_m'(ka)}{H_m^{1\,\prime}(ka)}J_{m-g}(kr_o)e^{-j(m-g)(\pi+\phi_{so})}\\
&*\sum_{n=-\infty}^{\infty}J_{n-m}(kr_o)e^{-j(n-m)\phi_{so}}kH_n^{1\,\prime}(kb)\\
&\times\frac{J_{m+1}(n\phi_{sw})}{n\phi_{sw}}e^{jn\phi_{ko}}-\sum_{m=-\infty}^{\infty}\frac{J_m'(ka)}{H_m^{1\,\prime}(ka)}\sum_{g=-\infty}^{\infty}a_g J_{m-g}(kr_o)e^{-j(m-g)(\phi_{so}+\pi)}\\
&\quad\times\sum_{n=-\infty}^{\infty}J_{n-m}(kr_o)e^{-j(n-m)\phi_{so}}H_n^{1\,\prime}(kb)\frac{J_{m+1}(n\phi_{sw})}{n\phi_{sw}}e^{jn\phi_{ko}}\\
&=-\sum_{n=-\infty}^{\infty}a_n kJ_n'(kb)\frac{J_{m+1}(n\phi_{sw})}{n\phi_{sw}}e^{jn\phi_{ko}}
\end{aligned}
\tag{3.30}
$$

The TM linear system in (3.28) and the TE linear system in (3.30) are solved to obtain the respective solutions.

3.5 Numerical Procedure and Results

Determination of the scattered fields for the eccentrically loaded cylinder with multiple slits requires a linear system solution of the following form when using a CBC-based formulation:

$$[\beta][b_n]+g[\beta_g][b_n]=[\alpha][a_n] \tag{3.31}$$

where $[a_n]$ and $[b_n]$ are vectors containing the coefficients defined in (3.12) for TM case and (3.17) for TE case, g is a constant that provides a relative weighting of boundary conditions, and $[\beta\,]$, $[\beta_g]$ and $[\alpha]$ are coefficient matrices. In previous solutions employing the CBC, such as [34], a typical choice for the parameter g is -0.001.

However, as the slit width grows smaller, the magnitudes of the $[\beta_g]$ elements grow smaller relative to those of $[\beta]$, resulting in inaccuracies for the fields within the slit. Thus, in order to assign comparable weights to the boundary conditions and allow for any slit size, the parameter g is defined according to

$$g = \frac{\| diag(\beta) \|}{\| diag(\beta_g) \|} \tag{3.32}$$

where each term in (3.32) is the Euclidean norm of the diagonal elements of each matrix. A detailed analysis regarding the selection of the CBC parameter g is the subject of a future research.

In order to determine the number of terms N required to obtain an accurate solution for the backscattered RCS (σ_{bs}) of the eccentrically loaded cylinder with slits using the two integral equation formulations considered here, we define the truncation error as

$$\text{Truncation error} = \left| \frac{\sigma_{\text{bs}}(N) - \sigma_{\text{bs}}(N+1)}{\sigma_{\text{bs}}(N)} \right| \tag{3.33}$$

where the IE/CBC coefficients are truncated from $-N$ to N while the IE/NS coefficients are truncated from 0 to N. A comparison of the solution convergence for the IE/CBC and IE/NS formulations is shown in Figure 3.2 for a coaxial cylinder (a = 0.8m, b = 1m) with a 10° slit located at $\Omega_2 \in$ (-5°,5°) and ϕ_{inc} = 90°. The results in Figure 3.2 show that the IE/NS method requires significantly fewer terms than the IE/CBC method to achieve a given solution accuracy.

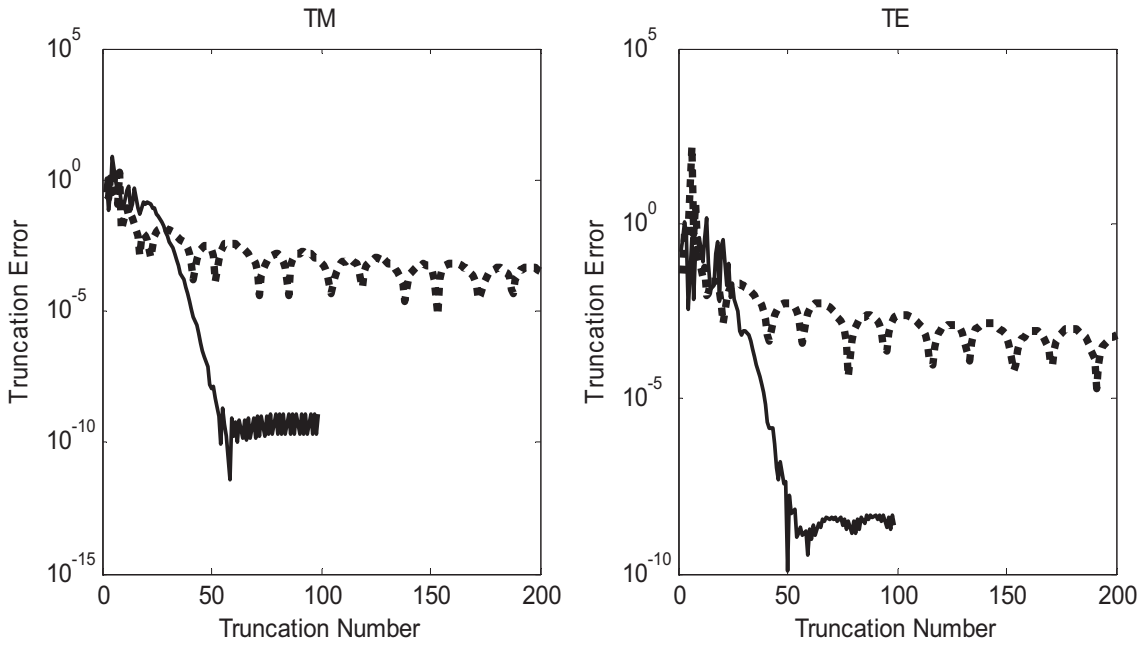

Figure 3.2. Truncation error vs. truncation number N [a = 0.8m, b = 1m, r_o= 0, ϕ_o = 0°, ϕ_{inc} = 90°, $\Omega_2 \in$ (-5°,5°)].

The computational burden associated with the evaluation of the Fourier-Neumann coefficients in the IE/NS formulation depends on a truncated series of the general form seen in the first terms in (3.28) and (3.30)

$$\sum_{n=-\infty}^{\infty} b_n \frac{J_{p+v}(n\phi_{sw})J_{m+v}(n\phi_{sw})}{(n\phi_{sw})^{2v}} e^{jn(\phi_{ko}-\phi_{so})} \tag{3.34}$$

where $v = 0$ for the TM case and $v = 1$ for the TE case, and

$$b_n = \begin{cases} J_n(kb)H_n^1(kb) \approx -j\dfrac{1}{\pi n} \quad as\ n \to \infty \quad (TM) \\ k^2 J_n{}'(kb)H_n^{1\,\prime}(kb) \approx j\dfrac{2n}{\pi b^2}\ as\ n \to \infty \quad (TE) \end{cases} \tag{3.35}$$

The infinite series in (3.34) is slowly converging: thus, a large number of terms is required for accurate computation of the series. In all computations we have evaluated,

the summation from n=-40000 to 40000 and it provides convergence of the first three decimal places. The large order approximations for the Bessel products in (3.35) are used to reduce computation time. The approximation is used for n>100. Fast methods for evaluating (3.34) are proposed in [37] and [38] for $\phi_{sw} < 2$ and $b_n=1/n$, but these methods do not perform well for all values of ϕ_{sw}. The remaining infinite series in (3.28) and (3.30) are fast converging and can be truncated at approximately 200 terms (summation index ranging from -100 to +100). A plot of N required to achieve a truncation error less than 10^{-3} verses $2kb\phi_{sw}$ (2π times the segment arc length in wavelengths) is shown in Figure 3.3 for the TE IE/NS solution of various configurations of the eccentrically loaded cylinder with multiple slits. The results in Figure 3.3 show that the truncation number depends primarily on the segment length and is practically independent of eccentricity and the dimensions of the inner cylinder. Simple equations for calculating the value of N required for a truncation error less than 10^{-3} for the TE and TM IE/NS solutions are given in Table 3.1. The number of terms required for the IE/CBC solution varies dramatically with frequency as shown in Figure 3.4 for a TE IE/CBC solution of a loaded cylinder with a single slit [b = 1m, a = 0.8m, r_o = 0m, ϕ_o = 0, ϕ_{inc} = π, Ω_2 = (-5°,5°)] for a truncation error of $10^{-1.5}$. The IE/CBC truncation number for a given accuracy increases rapidly at frequencies just above the resonances of the structure.

Table 3.1. IE/NS truncation number N to achieve a truncation error less than 10^{-3}

Excitation	***N***
TM	$\lvert k_1\rvert b\phi_{sw}$+10
TE	$1.1\lvert k_1\rvert b\phi_{sw}$+9

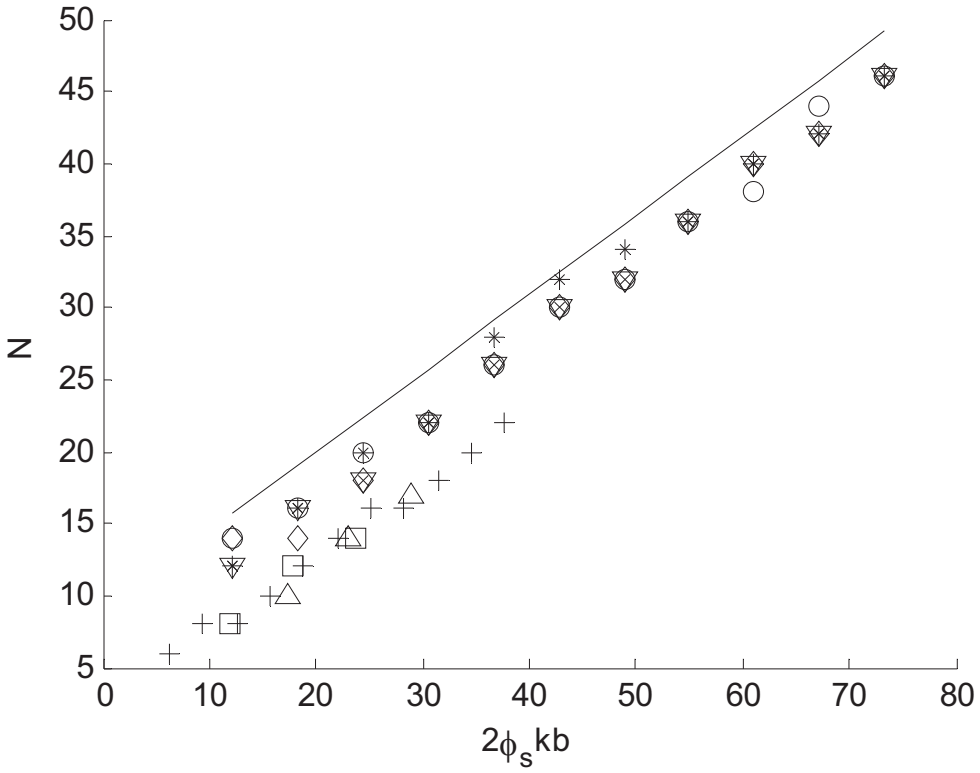

Figure 3.3. TE IE/NS truncation number N vs. $2kb\phi_{sw}$

* $a = 0.8$m, $b = 1$m, $r_o = 0$m, $\phi_o = 0$, $\phi_{inc} = \pi$, $\Omega_2 = (-5°, 5°)$

\+ $a = 0.8$m, $b = 1$m, $r_o = 0$m, $\phi_o = 0$, $\phi_{inc} = \pi$, $\Omega_2 = (-90°, 90°)$

× $a = 0.4$m, $b = 1$m, $r_o = 0$m, $\phi_o = 0$, $\phi_{inc} = \pi$, $\Omega_2 = (-5°, 5°)$

o $a = 0.1$m, $b = 1$m, $r_o = 0$m, $\phi_o = 0$, $\phi_{inc} = \pi$, $\Omega_2 = (-5°, 5°)$

◊ $a = 0.1$m, $b = 1$m, $r_o = 0.5$m, $\phi_o = 0$, $\phi_{inc} = \pi$, $\Omega_2 = (-5°, 5°)$

∉ $a = 0.1$m, $b = 1$m, $r_o = 0.5$m, $\phi_o = \pi$, $\phi_{inc} = \pi$, $\Omega_2 = (-5°, 5°)$

□ $a = 0.5$m, $b = 1$m, $r_o = 0.2$m, $\phi_o = 0$, $\phi_{inc} = \pi$, $\Omega_2 = (85°, 95°) \cup (-95°, -85°)$

Δ $a = 0.5$m, $b = 1$m, $r_o = 0.2$m, $\phi_o = 0$, $\phi_{inc} = \pi$, $\Omega_2 = (55°, 65°) \cup (175°, 185°) \cup (-55°, -65°)$

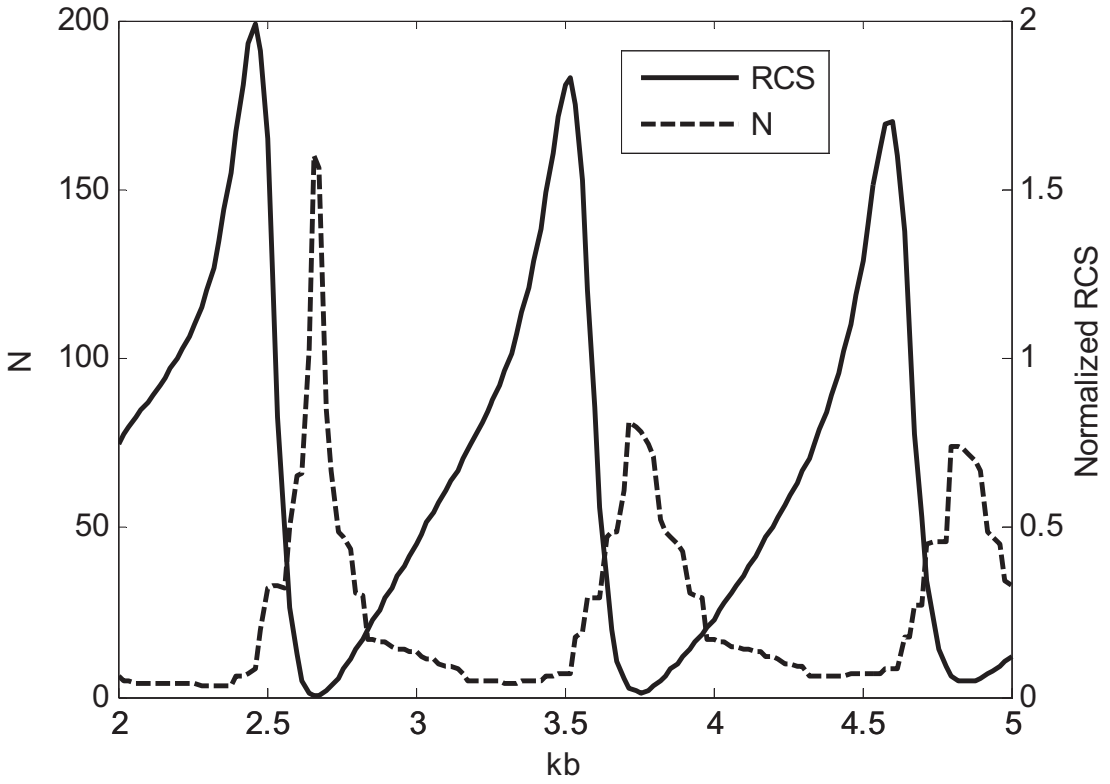

Figure 3.4. TE IE/CBC truncation number N (truncation error<$10^{-1.5}$) and normalized back scatter RCS vs. kb [a = 0.8m, b =1m, r_o = 0m, ϕ_o = 0, ϕ_{inc} = π, Ω_2 = (-5°, 5°)].

The IE/CBC and IE/NS formulations have been validated by comparing computed solutions using geometries considered in previously published results. Given a concentrically loaded cylinder with a single slit, the normalized backscattered RCS and total current induced on the inner conductor for TM incidence have been calculated using the IE/CBC and IE/NS techniques and compared to the results found in [21]. The normalized backscattered RCS for TE incidence has been compared to [20]. Excellent agreement is found with available data.

As previously shown, the IE/NS formulation provides faster convergence than the IE/CBC formulation, thus producing a more accurate solution for the same number of terms. In addition, the accuracy of the IE/CBC solution is found to be somewhat sensitive to the *g* parameter for certain geometries. Due to these advantages, the results shown here are all computed using the IE/NS formulation.

For the multiple slit geometries considered here, we assume that the slits are equally spaced around the cylinder. The azimuthal angles swept by the set of metal segments making up the slitted cylinder are defined by

$$\Omega_1 = \bigcup_{i=1}^{N_s} \left[(i-1)\frac{2\pi}{N_s} - \frac{\phi_1}{2N_s}, (i-1)\frac{2\pi}{N_s} + \frac{\phi_1}{2N_s} \right] \tag{3.36}$$

where ϕ_1 defines the total azimuthal angle swept by all of the metal segments. The angle of incidence in each of the following examples is assumed to be $\phi_{inc} = \pi/N_s$ so that a slit always faces the incoming wave, since larger RCS values are observed when the slit faces the incident wave [27] and [28]. For RCS comparison purposes, the total amount of metal formed by the segments and the total gap formed by the slits are both kept constant as the number of slits is varied. For each of the following examples, we have assumed the total angle swept by the metal segments is 300° leaving a total angle of 60° swept by the slits.

The variation of the backscattered RCS as the number of slits varies is shown in Figure 3.5 for TM illumination and Figure 3.6 for TE illumination. The TM low frequency RCS approaches that of a closed cylinder of radius *b* as the number of slits grows larger, since the outer cylinder becomes opaque to TM waves at these frequencies. The TE low frequency RCS approaches that of the inner cylinder as the number of slits

grows larger, since the outer cylinder becomes transparent to the TE waves at low frequencies. At higher frequencies, the internal coaxial resonances appear for both TM and TE excitations.

The variation of the backscattered RCS when the radius of the inner conductor relative to that of the outer conductor changes is shown in Figure 3.7 for TM illumination and Figure 3.8 for TE illumination. The smaller inner conductor radius yields a larger internal cavity which gives rise to resonances at lower frequencies. For the TM case, the larger internal cavity produces larger RCS values at certain resonances. In the TE case, two large resonances are observed for the smaller internal cavity over the given frequency range. Except for these TE resonances, the RCS of the smaller internal cavity is generally lower than that of the larger cavity.

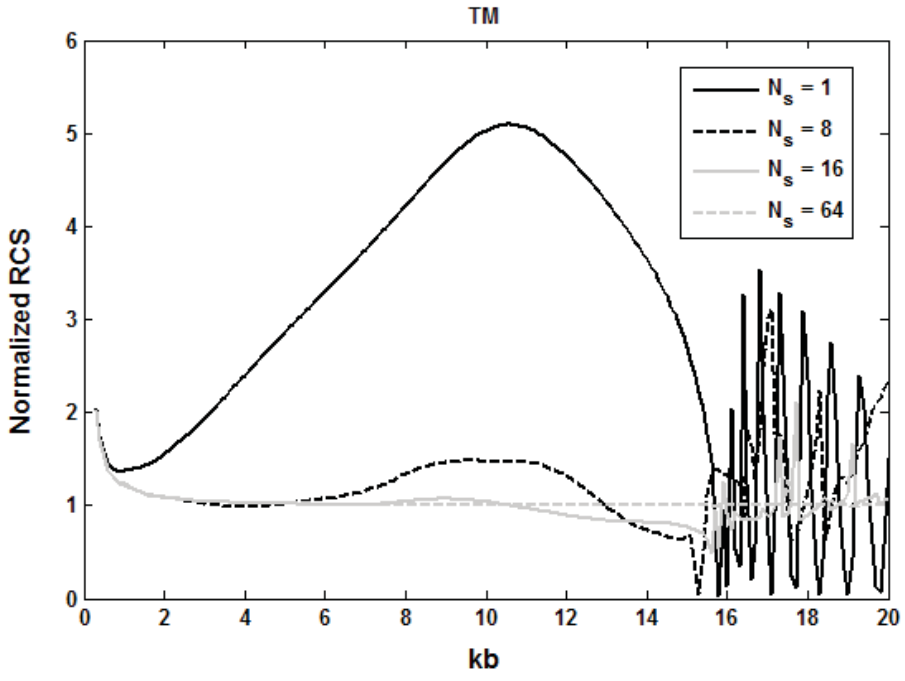

Figure 3.5. Normalized backscattered RCS (TM incidence) for different numbers of slits [$a = 0.8$m, $b = 1$m, $r_o = 0$m, $\phi_o = 0$, $\phi_{inc} = \pi/N_s$].

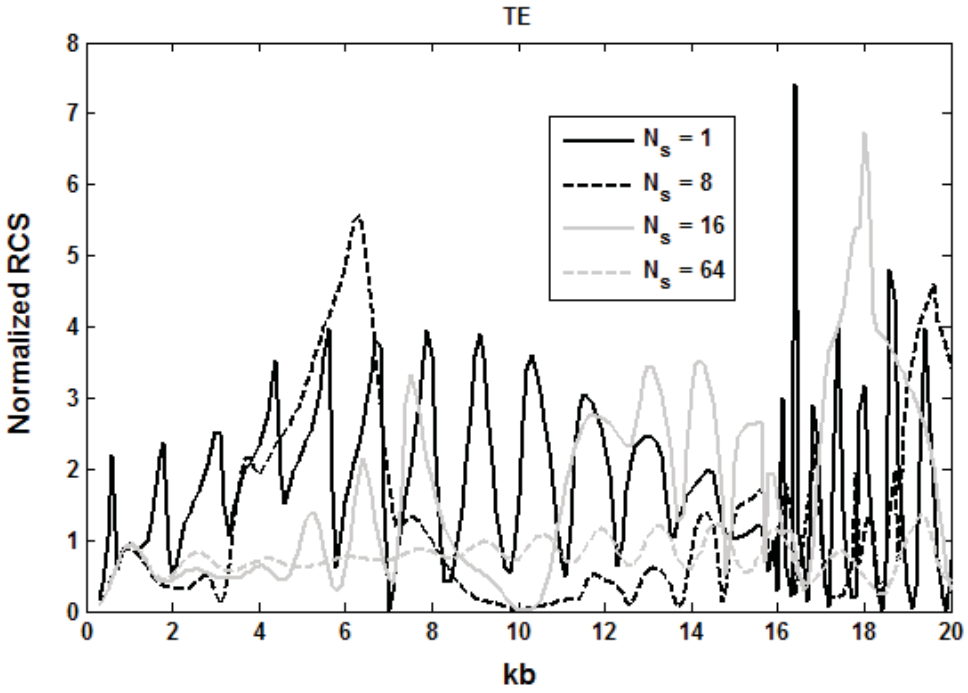

Figure 3.6. Normalized backscattered RCS (TE incidence) for different numbers of slits [a = 0.8m, b =1m, r_o = 0m, ϕ_o = 0, $\phi_{inc} = \pi/N_s$].

The effect of the inner conductor eccentricity on the backscattered RCS is shown in Figure 3.9 for the TM case and and Figure 3.10 for the TE case. Note that the inner conductor has been shifted from the center point in a direction opposite to that of the incoming wave. For TM illumination, the RCS is generally reduced as the eccentricity of the inner conductor is increased: while for TE illumination, significantly higher backscatter is seen at a large number of resonances.

The backscattered RCS variation when the eccentricity angle of the inner conductor is changed is shown in Figure 3.11 for the TM case and Figure 3.12 for the TE case. Note that the three eccentricity angles considered in these plots represent inner conductor shifts (1) toward the incoming incident wave, (2) perpendicular to the incoming incident wave and (3) away from the incoming incident wave. The eccentricity

angle produces a rather dramatic effect on the amplitude of the scatterer resonances in both the TM and TE cases.

The effect of the loading of the inner region with a lossy material is shown in Figure 3.13 for TM illumination and Figure 3.14 for TE illumination. The lossy dielectric and lossy magnetic materials considered here are those used in [27] and [28]. Both materials are found to significantly reduce the high frequency resonances in the TM case and resonances over the entire band in the TE case.

The IE/NS formulation is found to be computationally efficient. As an example, the overall computation time required for the problem defined by [N_s = 16, a = 0.5m, b = 1m, r_o= 0, ϕ_o= 0, ϕ_{inc} = π] using MATLAB on a personal computer with a 2.53 GHz processor and 3GB of RAM is less than 22 seconds.

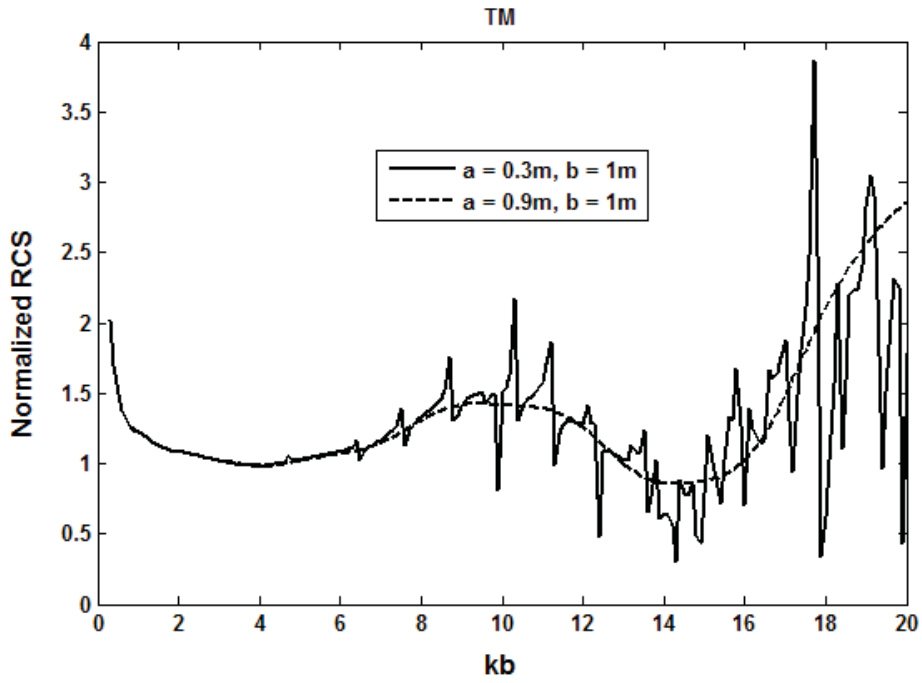

Figure 3.7. Normalized backscattered RCS (TM incidence) for different inner conductor radii [N_s = 8, r_o = 0m, ϕ_o = 0, ϕ_{inc} = π/8].

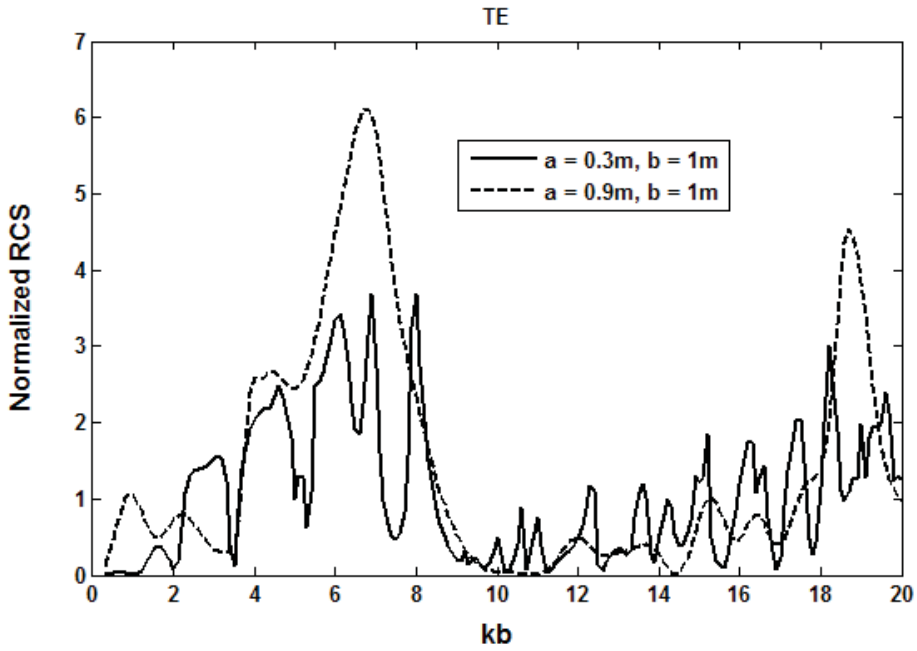

Figure 3.8. Normalized backscattered RCS (TE incidence) for different inner conductor radii [$N_s = 8$, $r_o = 0$m, $\phi_o = 0$, $\phi_{inc} = \pi/8$].

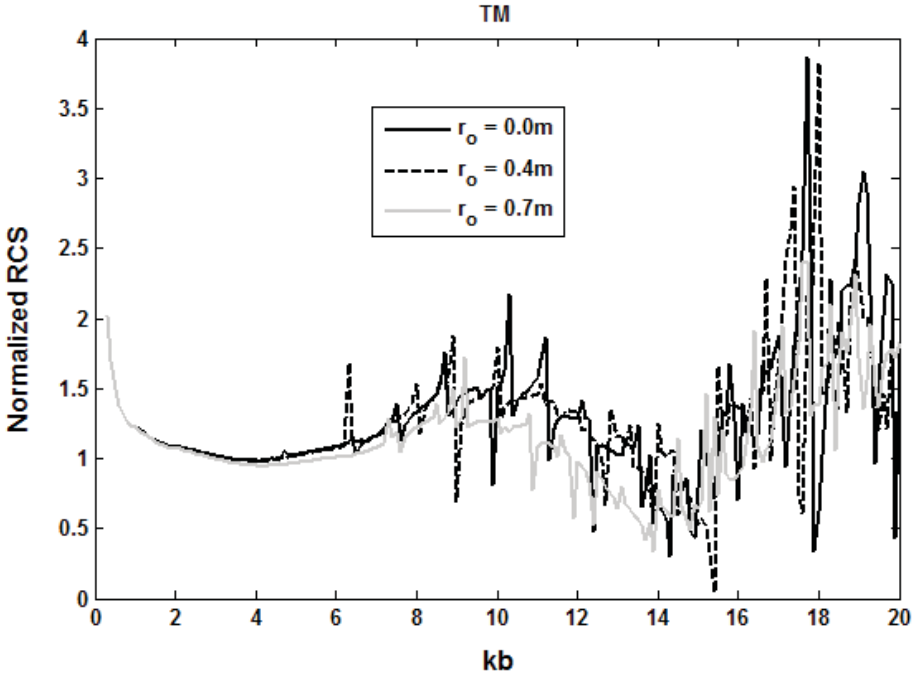

Figure 3.9. Normalized backscattered RCS (TM incidence) for different eccentricity radii [$a = 0.3$m, $b = 1$m, $N_s = 8$, $r_o = 0$m, $\phi_{inc} = \pi/8$, $\phi_o = 9\pi/8$].

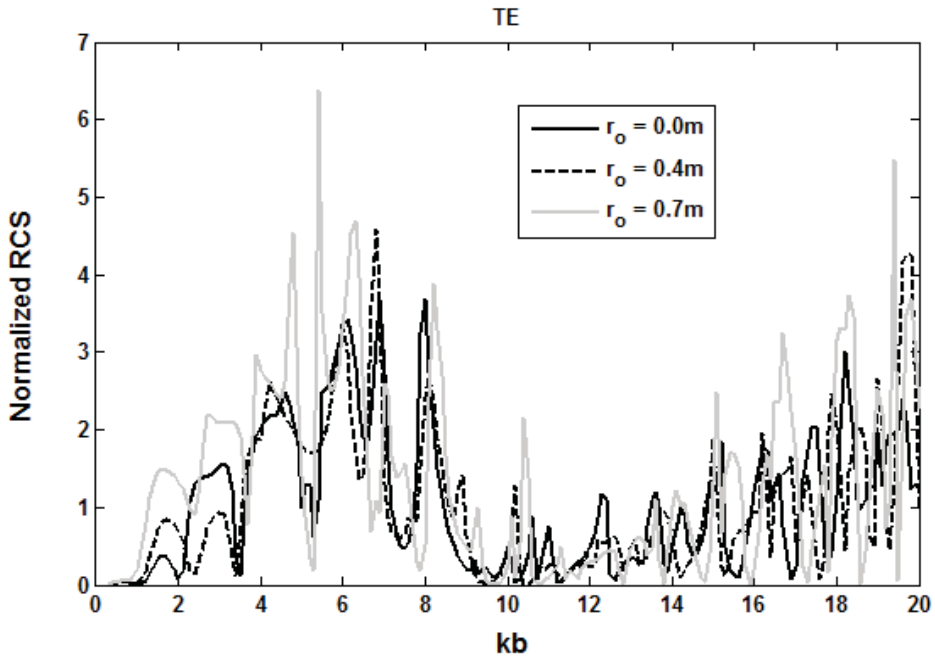

Figure 3.10. Normalized backscattered RCS (TE incidence) for different eccentricity radii [a = 0.3m, b =1m, N_s = 8, r_o = 0m, ϕ_{inc} = π/8, ϕ_o = 9π/8].

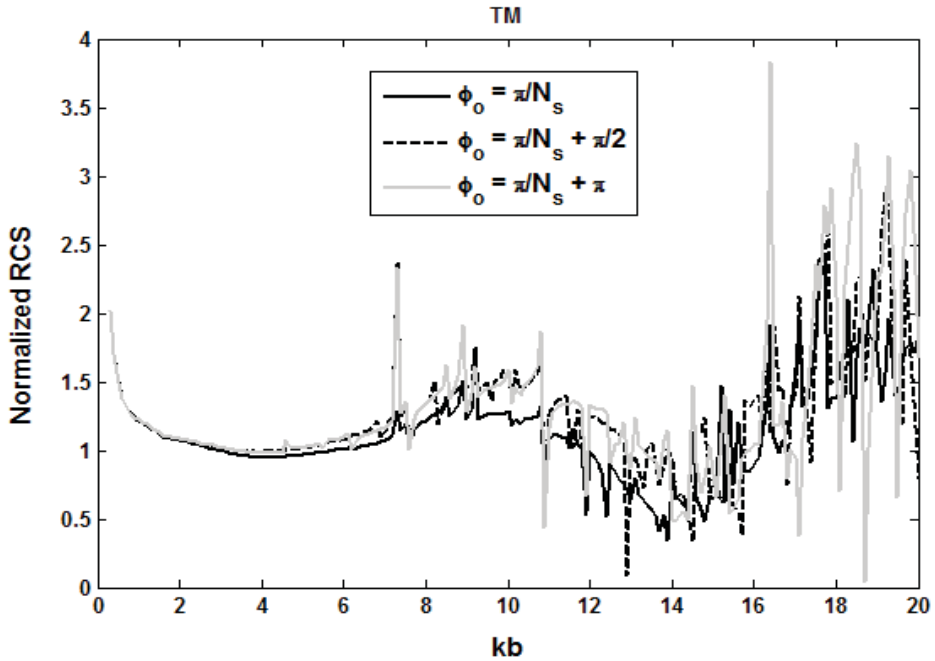

Figure 3.11. Normalized backscattered RCS (TM incidence) for different eccentricity angles [a = 0.3m, b =1m, N_s = 8, r_o = 0.7m, ϕ_{inc} = π/8].

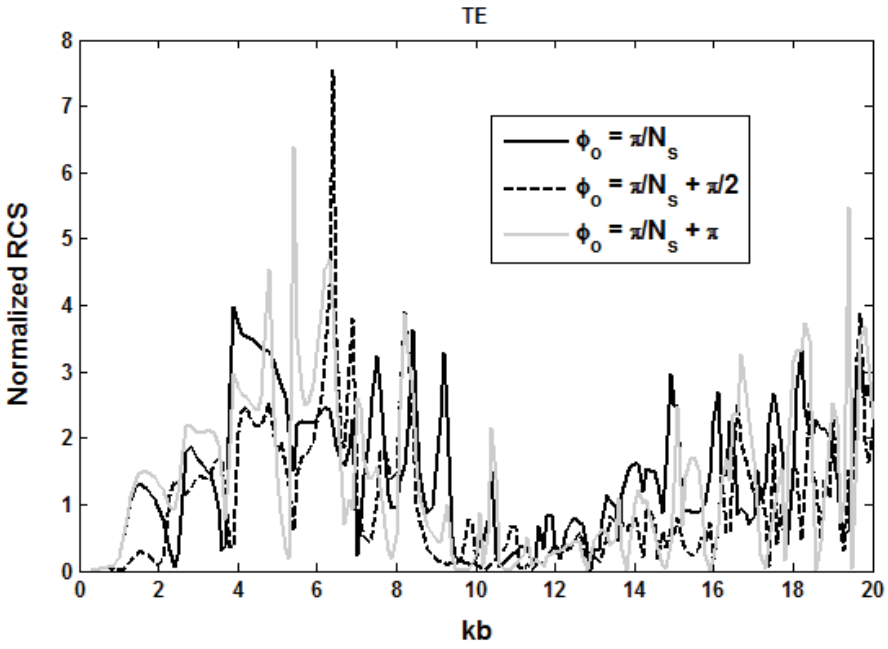

Figure 3.12. Normalized backscattered RCS (TE incidence) for different eccentricity angles [a = 0.3m, b =1m, N_s = 8, r_o = 0.7m, ϕ_{inc} = π/8].

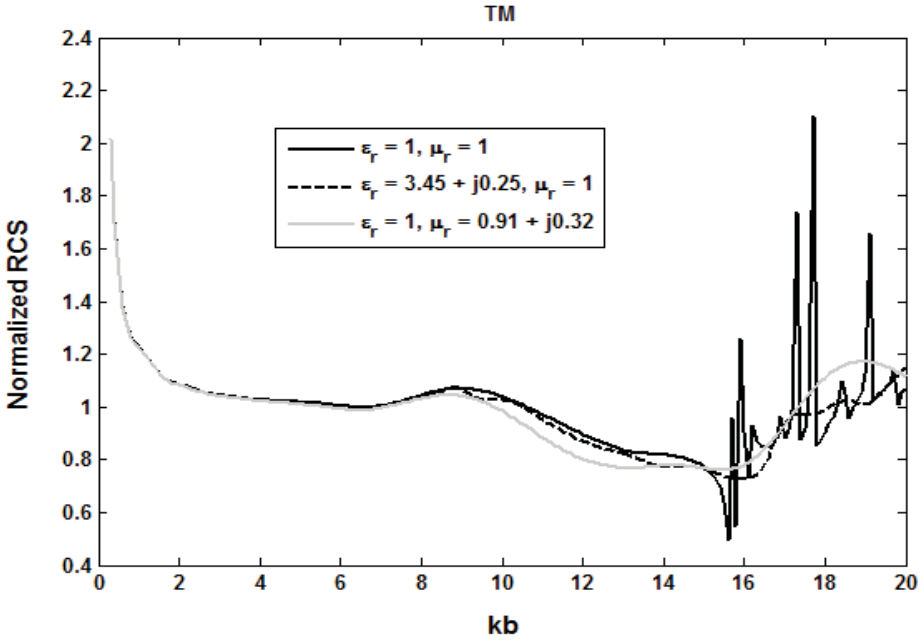

Figure 3.13. Normalized backscattered RCS (TM incidence) for different loading materials [a = 0.8m, b =1m, N_s = 16, r_o = 0m, ϕ_o = 0, ϕ_{inc} = π/16].

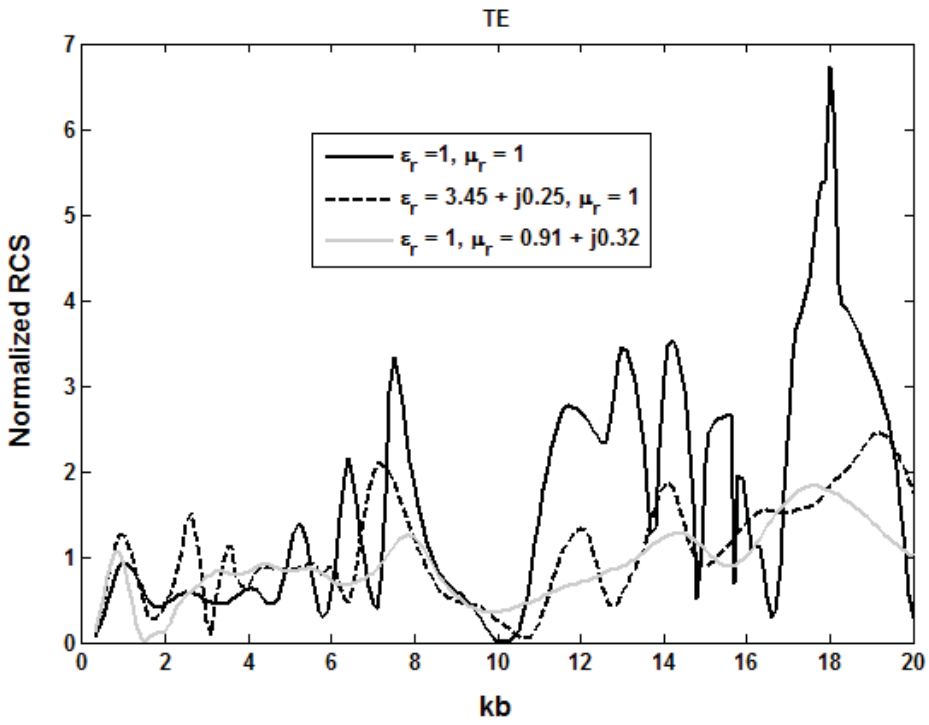

Figure 3.14. Normalized backscattered RCS (TE incidence) for different loading materials [a = 0.8m, b =1m, N_s = 16, r_o = 0m, ϕ_o = 0, ϕ_{inc} = π/16].

CHAPTER IV

A FAST METHOD FOR CALCULATING SCATTERING FROM DIELECTRIC LOADED PEC SEMICIRCULAR CYLINDER AND STRIP

4.1 Introduction

Scattering from a thin strip and a semicircular cylinder has drawn substantial attention in the literature, with a comprehensive list of references found in [39]. Previous related work includes, scattering from a dielectric loaded strip via eigenfunction expansion and mode matching by Elsherbeni [40], scattering from an unloaded semicircular cylinder using a hybrid MOM approach by Srikanth [41], low frequency scattering from a dielectric loaded semicircular cylinder by Hurd using an integral equation approximation [42], and a fast method for evaluating the matrix coefficients for the strip and complementary slit as presented by Tsalamengas [43].

In this chapter, we present an efficient method to analyze a dielectric loaded strip and semicircular cylinder using a Neumann series. The method presented here is an extension to our earlier work where the current density was expanded on an unclosed metallic circular cylinder in terms of a Neumann series to study scattering from an eccentrically loaded cylinder with multiple slits [44]. In this work, a Neumann series is used to expand the tangential electric field on the circle bounding the scatterer to obtain the solution. The advantages offered by the Neumann series include faster convergence

and easy computation of matrix coefficients. In the present method, the matrix coefficients consisting of infinite series are computed more efficiently when compared to the integral evaluations necessary for the MOM solution. The proposed method works efficiently from very low to high frequency.

4.2 Geometry of the Problem

The geometries of the PEC strip and the PEC semicircular cylinder loaded with semicircular dielectric cylinders are shown in Figure 4.1 illuminated by either an axially polarized source (TM to z plane wave or z-directed electric line source) or a transversely polarized source (TE to z plane wave or z-directed magnetic line source) at an incident angle of ϕ_{inc} [line source is located at (r_{inc}, ϕ_{inc})]. For either geometry, the scatterer and the surrounding space is divided into three regions (a) Region 1 ($r > a$), (b) Region 2 ($r < a$ and $x > 0$), and (c) Region 3 ($r < a$ and $x < 0$). Region 1 is assumed to be free space, while regions 2 and 3 are characterized by relative permittivities ε_{r2} and ε_{r3} for the strip geometry. Region 3 is a PEC for the semicircular cylinder geometry. The electric/magnetic fields in the three regions are denoted by $u_1(r,\phi)$, $u_2(r,\phi)$ and $u_3(r,\phi)$ for the axial/transverse source polarizations, respectively. The scattering solution for the semicircular cylinder problem is obtained by setting $u_3 = 0$. The time dependence assumed here is $\exp(-j\omega t)$. The fields u_1, u_2 and u_3 can be expressed in cylindrical harmonics as follows:

$$u_1(r,\phi) = \sum_{n=-\infty}^{\infty}[a_n J_n(kr) + b_n H_n^{(1)}(kr)]e^{jn\phi}, \tag{4.1}$$

$$u_2(r,\phi) = \sum_{n=-\infty}^{\infty} c_n J_n(k_2 r)[e^{jn(\phi-\pi/2)} \mp e^{-jn(\phi-\pi/2)}], \tag{4.2}$$

$$u_3(r,\phi) = \sum_{n=-\infty}^{\infty} d_n J_n(k_3 r)[e^{jn(\phi-\pi/2)} \mp e^{-jn(\phi-\pi/2)}]. \tag{4.3}$$

where $J_n(kr)$ and $H_n^{(1)}(kr)$ are Bessel and Hankel functions of the first kind, k, k_2, and k_3 are the wave numbers in the three regions, and b_n, c_n and d_n are unknown amplitude coefficients. The plus and minus signs in Eqs. (4.2) and (4.3) are associated with the transverse and axial source polarizations, respectively. The a_n coefficient for the given excitation can be expressed as

$$a_n = \begin{cases} e^{-jn\phi_{inc}} H_n^{(1)}(kr_{inc}) & \text{line source} \\ j^{-n} e^{-jn\phi_{inc}} & \text{plane wave}. \end{cases} \tag{4.4}$$

Note that the selection of u_2 and u_3 satisfies the requirement of zero tangential electric field on the flat side of the structure.

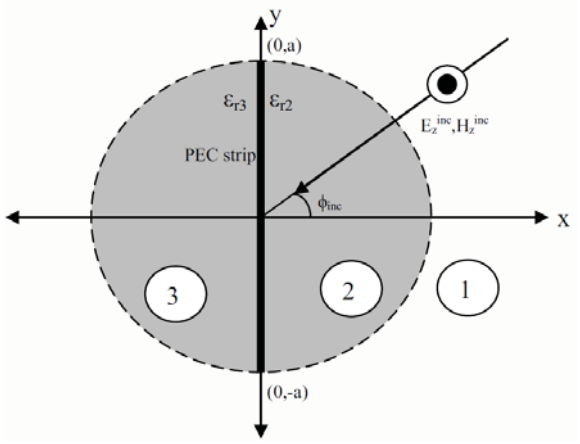

(a)

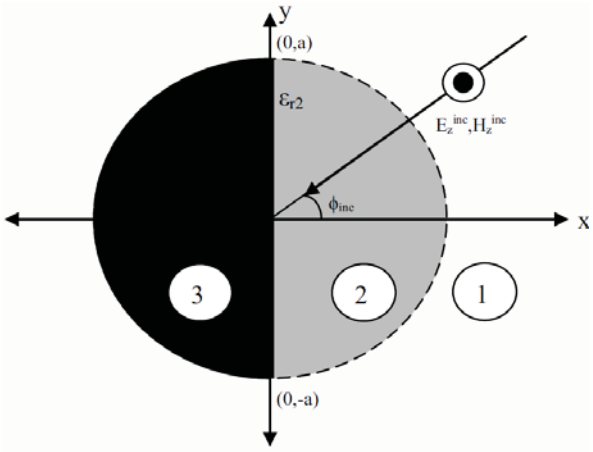

(b)

Figure 4.1. TE/TM plane wave incident on (a) a dielectric loaded strip and (b) a dielectric loaded semicircular cylinder.

4.3 Neumann series solution of the problem

The electric field Fourier coefficient on the circle surrounding the scatterer is expressed in terms of a Neumann series as

$$c_n X_n e^{-jn\pi/2} = \sum_{p=0}^{\infty} \chi_p^1 J_{p+v}(n\pi/2)/(n\pi/2)^v \tag{4.5}$$

$$d_n Y_n e^{jn\pi/2} = \sum_{p=0}^{\infty} \chi_p^2 J_{p+v}(n\pi/2)/(n\pi/2)^v \tag{4.6}$$

$$a_n U_n + b_n V_n = \sum_{p=0}^{\infty} (\chi_p^1 + e^{-jn\pi}\chi_p^2)\frac{J_{p+v}(n\pi/2)}{(n\pi/2)^v} \tag{4.7}$$

where X_n, Y_n, U_n and V_n are functions defined in Table 4.1. The fields in regions 1, 2, and 3 is written as

$$\begin{aligned} u_1(r,\phi) &= \sum_{n=-\infty}^{\infty} a_n\left(J_n(kr) - \frac{U_n}{V_n}H_n^{(1)}(kr)\right)e^{jn\phi} \\ &+ \sum_{n=-\infty}^{\infty}\frac{H_n^{(1)}(kr)}{V_n}\sum_{p=0}^{\infty}(\chi_p^1 + e^{-jn\pi}\chi_p^2)\frac{J_{p+v}(n\pi/2)}{(n\pi/2)^v}e^{jn\phi}, \end{aligned} \tag{4.8}$$

$$\begin{aligned} u_2(r,\phi) &= \sum_{n=-\infty}^{\infty}\frac{J_n(k_2 r)}{X_n}\sum_{p=0}^{\infty}\chi_p^1\frac{J_{p+v}(n\pi/2)}{(n\pi/2)^v} \\ &\times\left(e^{jn\phi} - e^{-jn(\phi-\pi)}\right), \end{aligned} \tag{4.9}$$

$$\begin{aligned} u_3(r,\phi) &= \sum_{n=-\infty}^{\infty}\frac{J_n(k_3 r)}{Y_n}\sum_{p=0}^{\infty}\chi_p^2\frac{J_{p+v}(n\pi/2)}{(n\pi/2)^v} \\ &\times\left(e^{-jn\pi}e^{jn\phi} - e^{-jn\phi}\right). \end{aligned} \tag{4.10}$$

Continuity of the tangential magnetic field at $r = a$ must also be enforced. For axial source polarizations, Eqs. (4.8), (4.9), and (4.10) must be differentiated with respect to r to obtain the tangential magnetic fields at the interface between regions 1 and 2, and regions 1 and 3. The expansion coefficients are calculated using the orthogonality of the Gegenbauer polynomials by multiplying the magnetic fields in regions 1 and 2 with $[1-(2\phi/\pi)^2]^{v-1/2}C_m^v(2\phi/\pi)$, integrating with respect to ϕ from $-\pi/2$ to $\pi/2$ and equating the resulting equations. This manipulation yields Eq. (4.11) while applying the same procedure to the regions 1 and 3 interface yields Eq. (4.12).

$$
\begin{aligned}
&-\sum_{p=0}^{\infty}\chi_p^2\sum_{n=-\infty}^{\infty}\frac{W_n}{V_n}\frac{e^{-jn\pi}J_{p+1}(n\pi/2)J_{m+1}(n\pi/2)}{(n\pi/2)^2}\\
&\sum_{p=0}^{\infty}\chi_p^1\sum_{n=-\infty}^{\infty}\frac{J_{p+v}(n\pi/2)J_{m+v}(n\pi/2)}{(n\pi/2)^{2v}}\left\{-\frac{W_n}{V_n}+\frac{K_n}{X_n}\times\right.\\
&\left.\left(1-(-1)^{m+n}\right)\right\}=\sum_{n=-\infty}^{\infty}\frac{a_n f_n}{V_n}\frac{J_{m+1}(n\pi/2)}{(n\pi/2)},
\end{aligned}
\tag{4.11}
$$

$$
\begin{aligned}
&\sum_{n=-\infty}^{\infty}a_n\frac{f_n}{V_n}e^{jn\pi}\frac{J_{m+v}(n\pi/2)}{(n\pi/2)}=\sum_{p=0}^{\infty}\chi_p^2\times\\
&\sum_{n=-\infty}^{\infty}\frac{J_{p+v}(n\pi/2)J_{m+v}(n\pi/2)}{(n\pi/2)^{2v}}\\
&*\left\{-\frac{W_n}{V_n}+\frac{L_n}{X_n}(1-(-1)^m e^{jn\pi})\right\}\\
&-\sum_{p=0}^{\infty}\chi_p^1\sum_{n=-\infty}^{\infty}\frac{W_n}{V_n}e^{jn\pi}\frac{J_{p+v}(n\pi/2)J_{m+v}(n\pi/2)}{(n\pi/2)^{2v}}
\end{aligned}
\tag{4.12}
$$

where the coefficients f_n , W_n , K_n and L_n are given in Table 4.1. Solutions of the linear systems in Eq. (4.11) and (4.12) yield the coefficients χ_p^1 and χ_p^2. For the semicircular cylinder scatterer, the coefficient χ_p^2 is set to zero and the linear system in Eq. (4.11) is solved for χ_p^1. The values of v determined from the edge conditions in [45] for the PEC strip and the PEC semicircular cylinder are given in Table 4.2. Thus, the tangential electric field on the circular boundary at $r = a$ for either scatterer automatically satisfies the required edge condition for either source polarization. For example, given the PEC strip, the tangential electric field components on the circular boundary (E_z for the axially polarized source or E_ϕ for the transversely polarized source) tend to zero as $[\phi-\pi/2]^{x/2}$ near the upper edge at $(a, \phi/2)$ and $[\phi+\pi/2]^{x/2}$ near the lower edge at $(a, -\phi/2)$, where $x = 1$ for the transversely polarized source and $x = -1$ for the axially polarized source. This edge condition also satisfies the appropriate edge condition for the tangential magnetic field (see Appendix C for a proof given an axially polarized source). The corresponding

proof assuming a transversely polarized source can be derived by following a similar procedure.

4.4 Numerical Result

The infinite series computations in Eqs. (4.11) and (4.12) are performed using the procedure described in [44]. To determine the convergence properties of the Neumann series solution, we define the truncation error as

$$e(N) = \left\| b_n(N+1) - b_n(N) \right\| \tag{4.13}$$

where $b_n(N)$ is the scattered field coefficient for region 1 calculated using N coefficients of χ_p^1 and χ_p^2. The truncation errors for the loaded and unloaded strip under TM and TE illumination are shown in Figure 4.2 and exhibit significant coefficient decay. The unloaded and loaded strips require only 16 and 25 terms, respectively, to achieve a truncation error less than 10^{-4} for $ka = 5$ given either TM or TE excitation. For all of the following comparisons of the Neumann series solution to published results, the value of N is selected to yield a truncation error $< 10^{-4}$. The back scattered field for a dielectric loaded semicircular cylinder is compared with [42] in Figure 4.3. The current density on an unloaded strip of length 6λ given a normally incident TE plane wave is compared with [46] in Figure 4.4. The current density magnitude on an unloaded strip of length 0.1λ given a normally incident TM plane wave is compared with [47] in Figure 4.5. All results match well and validate the proper edge behavior for current density. In Figure 4.6, the current density on the top-half of the strip of width 6λ for normal incidence is presented. The non-physical oscillatory behavior demonstrated in [49] and reported in [46] is not present in Neumann series solution and can be seen from Figure 4.5 and Figure 4.6.

Computation times for different unloaded strip widths under normal TE/TM incidence are compared in Table 4.3, where the solutions were coded in MATLAB on a 3.4 GHz Pentium IV with 4GB RAM. The results given in Table 4.3 show the efficiency of the solution scheme.

Table 4.1. Coefficients for the Neumann Series Solution.

Coefficient	**Axial Source**	**Transverse Source**
X_n	$J_n(k_2 a)$	$k_2 J_n'(k_2 a)/\varepsilon_{r2}$
Y_n	$J_n(k_3 a)$	$k_3 J_n'(k_3 a)/\varepsilon_{r3}$
U_n	$J_n(ka)$	$kJ_n'(ka)$
V_n	$H_n^{(1)}(ka)$	$kH_n^{(1)}{}'(ka)$
f_n	$-2jk/\pi ka$	$2jk/\pi ka$
W_n	$kH_n^1{}'(ka)$	$H_n^1(ka)$
K_n	$k_2 J_n'(k_2 a)$	$J_n(k_2 a)$
L_n	$k_3 J_n'(k_3 a)$	$J_n(k_3 a)$

Table 4.2. Values of v to satisfy the scatterer edge conditions.

Scatterer	Axial Source	Transverse Source
Strip	1	0
Semicircular Cylinder	7/6	1/6

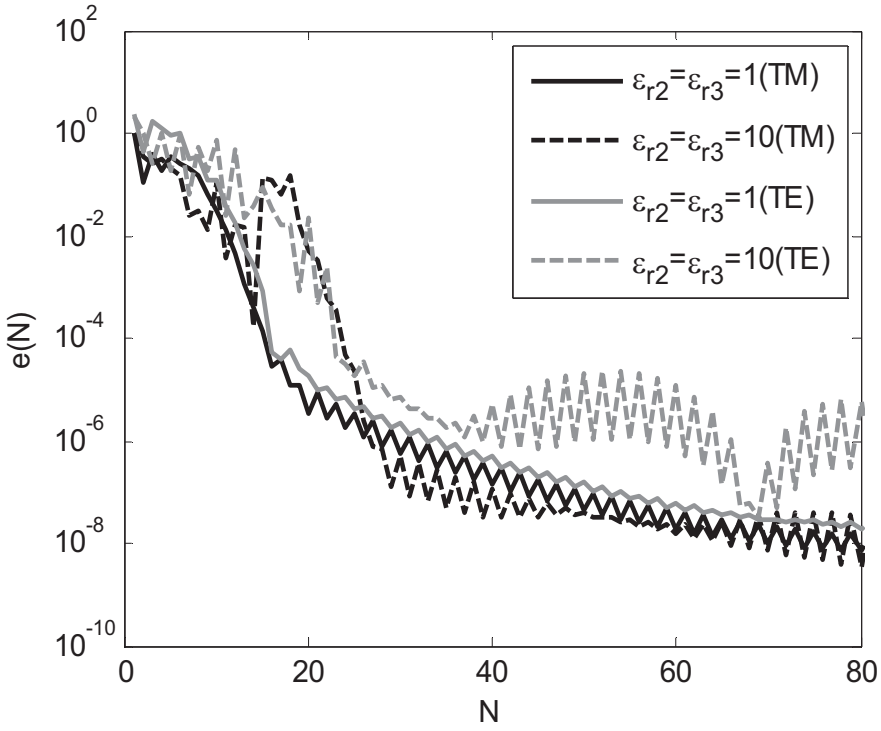

Figure 4.2. Truncation error versus N (TE case) for a dielectric loaded strip with, ka=5 and $\phi_{inc}=\pi/4$.

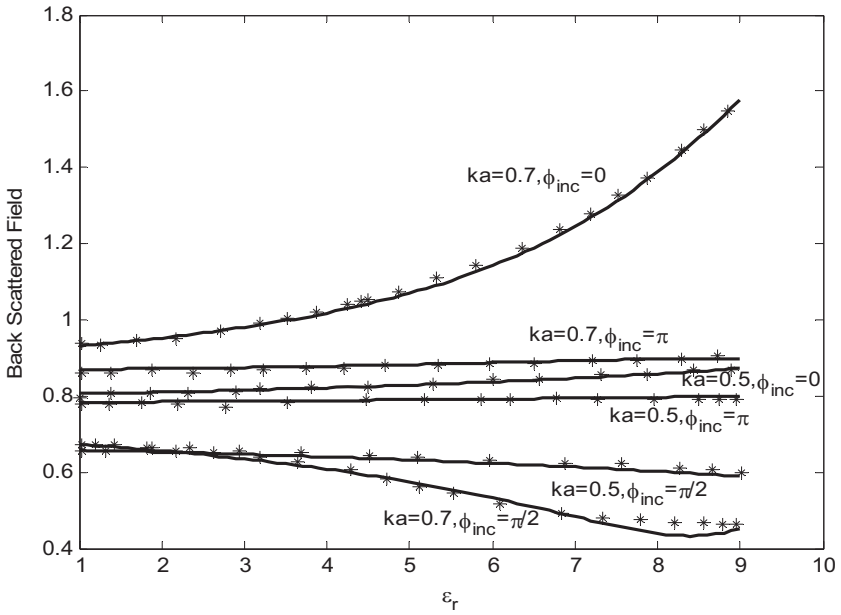

Figure 4.3. Back scattered field versus ε_{r2} for a dielectric loaded semicircular cylinder for TM incidence. (1) Solid line-the proposed method. (2) Asterick-Ref [42].

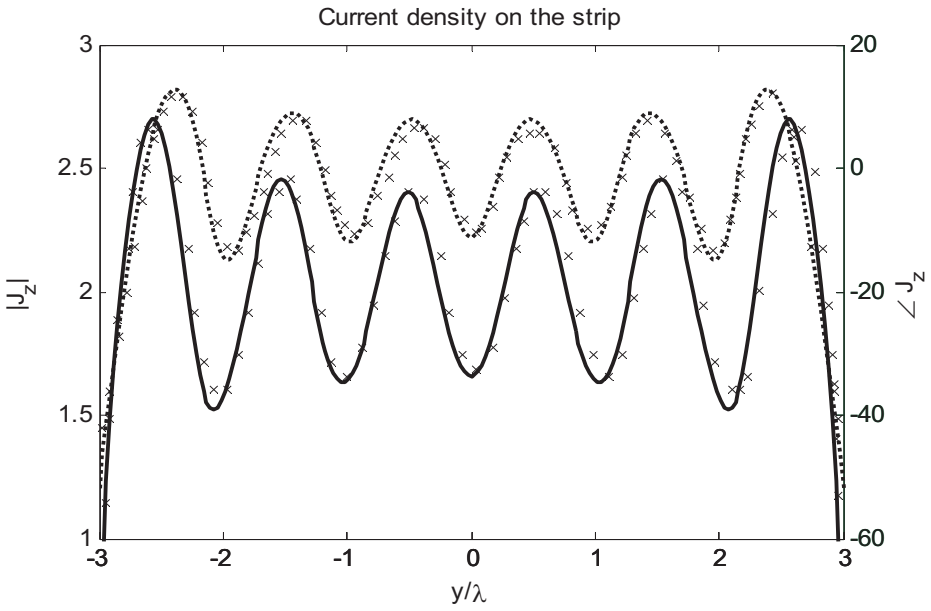

Figure 4.4. Axial Current density on the surface of the unloaded strip with of with 6λ and ϕ_{inc}=0 with TE incidence (1) solid/dotted line the proposed method (2) Astericks – Ref [46].

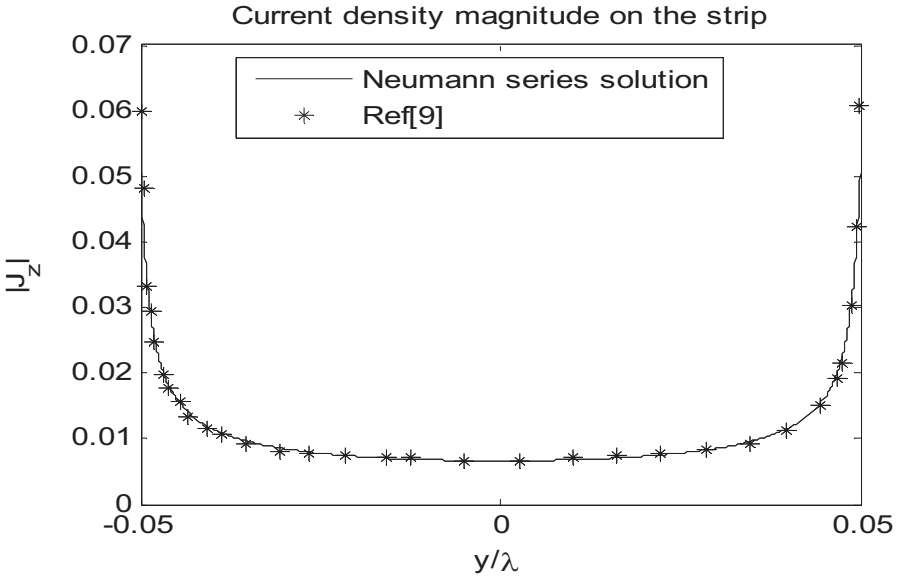

Figure 4.5. Current density on the surface of an unloaded strip of length 0.1λ under TM plane wave illumination with ϕ_{inc} = 0°.

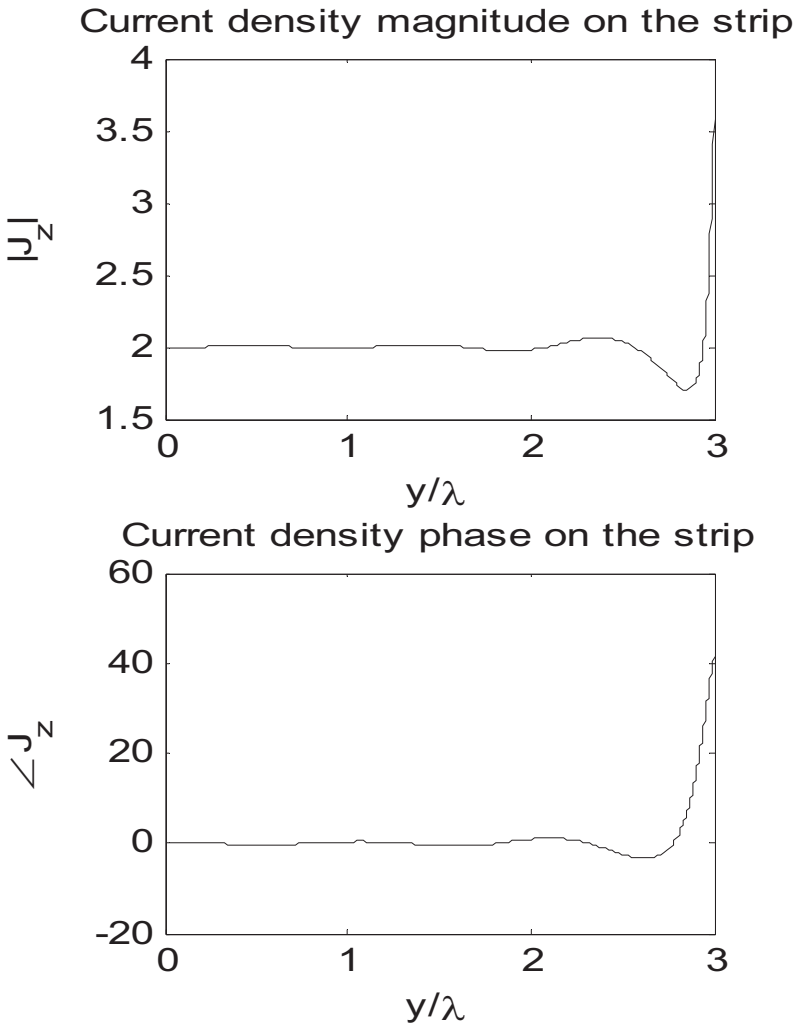

Figure 4.6. Current density on the surface of an unloaded strip of length 6λ under TM plane wave illumination with $\phi_{inc} = 0°$.

Table 4.3. Computation times for unloaded strips of various widths under normal TE or TM plane wave incidence

Strip Width (λ)	Computation Time (sec)		Number of Terms used
	TM	TE	
1λ	3	3	15
5λ	6	5	40
10λ	7	6	60

CHAPTER V

SCATTERING FROM A SLOTTED CYLINDER WITH AN INTERIOR WEDGE

5.1 Introduction

In this chapter we present the application of Neumann series for calculating scattering from a slotted cylinder with an interior wedge. Intially, we solve the problem of a knife edge inside an unclosed cylinder which is a limiting case of wedge. In order to solve the problem, we expand the field in the outer region on the Riemann surface and apply the procedure followed in CHAPTER IV, as illustrated in sections 5.2 and 5.3. The field expansion on the Riemann surface method can only be applied to a knife edge. The general problem of a wedge is solved by using the Fourier expansion of the Gegenbauer polynomial with different periodicity; as shown in 5.4 and 5.5.

5.2 Geometry of the problem

The geometry of the slotted cylinder loaded with knife edge is shown in Figure 5.1. The radius of the cylinder is denoted by a. A metallic strip extends from the center of the coordinate axis and touches the cylinder at ($-a$,0). Both the cylinder and inner strip are PECs and infinitesimally thin. The slit on the cylinder occupies the angular position ($-\phi_s+\phi_{sc}, \phi_s+\phi_{sc}$).

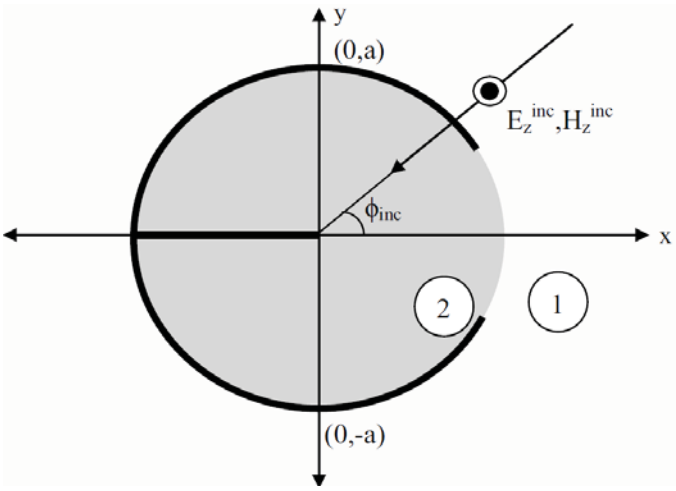

Figure 5.1. Geometry of the slotted cylinder loaded with knife edge.

We assume there is only one slit on the cylinder even though the method presented here is applicable to multiple slit configurations. For the purpose of analysis, the entire space is divided into two regions, region 1 (r>a) and region 2 (r<a). The relative dielectric constants of region 1 and region 2 are given by ε_{r1} and ε_{r2}. The structure is illuminated by a TM to z (electric field parallel to z-axis) or TE to z (magnetic field parallel to z-axis) plane wave incident at an angle of ϕ_{inc}. The time dependence assumed here is exp(-jωt). The fields in regions 1 and 2 are given by $u_1(r,\phi)$ and $u_2(r,\phi)$ and can be expressed in cylindrical harmonics as:

$$u_1(r,\phi) = \sum_{n=-\infty}^{\infty} a_n J_n(kr) e^{jn\phi} + b_n H_n^1(kr) e^{jn\phi} \tag{5.1}$$

$$u_2(r,\phi) = \sum_{n=-\infty}^{\infty} c_n J_{\left|\frac{n}{2}\right|}(k_1 r)\left(e^{j\frac{n}{2}\phi} \mp e^{-j\frac{n}{2}(\phi-2\pi)} \right) \tag{5.2}$$

where $J_n(kr)$ and $H_n^1(kr)$ are Bessel and Hankel function of the first kind. 'k' and 'k_1' are the wave numbers of regions 1 and 2. In Eq. (5.2) the plus and minus signs correspond to

the TE and TM cases, respectively. The solution is obtained by determining the unknown coefficients b_n and c_n. The coefficient a_n depends on the excitation and is given by

$$a_n = \begin{cases} e^{-jn\phi'} H_n^1(kr') & \text{Line source} \\ j^{-n} e^{-jn\phi_{inc}} & \text{Plane Wave} \end{cases} \tag{5.3}$$

where *(r',ϕ')* is the position of the line source in cylindrical coordinates. The above selection of $u_2(r,\phi)$ automatically satisfies the requirement of the zero tangential electric field on the inner strip. The coefficients b_n and c_n must satisfy continuity of the electric and magnetic fields in the slit at r=a while also satisfying the requirement of zero tangential electric field on the PEC cylinder. In order to apply the Neumann series method applied earlier to an eccentrically loaded cylinder, strip, and semicircular cylinder, the field in regions 1 and 2 need to be of the same periodicity. The field u_1 in Eq. (5.1) has a period of 2π, while the field u_2 in Eq. (5.2) has period of 4π. To solve the problem of scattering from a slotted cylinder with an interior knife edge, we consider the equivalent problem of scattering from a slotted cylinder with an interior knife edge placed on a Riemann double space, as shown in Figure 5.2. The entire space is divided into three regions:

- Region 1 (Riemann Surface I, Riemann Surface II and r>a)
- Region 2 (Riemann Surface I, r<a).
- Region 3 (Riemann Surface II, r<a).

The branch cut joining the two Riemann surfaces is along the negative real axis (the branch cut can be along any radial line from origin to infinity). The fields in the three regions are denoted by $u_1(r,\phi)$, $u_2(r,\phi)$, and $u_3(r,\phi)$, respectively.

$$u_1(r,\phi) = \sum_{n=-\infty}^{\infty} 0.5 a_{\frac{n}{2}}' J_{\left|\frac{n}{2}\right|}(kr) e^{j\frac{n}{2}\phi} + b_n H^1_{\left|\frac{n}{2}\right|}(kr) e^{j\frac{n}{2}\phi} \tag{5.4}$$

$$u_2(r,\phi) = \sum_{n=-\infty}^{\infty} c_n J_{\left|\frac{n}{2}\right|}(k_1 r) \left(e^{j\frac{n}{2}\phi} \mp e^{-j\frac{n}{2}(\phi - 2\pi)} \right) \tag{5.5}$$

$$u_3(r,\phi) = \sum_{n=-\infty}^{\infty} d_n J_{\left|\frac{n}{2}\right|}(k_1 r) \left(e^{j\frac{n}{2}\phi} \mp e^{-j\frac{n}{2}(\phi - 2\pi)} \right) \tag{5.6}$$

where a_n' is related to a_n by

$$a_n' = \begin{cases} a_n & n > 0 \\ (-1)^n a_n & otherwise \end{cases} \tag{5.7}$$

and b_n, c_n, and d_n are the unknown coefficients to be determined such that the continuity of the tangential electric and magnetic field across all interfaces are satisfied, and . Also, the requirement of the zero tangential electric field on the outer cylinder should be enforced. The fields u_1, u_2, and u_3 represent the E_z/H_z component for TM/TE incidence. The minus and plus sign in Eq. (5.5) and (5.6) are for TM and TE case, respectively. The summation of the fields on Riemann surfaces I and II gives the solution to the problem. This is explained as follows:

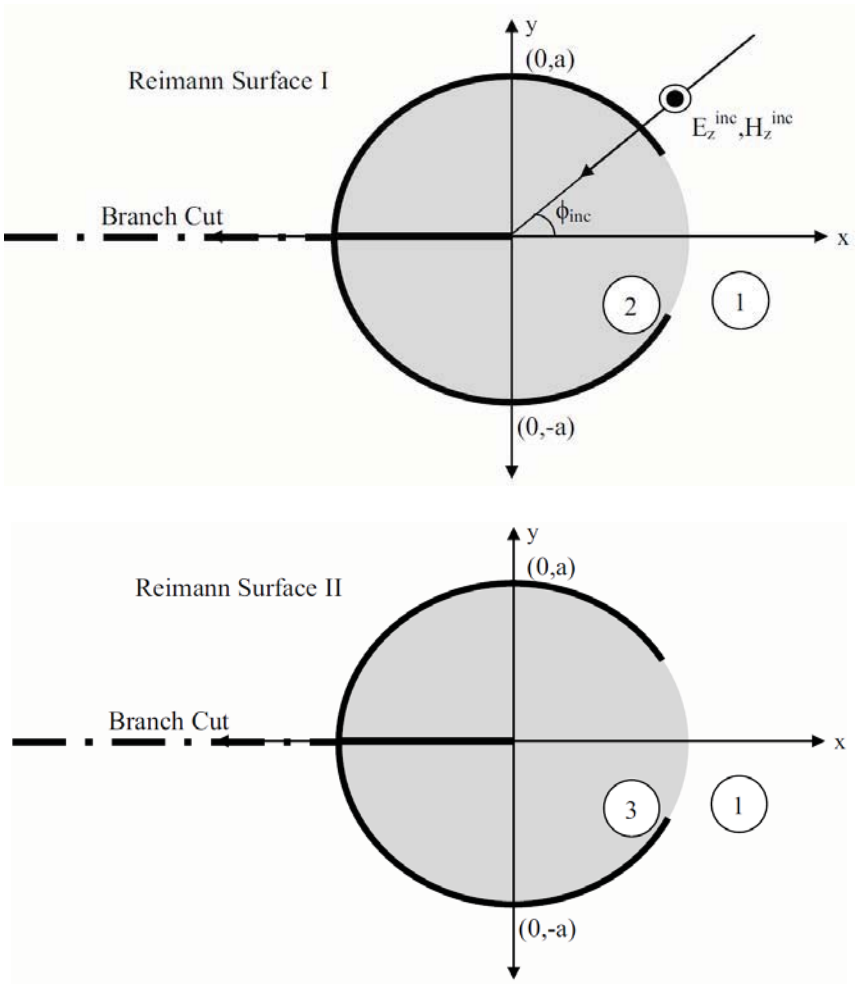

Figure 5.2. Equivalent problem on the Reimann 2 space.

- The summation of the incident field on the two Riemann surfaces becomes the incident field for the original problem.

$$u_{inc} = \sum_{n=-\infty}^{\infty} 0.5 a_{\frac{n}{2}}' J_{\left|\frac{n}{2}\right|}(kr)(e^{j\frac{n}{2}\phi} + e^{j\frac{n}{2}(\phi+2\pi)}) \\ = \sum_{k=-\infty}^{\infty} a_k' J_{|k|}(kr)e^{jk\phi} = \sum_{k=-\infty}^{\infty} a_k J_k(kr)e^{jk\phi} \tag{5.8}$$

- The total field in regions 1, 2, and 3 satisfies the continuity of the tangential electric/magnetic field on the interface in addition to zero tangential electric field on

the cylinder. Therefore, the sum also satisfies all the required boundary conditions, and hence the two problems are equivalent.

5.3 Neumann series solution

5.3.1 TM Case

The Fourier coefficients of the electric field on the circle r=a on either Riemann surface can be expanded in terms of Neumann series by

$$b_n H^1_{\left|\frac{n}{2}\right|}(ka) + \frac{1}{2} a_{n/2}' J_{|n/2|}(kr) = \sum_{p=0}^{\infty} (\chi_p^1 + \chi_p^2 e^{in\pi}) e^{-j\frac{n}{2}\phi_{sc}} \frac{J_{p+v}(\frac{n\phi_s}{2})}{(\frac{n\phi_s}{2})^v} \tag{5.9}$$

$$c_n J_{\left|\frac{n}{2}\right|}(k_2 a) = \sum_{p=0}^{\infty} \chi_p^1 \frac{J_{p+v}(\frac{n\phi_s}{2})}{(\frac{n\phi_s}{2})^v} e^{-j\frac{n}{2}\phi_{sc}} \tag{5.10}$$

$$d_n J_{\left|\frac{n}{2}\right|}(k_3 a) = \sum_{p=0}^{\infty} \chi_p^2 \frac{J_{p+v}(\frac{n\phi_s}{2})}{(\frac{n\phi_s}{2})^v} e^{in\pi} e^{-j\frac{n}{2}\phi_{sc}} \tag{5.11}$$

The above choice of Fourier coefficient satisfies the continuity of the tangential electric field across the boundary between regions 1 and 2, and regions 1 and 3. In the above equation, v=1 for the required edge condition. Expressing the fields u_1, u_2, and u_3 in terms of χ_p^1 and χ_p^2, we get:

$$u_1(r,\phi) = \sum_{n=-\infty}^{\infty} (1/2)a_{n/2}\left(J_{\left|\frac{n}{2}\right|}(kr) - \frac{J_{\left|\frac{n}{2}\right|}(ka)}{H^1_{\left|\frac{n}{2}\right|}(ka)} H^1_{\left|\frac{n}{2}\right|}(kr) \right) e^{jn\phi/2}$$
$$+ \sum_{n=-\infty}^{\infty} \frac{H^1_{\left|\frac{n}{2}\right|}(kr)}{H^1_{\left|\frac{n}{2}\right|}(ka)} \sum_{p=0}^{\infty} (\chi^1_p + \chi^2_p e^{in\pi}) e^{-j\frac{n}{2}\phi_{sc}} \frac{J_{v+p}(\frac{n\phi_s}{2})}{(\frac{n\phi_s}{2})^v} e^{jn\phi/2} \tag{5.12}$$

$$u_2(r,\phi) = \sum_{n=-\infty}^{\infty} \frac{J_{\left|\frac{n}{2}\right|}(k_1 r)}{J_{\left|\frac{n}{2}\right|}(k_1 a)} *$$
$$\sum_{p=0}^{\infty} \chi^1_p e^{-j\frac{n}{2}\phi_{sc}} \frac{J_{v+p}(\frac{n\phi_s}{2})}{(\frac{n\phi_s}{2})^v} \left(e^{\frac{jn\phi}{2}} - e^{-jn(\frac{\phi}{2}-\pi)} \right) \tag{5.13}$$

$$u_3(r,\phi) = \sum_{n=-\infty}^{\infty} \frac{J_{\left|\frac{n}{2}\right|}(k_1 r)}{J_{\left|\frac{n}{2}\right|}(k_1 a)} *$$
$$\sum_{p=0}^{\infty} \chi^2_p e^{-j\frac{n}{2}\phi_{sc}} \frac{J_{v+p}(\frac{n\phi_s}{2})}{(\frac{n\phi_s}{2})^v} \left(e^{in\pi} e^{\frac{jn\phi}{2}} - e^{-jn\frac{\phi}{2}} \right) \tag{5.14}$$

The magnetic field in each region is proportional to:

$$\frac{\partial u_1(r,\phi)}{\partial r} = \sum_{n=-\infty}^{\infty} (1/2) a_{n/2} \left(kJ_{\left|\frac{n}{2}\right|}'(kr) - \frac{J_{\left|\frac{n}{2}\right|}(ka)}{H^1_{\left|\frac{n}{2}\right|}(ka)} kH^1_{\left|\frac{n}{2}\right|}'(kr) \right) e^{jn\phi/2}$$

$$+ \sum_{n=-\infty}^{\infty} \frac{kH^1_{\left|\frac{n}{2}\right|}'(kr)}{H^1_{\left|\frac{n}{2}\right|}(ka)} \sum_{p=0}^{\infty} (\chi_p^1 + \chi_p^2 e^{in\pi}) e^{-j\frac{n}{2}\phi_{sc}} \frac{J_{v+p}(\frac{n\phi_s}{2})}{(\frac{n\phi_s}{2})^v} e^{jn\phi/2} \tag{5.15}$$

$$\frac{\partial u_2(r,\phi)}{\partial r} = \sum_{n=-\infty}^{\infty} \frac{k_1 J_{\left|\frac{n}{2}\right|}'(k_1 r)}{J_{\left|\frac{n}{2}\right|}(k_1 a)} \times$$

$$\sum_{p=0}^{\infty} e^{-j\frac{n}{2}\phi_{sc}} \chi_p^1 \frac{J_{v+p}(\frac{n\phi_s}{2})}{(\frac{n\phi_s}{2})^v} \left(e^{\frac{jn\phi}{2}} - e^{-jn(\frac{\phi}{2}-\pi)} \right) \tag{5.16}$$

$$\frac{\partial u_3(r,\phi)}{\partial r} = \sum_{n=-\infty}^{\infty} \frac{k_1 J_{\left|\frac{n}{2}\right|}'(k_1 r)}{J_{\left|\frac{n}{2}\right|}(k_1 a)} \times$$

$$\sum_{p=0}^{\infty} e^{-j\frac{n}{2}\phi_{sc}} \chi_p^2 \frac{J_{v+p}(\frac{n\phi_s}{2})}{(\frac{n\phi_s}{2})^v} \left(e^{in\pi} e^{\frac{jn\phi}{2}} - e^{-jn\frac{\phi}{2}} \right) \tag{5.17}$$

Multiplying Eqs. (5.15) and (5.16) with $[1-\{(\phi-\phi_{sc})/\phi_s\}^2]^{v-1/2} C_m^v(\{(\phi-\phi_{sc})/\phi_s\})$ and integrating w.r.t ϕ from $(\phi_{sc}-\phi_s)$ to $(\phi_s+\phi_{sc})$ and equating results:

$$\sum_{n=-\infty}^{\infty}(1/2)a_{n/2}\left(kJ_{\left|\frac{n}{2}\right|}'(kr)-\frac{J_{\left|\frac{n}{2}\right|}(ka)}{H^1_{\left|\frac{n}{2}\right|}(ka)}kH^1_{\left|\frac{n}{2}\right|}'(kr)\right)\frac{J_{v+m}(\frac{n\phi_s}{2})}{(\frac{n\phi_s}{2})^v}$$

$$+\sum_{n=-\infty}^{\infty}\frac{kH^1_{\left|\frac{n}{2}\right|}'(ka)}{H^1_{\left|\frac{n}{2}\right|}(ka)}\sum_{p=0}^{\infty}(\chi_p^1+\chi_p^2e^{in\pi})\frac{J_{v+p}(\frac{n\phi_s}{2})}{(\frac{n\phi_s}{2})^v}\frac{J_{v+m}(\frac{n\phi_s}{2})}{(\frac{n\phi_s}{2})^v} \tag{5.18}$$

$$=\sum_{n=-\infty}^{\infty}\frac{k_1J_{\left|\frac{n}{2}\right|}'(k_1a)}{J_{\left|\frac{n}{2}\right|}(k_1a)}\sum_{p=0}^{\infty}\chi_p^1\frac{J_{v+p}(\frac{n\phi_s}{2})J_{v+m}(\frac{n\phi_s}{2})}{(\frac{n\phi_s}{2})^{2v}}\left(1-(-1)^me^{jn(\pi-\phi_{sc})}\right)$$

Similarly, multiplying Eqs. (5.15) and (5.17) with $[1-\{[\phi-2\pi-\phi_{sc}]/\phi_s\}^2]^{v-1/2}C_m^v(\{[\phi-2\pi-\phi_{sc}]/\phi_s\})$, integrating w.r.t ϕ from $2\pi-\phi_{sc}-\phi_s$ to $2\pi-\phi_{sc}+\phi_s$, and equating gives:

$$\sum_{n=-\infty}^{\infty}(1/2)a_{n/2}\left(kJ_{\left|\frac{n}{2}\right|}'(kr)-\frac{J_{\left|\frac{n}{2}\right|}(ka)}{H^1_{\left|\frac{n}{2}\right|}(ka)}kH^1_{\left|\frac{n}{2}\right|}'(kr)\right)e^{in\pi}\frac{J_{v+m}(\frac{n\phi_s}{2})}{(\frac{n\phi_s}{2})^v}$$

$$+\sum_{n=-\infty}^{\infty}\frac{kH^1_{\left|\frac{n}{2}\right|}'(ka)}{H^1_{\left|\frac{n}{2}\right|}(ka)}\sum_{p=0}^{\infty}(e^{in\pi}\chi_p^1+\chi_p^2)\frac{J_{v+p}(\frac{n\phi_s}{2})}{(\frac{n\phi_s}{2})^v}\frac{J_{v+m}(\frac{n\phi_s}{2})}{(\frac{n\phi_s}{2})^v}= \tag{5.19}$$

$$\sum_{n=-\infty}^{\infty}\frac{k_1J_{\left|\frac{n}{2}\right|}'(k_1a)}{J_{\left|\frac{n}{2}\right|}(k_1a)}\sum_{p=0}^{\infty}\chi_p^2\frac{J_{v+p}(\frac{n\phi_s}{2})J_{v+m}(\frac{n\phi_s}{2})}{(\frac{n\phi_s}{2})^{2v}}\left(1-(-1)^me^{jn(\pi-\phi_{sc})}\right)$$

The linear system Eq.(5.18) and (5.19) can be solved for unknowns χ_p^1 and χ_p^2, respectively, and therefore, the field solution everywhere is obtained.

5.3.2 TE case

The Fourier coefficients of the electric field on the circle *r=a* on either Riemann surface can be expanded in terms of Neumann series as:

$$b_n kH^1_{\left|\frac{n}{2}\right|}{}'(ka) + 0.5 * a_{n/2}\, kJ_{\left|n/2\right|}{}'(kr) = \sum_{p=0}^{\infty} (\chi_p^1 + \chi_p^2 e^{in\pi}) e^{-j\frac{n}{2}\phi_{sc}} \frac{J_{p+v}(\frac{n\phi_s}{2})}{(\frac{n\phi_s}{2})^v} \tag{5.20}$$

$$c_n \frac{k_1}{\varepsilon_{r1}} J_{\left|\frac{n}{2}\right|}{}'(k_1 a) = \sum_{p=0}^{\infty} \chi_p^1 e^{-j\frac{n}{2}\phi_{sc}} \frac{J_{p+v}(\frac{n\phi_s}{2})}{(\frac{n\phi_s}{2})^v} \tag{5.21}$$

$$d_n \frac{k_1}{\varepsilon_{r1}} J_{\left|\frac{n}{2}\right|}{}'(k_1 a) = \sum_{p=0}^{\infty} \chi_p^2 e^{-j\frac{n}{2}\phi_{sc}} \frac{J_{p+v}(\frac{n\phi_s}{2})}{(\frac{n\phi_s}{2})^v} e^{in\pi} \tag{5.22}$$

The above choice of Fourier coefficients satisfies the continuity of tangential electric field on the boundary *r=a*. Expressing the fields u_1, u_2, and u_3 in terms of χ_p^1 and χ_p^2, we get:

$$\begin{aligned} u_1(r,\phi) = \sum_{n=-\infty}^{\infty} (1/2) a_{n/2} & \left(J_{\left|\frac{n}{2}\right|}(kr) - \frac{kJ_{\left|\frac{n}{2}\right|}{}'(ka)}{kH^1_{\left|\frac{n}{2}\right|}{}'(ka)} H^1_{\left|\frac{n}{2}\right|}(kr) \right) e^{jn\phi/2} \\ + \sum_{n=-\infty}^{\infty} & \frac{H^1_{\left|\frac{n}{2}\right|}(kr)}{kH^1_{\left|\frac{n}{2}\right|}{}'(ka)} \sum_{p=0}^{\infty} (\chi_p^1 + \chi_p^2 e^{in\pi}) e^{-j\frac{n}{2}\phi_{sc}} \frac{J_{v+p}(\frac{n\phi_s}{2})}{(\frac{n\phi_s}{2})^v} e^{jn\phi/2} \end{aligned} \tag{5.23}$$

$$u_2(r,\phi) = \sum_{n=-\infty}^{\infty} \frac{\varepsilon_{r1} J_{\left|\frac{n}{2}\right|}(k_1 r)}{k_1 J'_{\left|\frac{n}{2}\right|}(k_1 a)}$$
$$\times \sum_{p=0}^{\infty} \chi_p^1 e^{-j\frac{n}{2}\phi_{sc}} \frac{J_{v+p}(\frac{n\phi_s}{2})}{(\frac{n\phi_s}{2})^v} \left(e^{\frac{jn\phi}{2}} + e^{-jn(\frac{\phi}{2}-\pi)} \right) \tag{5.24}$$

$$u_3(r,\phi) = \sum_{n=-\infty}^{\infty} \frac{\varepsilon_{r1} J_{\left|\frac{n}{2}\right|}(k_1 r)}{k_1 J_{\left|\frac{n}{2}\right|}(k_1 a)}$$
$$\times \sum_{p=0}^{\infty} \chi_p^2 e^{-j\frac{n}{2}\phi_{sc}} \frac{J_{v+p}(\frac{n\phi_s}{2})}{(\frac{n\phi_s}{2})^v} \left(e^{in\pi} e^{\frac{jn\phi}{2}} + e^{-jn\frac{\phi}{2}} \right) \tag{5.25}$$

Multiplying Eqs. (5.23) and (5.24) with $[1-\{(\phi-\phi_{sc})/\phi_s\}^2]^{v-1/2} C_m^v(\{(\phi-\phi_{sc})/\phi_s\})$, integrating w.r.t ϕ from $(\phi_{sc}-\phi_s)$ to $(\phi_s+\phi_{sc})$, and equating gives

$$\sum_{n=-\infty}^{\infty} (1/2) a_{n/2} \left(J_{\left|\frac{n}{2}\right|}(kr) - \frac{kJ'_{\left|\frac{n}{2}\right|}(ka)}{kH^1_{\left|\frac{n}{2}\right|}'(ka)} H^1_{\left|\frac{n}{2}\right|}(kr) \right) \frac{J_{v+m}(\frac{n\phi_s}{2})}{(\frac{n\phi_s}{2})^v}$$
$$+ \sum_{n=-\infty}^{\infty} \frac{H^1_{\left|\frac{n}{2}\right|}(ka)}{kH^1_{\left|\frac{n}{2}\right|}'(ka)} \sum_{p=0}^{\infty} (\chi_p^1 + \chi_p^2 e^{in\pi}) \frac{J_{v+p}(\frac{n\phi_s}{2})}{(\frac{n\phi_s}{2})^v} \frac{J_{v+m}(\frac{n\phi_s}{2})}{(\frac{n\phi_s}{2})^v} = \tag{5.26}$$
$$\sum_{n=-\infty}^{\infty} \frac{\varepsilon_{r1} J_{\left|\frac{n}{2}\right|}(k_1 a)}{k_1 J'_{\left|\frac{n}{2}\right|}(k_1 a)} \sum_{p=0}^{\infty} \chi_p^1 \frac{J_{v+p}(\frac{n\phi_s}{2}) J_{v+m}(\frac{n\phi_s}{2})}{(\frac{n\phi_s}{2})^{2v}} \left(1 + (-1)^m e^{jn(\pi-\phi_{sc})} \right)$$

Multiplying Eqs. (5.23) and (5.25) with $[1-\{[\phi-2\pi-\phi_{sc}]/\phi_s\}^2]^{v-1/2}C_m^v(\{[\phi-2\pi-\phi_{sc}]/\phi_s\})$, integrating w.r.t ϕ from $2\pi-\phi_{sc}-\phi_s$ to $2\pi-\phi_{sc}+\phi_s$, and equating gives

$$\sum_{n=-\infty}^{\infty}(1/2)a_{n/2}e^{jn\pi}\left(J_{\left|\frac{n}{2}\right|}(kr)-\frac{kJ_{\left|\frac{n}{2}\right|}'(ka)}{kH^1_{\left|\frac{n}{2}\right|}'(ka)}H^1_{\left|\frac{n}{2}\right|}(kr)\right)\frac{J_{v+m}(\frac{n\phi_s}{2})}{(\frac{n\phi_s}{2})^v}$$

$$+\sum_{n=-\infty}^{\infty}\frac{H^1_{\left|\frac{n}{2}\right|}(ka)}{kH^1_{\left|\frac{n}{2}\right|}'(ka)}\sum_{p=0}^{\infty}(\chi_p^1e^{jn\pi}+\chi_p^2)\frac{J_{v+p}(\frac{n\phi_s}{2})}{(\frac{n\phi_s}{2})^v}\frac{J_{v+m}(\frac{n\phi_s}{2})}{(\frac{n\phi_s}{2})^v}=$$

$$\sum_{n=-\infty}^{\infty}\frac{\varepsilon_{r1}J_{\left|\frac{n}{2}\right|}(k_1a)}{k_1J_{\left|\frac{n}{2}\right|}'(k_1a)}\sum_{p=0}^{\infty}\chi_p^2\frac{J_{v+p}(\frac{n\phi_s}{2})}{(\frac{n\phi_s}{2})^v}\frac{J_{v+m}(\frac{n\phi_s}{2})}{(\frac{n\phi_s}{2})^v}\left(1+(-1)^me^{jn(\pi-\phi_{sc})}\right)$$

The linear system Eqs.(5.26) and (5.27) can be solved for unknowns χ_p^1 and χ_p^2, respectively, and therefore, the field solution everywhere is obtained.

5.3.3 Validation

The efficacy of the proposed method is demonstrated by comparing these results with the method defined in CHAPTER IV. For this purpose we compare the tangential electric field and magnetic field on the circle $r=a$ for ka=5 and ϕ_{inc}=0 obtained using the two methods. From Figure 5.3 and Figure 5.4, it is observed that the results compare well.

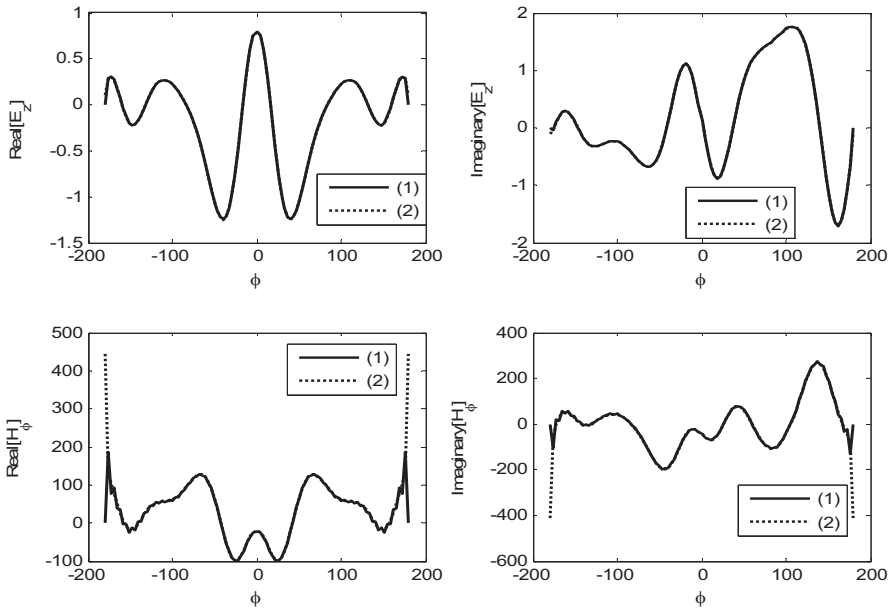

Figure 5.3. Tangential electric and magnetic field on the circle $r=a$ for $ka=5$, $\phi_{inc}=0$ and TM excitation using (1) the Riemann surface method (2) The original method of chapter IV

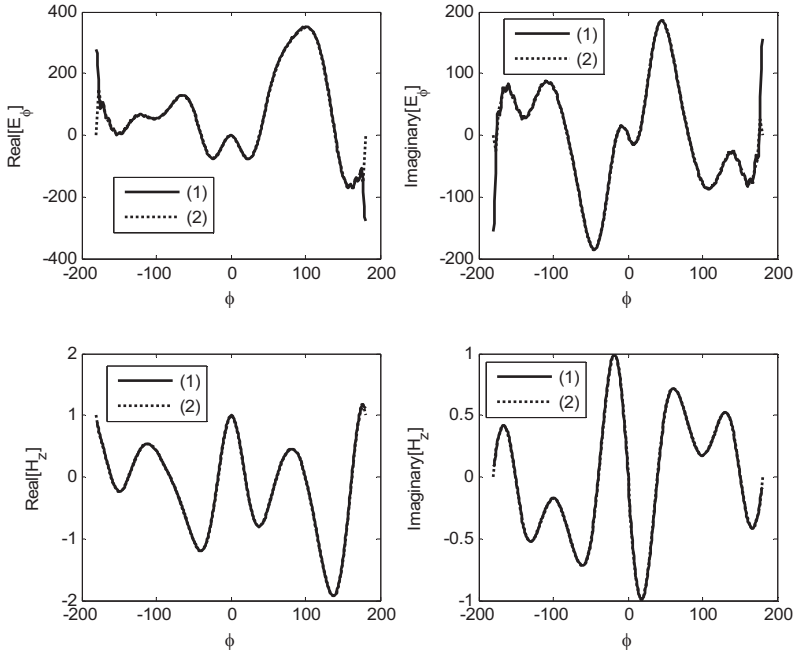

Figure 5.4. Tangential electric and magnetic field on the circle r=a for ka=5, $\phi_{inc}=0$ and TE excitation using. (1) The Riemann surface method (2) The original method of chapter IV.

5.4 Geometry of the wedge shaped cylinder

The geometry of the wedge-shaped metallic cylinder is shown in Figure 5.5. The wedge-shaped cylinder occupies the region r<a and $\phi \in [0,2\pi] \backslash (-\phi_s, \phi_s)$. For analysis purposes, the space surrounding the metallic cylinder is divided into two regions, region 1 (r>a) and region 2 (r<a and $\phi \in [-\phi_s, \phi_s]$). In this case, we are interested in when ϕ_s is given by $q\pi/(2h)$ where q and h are integers. The dielectric constant of region 2 is given by ε_{r2}, while free space is assumed for region 1. The structure is illuminated by a TM to z (electric field parallel to z-axis) or TE to z (magnetic field parallel to z-axis) plane wave incident at an angle of ϕ_{inc}. The time dependence assumed here is $\exp(-j\omega t)$. The fields in regions 1 and 2 are given by $u_1(r,\phi)$ and $u_2(r,\phi)$, where u_1 and u_2 represent the E_z /H_z component for TM and TE cases, respectively. The fields $u_1(r,\phi)$ and $u_2(r,\phi)$ are expressed in cylindrical harmonics as

$$u_1(r,\phi) = \sum_{n=-\infty}^{\infty} a_n J_n(kr) e^{jn\phi} + b_n H_n^1(kr) e^{jn\phi} \tag{5.28}$$

$$u_2(r,\phi) = \sum_{n=-\infty}^{\infty} c_n J_{\left|\frac{hn}{q}\right|}(k_1 r) \left(e^{j\frac{hn}{q}\phi} \mp e^{-j\frac{hn}{q}(\phi - \frac{q}{h}\pi)} \right) \tag{5.29}$$

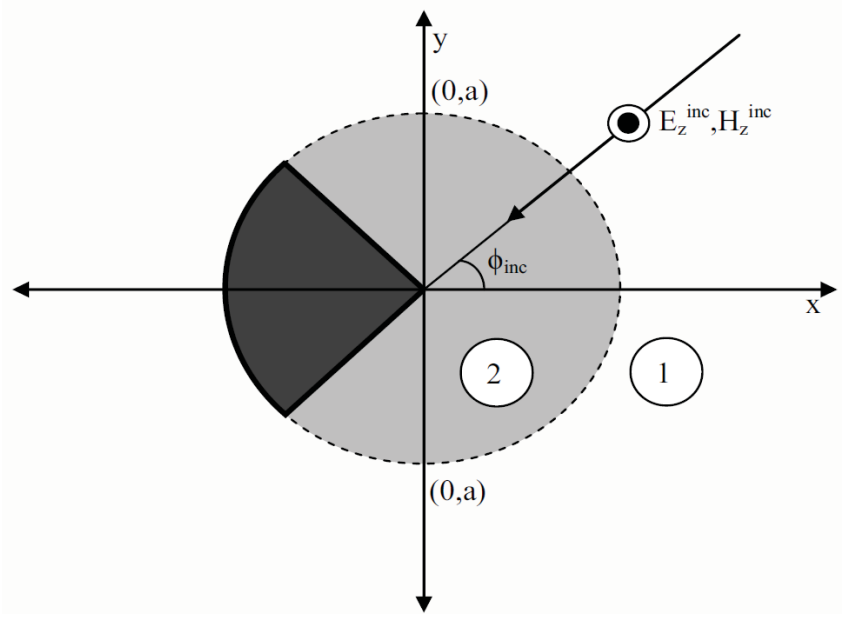

Figure 5.5. Geometry of the wedge-shaped cylinder

where $J_n(kr)$ and $H_n^1(kr)$ are Bessel and Hankel functions of the first kind. k and k_1 are the wave numbers of regions 1 and 2. In Eq. (5.29), the plus and minus sign are for the TE and TM cases, respectively. The coefficient a_n depends on the excitation and is given by

$$a_n = \begin{cases} e^{-jn\phi'} H_n^1(kr') & \text{Line source} \\ j^{-n} e^{-jn\phi_{inc}} & \text{Plane Wave} \end{cases} \tag{5.30}$$

The field $u_2(r,\phi)$ given by Eq. (5.29) satisfies the requirement of zero tangential electric field on the planar side of the metallic wedge-shaped cylinder.

5.5 Neumann series solution for the wedge shaped cylinder

5.5.1 TM case

The Fourier coefficients of the electric field on the circle $r=a$ is expanded in terms of Neumann series as:

$$b_n H_n^1(ka) + a_n J_n(ka) = \sum_{p=0}^{\infty} \chi_p^1 \frac{J_{p+v}(\frac{n\pi q}{2h})}{(\frac{n\pi q}{2h})^v} \tag{5.31}$$

$$c_n J_{\left|\frac{hn}{q}\right|}(k_1 a) = \frac{h}{q} \sum_{p=0}^{\infty} \chi_p^1 \frac{J_{p+v}(\frac{n\pi}{2})}{(\frac{n\pi}{2})^v} \tag{5.32}$$

The above choice of Fourier coefficient satisfies the continuity of the tangential electric field across the boundary between regions 1 and 2 along with the tangential electric field on the outer part of the PEC cylinder. In the above equation, v=7/6 and v=1 for the required edge condition for wedge angles of 90 and 0 degrees, respectively. Expressing the fields u_1 and u_2 in terms of χ_p^1, we get

$$\begin{aligned} u_1(r,\phi) = & \sum_{n=-\infty}^{\infty} a_n \left(J_n(kr) - \frac{J_n(ka)}{H_n^1(ka)} H_n^1(kr) \right) e^{jn\phi} \\ & + \sum_{n=-\infty}^{\infty} \frac{H_n^1(kr)}{H_n^1(ka)} \sum_{p=0}^{\infty} \chi_p^1 \frac{J_{v+p}(\frac{n\pi q}{2h})}{(\frac{n\pi q}{2h})^v} e^{jn\phi} \end{aligned} \tag{5.33}$$

$$u_2(r,\phi)=\frac{h}{q}\sum_{n=-\infty}^{\infty}\frac{J_{\left|\frac{hn}{q}\right|}(k_1 r)}{J_{\left|\frac{hn}{q}\right|}(k_1 a)}\sum_{p=0}^{\infty}\chi_p^1 e\frac{J_{v+p}(\frac{n\pi}{2})}{(\frac{n\pi}{2})^v}$$
$$\times\left(e^{\frac{jnh\phi}{q}}-e^{-j\frac{nh}{q}(\phi-\pi\frac{q}{h})}\right) \tag{5.34}$$

The tangential magnetic on the circle $r=a$ can be written as

$$\frac{\partial u_1(r,\phi)}{\partial r}=\sum_{n=-\infty}^{\infty}a_n\left(kJ_n'(ka)-\frac{J_n(ka)}{H_n^1(ka)}kH_n^{1\prime}(ka)\right)e^{jn\phi}$$
$$+\sum_{n=-\infty}^{\infty}\frac{kH_n^{1\prime}(ka)}{H_n^1(ka)}\sum_{p=0}^{\infty}\chi_p^1\frac{J_{v+p}(\frac{n\pi q}{2h})}{(\frac{n\pi q}{2h})^v}e^{jn\phi} \tag{5.35}$$

$$\frac{\partial u_2(r,\phi)}{\partial r}=\frac{h}{q}\sum_{n=-\infty}^{\infty}\frac{k_1 J_{\left|\frac{hn}{q}\right|}'(k_1 a)}{J_{\left|\frac{hn}{q}\right|}(k_1 a)}\times$$
$$\sum_{p=0}^{\infty}\chi_p^1 e\frac{J_{v+p}(\frac{n\pi}{2})}{(\frac{n\pi}{2})^v}\left(e^{\frac{jnh\phi}{q}}-e^{-j\frac{nh}{q}(\phi-\pi\frac{q}{h})}\right) \tag{5.36}$$

Multiplying Eqs. (5.35) and (5.36) by $[1-\{2h\phi/\pi q\}^2]^{v-1/2}C_m^v(\{2h\phi/\pi q\})$, integrating w.r.t ϕ from $-\pi q/2h$ to $-\pi q/2h$, and then equating gives

$$\frac{h}{q}\sum_{n=-\infty}^{\infty}\frac{k_1 J_{\left|\frac{hn}{q}\right|}'(k_1 a)}{J_{\left|\frac{hn}{q}\right|}(k_1 a)}\sum_{p=0}^{\infty}\chi_p^1 e\frac{J_{v+p}(\frac{n\pi}{2})J_{m+p}(\frac{n\pi}{2})}{(\frac{n\pi}{2})^{2v}}\left(1-(-1)^m e^{-jn\pi}\right)=$$

$$\sum_{n=-\infty}^{\infty}a_n\left(kJ_n'(ka)-\frac{J_n(ka)}{H_n^1(ka)}kH_n^1'(ka)\right)\frac{J_{v+m}(\frac{n\pi q}{2h})}{(\frac{n\pi q}{2h})^v} \tag{5.37}$$

$$+\sum_{n=-\infty}^{\infty}\frac{kH_n^1'(ka)}{H_n^1(ka)}\sum_{p=0}^{\infty}\chi_p^1\frac{J_{v+p}(\frac{n\pi q}{2h})}{(\frac{n\pi q}{2h})^v}\frac{J_{v+m}(\frac{n\pi q}{2h})}{(\frac{n\pi q}{2h})^v}$$

Solving the linear system in Eq.(5.37) for the unknown coefficients yields the scattered fields.

5.5.2 TE case

The Fourier coefficients of the electric field on the circle $r=a$ can be expanded in terms of Neumann series as:

$$b_n kH_n^1'(ka)+a_n kJ_n'(ka)=\sum_{p=0}^{\infty}\chi_p\frac{J_{p+v}(\frac{n\pi q}{2h})}{(\frac{n\pi q}{2h})^v} \tag{5.38}$$

$$c_n k_1 J_{\left|\frac{hn}{q}\right|}'(k_1 a)=\frac{h}{q}\sum_{p=0}^{\infty}\chi_p^1\frac{J_{p+v}(\frac{n\pi}{2})}{(\frac{n\pi}{2})^v} \tag{5.39}$$

The above choice of Fourier coefficient satisfies the continuity of the tangential electric field across the boundary between regions 1 and 2 along with the tangential electric field on the outer part of the PEC cylinder. In the above equation, v=1/6 and v=0 for the

required edge condition for wedge angles of 90 and 0 degrees, respectively. Expressing the fields u_1 and u_2 in terms of χ_p, we get

$$u_1(r,\phi) = \sum_{n=-\infty}^{\infty} a_n \left(J_n(kr) - \frac{kJ_n'(ka)}{kH_n^1'(ka)} H_n^1(kr) \right) e^{jn\phi} + \sum_{n=-\infty}^{\infty} \frac{H_n^1(kr)}{kH_n^1'(ka)} \sum_{p=0}^{\infty} \chi_p^1 \frac{J_{v+p}(\frac{n\pi q}{2h})}{(\frac{n\pi q}{2h})^v} e^{jn\phi} \tag{5.40}$$

$$u_2(r,\phi) = \frac{h}{q} \sum_{n=-\infty}^{\infty} \frac{J_{\left|\frac{hn}{q}\right|}(k_1 r)}{k_1 J_{\left|\frac{hn}{q}\right|}'(k_1 a)} \sum_{p=0}^{\infty} \chi_p \frac{J_{v+p}(\frac{n\pi}{2})}{(\frac{n\pi}{2})^v} \times \left(e^{\frac{jnh\phi}{q}} - e^{-j\frac{nh}{q}(\phi - \pi\frac{q}{h})} \right) \tag{5.41}$$

Multiplying Eqs. (5.40) and (5.41) by $[1-\{2h\phi/\pi q\}^2]^{v-1/2} C_m^v(\{2h\phi/\pi q\})$, integrating w.r.t ϕ from $-\pi q/2h$ to $-\pi q/2h$, and then equating gives

$$\frac{h}{q} \sum_{n=-\infty}^{\infty} \frac{J_{\left|\frac{hn}{q}\right|}(k_1 a)}{k_1 J_{\left|\frac{hn}{q}\right|}'(k_1 a)} \sum_{p=0}^{\infty} \chi_p \frac{J_{v+p}(\frac{n\pi}{2}) J_{m+p}(\frac{n\pi}{2})}{(\frac{n\pi}{2})^{2v}} \left(1 + (-1)^m e^{-jn\pi}\right) =$$

$$\sum_{n=-\infty}^{\infty} a_n \left(J_n(ka) - \frac{kJ_n'(ka)}{kH_n^1'(ka)} H_n^1(ka) \right) \frac{J_{v+m}(\frac{n\pi q}{2h})}{(\frac{n\pi q}{2h})^v} + \sum_{n=-\infty}^{\infty} \frac{H_n^1(ka)}{kH_n^1'(ka)} \sum_{p=0}^{\infty} \chi_p^1 \frac{J_{v+p}(\frac{n\pi q}{2h})}{(\frac{n\pi q}{2h})^v} \frac{J_{v+m}(\frac{n\pi q}{2h})}{(\frac{n\pi q}{2h})^v} \tag{5.42}$$

Solving the linear system in Eq.(5.42) for the unknown coefficients yields the scattered fields.

5.5.3 Numerical results

The proposed method can be validated by comparing the results with the solution available in literature. In Figure 5.6, the Normalized electric far field for a semicircular cylinder excited with line source is compared with [41]. The scattered electric far field for a thin strip illuminated with TM wave is compared with [40]. It is observed the results compare well. The backscattered RCS for TM and TE case for different wedge width is presented in Figure 5.7 and Figure 5.8. It is observed that, the RCS increase with increase in the wedge angle.

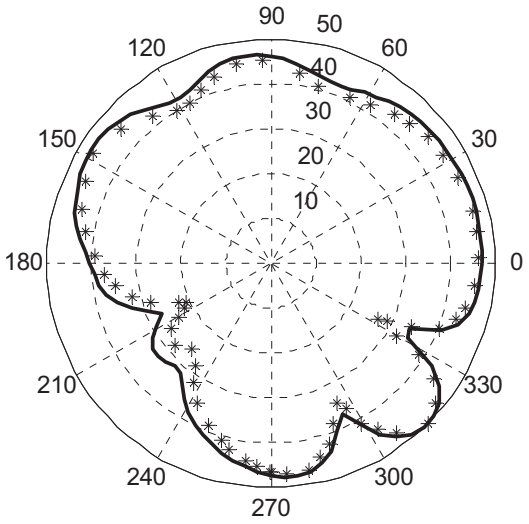

Figure 5.6. Normalized electric far field scattered by a semicircular cylinder ($a=0.8\lambda$) illuminated by an electric line source at $r_s=2a$ and $\phi_{inc}=\pi/4$.(1) Solid Line – Neumann series (2) Asterisks-Ref[41]

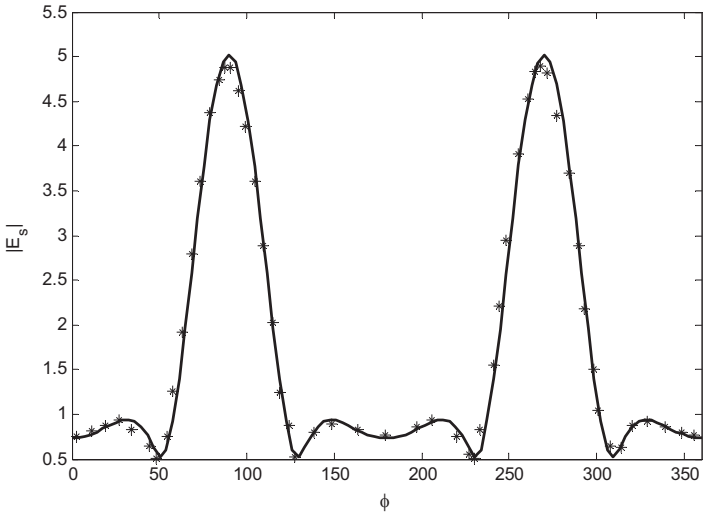

Figure 5.7. Comparison of electric far field scattered by a unloaded metallic strip ($ka=10$) illuminated by an TM incident at $\phi_{inc}=\pi/2$. (1) Solid line – Neumann series (2) Asterisks - Ref[40]

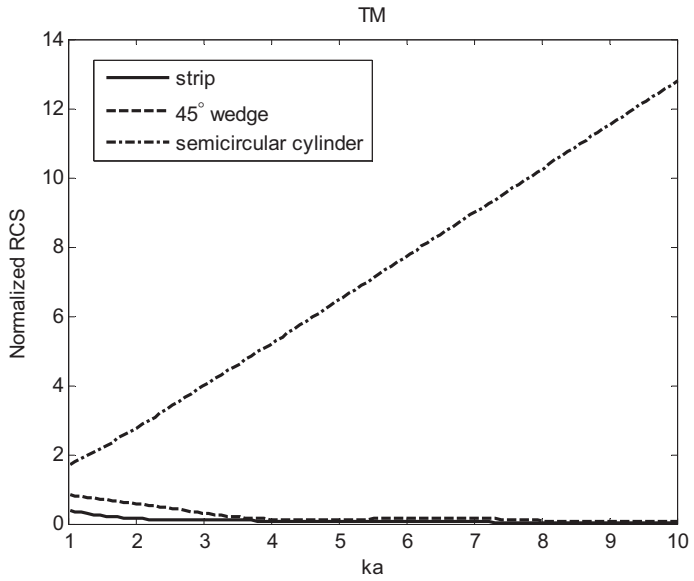

Figure 5.8 Comparison of normalized back scattered RCS for TM case for a thin strip, a 45° wedge cylinder, and a semicircular cylinder.

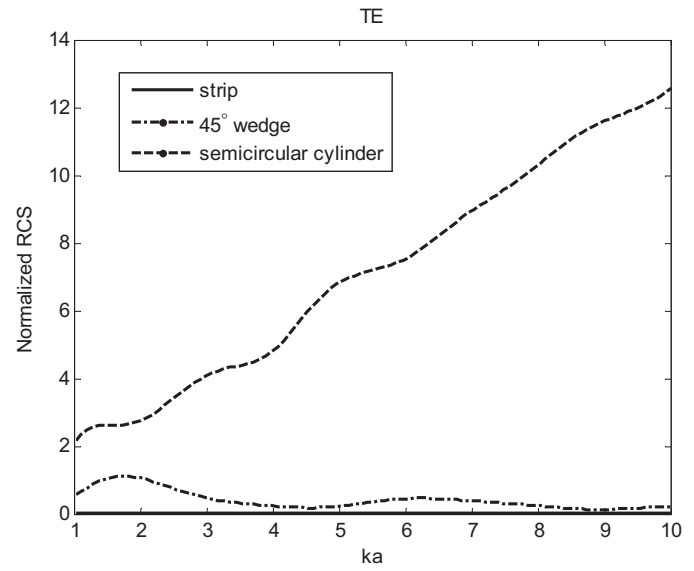

Figure 5.9. Comparison of normalized back scattered RCS for TM case for a thin strip, a 45° wedge cylinder, and a semicircular cylinder.

CHAPTER VI

SCATTERING FROM RESONANT CAVITIES ALONG A CIRCULAR ARC

6.1 Introduction

The study of superdirectivity has drawn significant attention in literature due to its application in high-gain antenna design. The use of passive elements like a finite array of slotted cylinders and rectangular grooves have been analyzed by Veremey [50][51] and Skigin [52]. In this work, we analyze the geometry of resonant cavities on a circular cylinder and circular arc for superdirective behavior. The analysis of scattering from a PEC circular cylinder with cavities using Neumann series is defined in section 6.2. Section 6.3 presents the analysis of scattering from cavities on a circular arc.

6.2 Diffraction from metallic circular cylinder with cavities

6.2.1. Geometry of the problem

The geometry of a circular metallic cylinder with N cavities illuminated by a plane wave is shown in Figure 6.1. The region occupied by each cavity is denoted as k ($b<r<a$ and $(1-2k)\phi_w<\phi<(3-2k)\phi_w$, $k=1..N$ and $\phi_w=\pi/N$). The cavities are coupled to the outer free space through a slit with angular width $2\phi_s$ which are centered symmetrically w.r.t to the axis of the cavity. The region $r>a$ is denoted as region '0'. The magnetic field

in each region is denoted by $u_0(r,\phi)$, $u_1(r,\phi)$, $u_2(r,\phi,,)..$, $u_N(r,\phi)$. The structure is illuminated by a TE to z (magnetic field parallel to z-axis) plane wave incident at an angle of ϕ_i. The time dependence assumed here is $\exp(-j\omega t)$. The fields u_0, u_1, $u_{2,..}$, u_N are expressed in cylindrical harmonics as follows:

$$u_0(r,\phi) = \sum_{n=-\infty}^{\infty}(a_n J_n(kr) + b_n H_n^1(kr))e^{jn\phi} \tag{6.1}$$

$$u_k(r,\phi) = \sum_{n=-\infty}^{\infty}\{c_n^k J_{\left|\frac{hn}{q}\right|}(kr) + d_n^k H^1_{\left|\frac{hn}{q}\right|}(kr)\} \times (e^{j\frac{hn}{q}(\phi+\phi'_k)} + e^{-j\frac{hn}{q}(\phi+\phi'_k-\frac{q}{h}\pi)}); k = 1..N. \tag{6.2}$$

where $J_n(kr)$ and $H_n^1(kr)$ are Bessel and Hankel functions of the first kind. $\phi_k' = 2\pi k/N$, $k=0,1..N-1$, and $\phi_w = \pi/N[q\pi/(2h)]$ where q and h are integers. b_n, c_n and d_n are the unknown coefficients to be determined, while a_n depends on the incident field given by

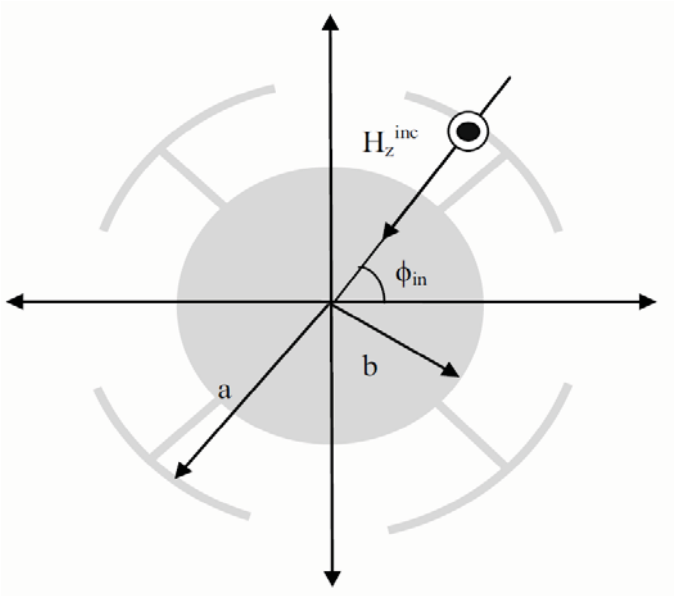

Figure 6.1. TE plane wave incident on a metallic circular cylinder with cavities.

$$a_n = \begin{cases} e^{-jn\phi'} H_n^1(kr') & \text{Line source} \\ j^{-n} e^{-jn\phi_{inc}} & \text{Plane Wave} \end{cases} \tag{6.3}$$

The above selection of u_k satisfies the requirement of zero tangential electric field on the flat walls of the cavities. Applying the condition of zero tangential electric field on the circle *r='b'* in each cavity gives

$$d_n^k = -c_n^k \frac{J_{\left|\frac{hn}{q}\right|}'(kb)}{H_{\left|\frac{hn}{q}\right|}^1{}'(kb)} \tag{6.4}$$

Hence the field u_k for k=1..N is written as

$$u_k(r,\phi) = \sum_{n=-\infty}^{\infty} c_n^k Z_n(kr) \times \left(e^{\frac{jhn}{q}(\phi+\phi'_k)} + e^{-\frac{jhn}{q}(\phi+\phi'_k-\frac{q}{h}\pi)}\right) \tag{6.5}$$

Where

$$Z_n(kr) = J_{\left|\frac{hn}{q}\right|}(kr) - \frac{J_{\left|\frac{hn}{q}\right|}'(kb)}{H_{\left|\frac{hn}{q}\right|}^1{}'(kb)} H_{\left|\frac{hn}{q}\right|}^1(kr). \tag{6.6}$$

6.2.2 Neumann series solution of the problem

In order to solve the problem, the Fourier coefficient of the electric field on the circle *r=a* is expressed in terms of Neumann series as:

$$c_n^k k Z_n'(ka) = \frac{h}{q} \sum_{p=0}^{\infty} \chi_p^k J_p\left(\frac{n\pi\phi_s}{2\phi_w}\right) \tag{6.7}$$

$$a_n kJ_n'(ka) + b_n kH_n^1'(ka) = \sum_{k=1}^{3}\sum_{p=0}^{\infty} \chi_p^k J_p(n\phi_s) e^{jn\phi_k'} \tag{6.8}$$

The details regarding the Neumann series selection follows that discussed in CHAPTER III and CHAPTER IV. The field in each region is written as

$$\begin{aligned} u_k(r,\phi) &= \frac{h}{q}\sum_{p=0}^{\infty}\chi_p^k \sum_{n=-\infty}^{\infty} c_n^k \frac{Z_n(kr)}{kZ_n'(ka)} J_p\left(\frac{n\pi\phi_s}{2\phi_w}\right) \\ &\times \left(e^{\frac{jhn}{q}(\phi+\phi'_k)} + e^{-\frac{jhn}{q}(\phi+\phi'_k-\frac{q}{h}\pi)}\right); k = 1,2,3. \end{aligned} \tag{6.9}$$

$$\begin{aligned} u_0(r,\phi) &= \sum_{n=-\infty}^{\infty} a_n \left(J_n(kr) - \frac{J_n'(ka)}{H_n^1'(ka)} H_n^1(kr)\right) e^{jn\phi} + \\ &\sum_{k=1}^{3}\sum_{p=0}^{\infty}\chi_p^k \sum_{n=-\infty}^{\infty} \frac{kH_n^1'(ka)}{H_n^1(ka)} J_p(n\phi_s) e^{jn\phi_k'} e^{jn\phi} \end{aligned} \tag{6.10}$$

The above selection of the Fourier coefficient in terms of Neumann series satisfies the continuity of the tangential electric field on the circle $r=a$. The only other boundary condition requirement is the continuity of the tangential magnetic field. Multiplying Eq. (6.9) and (6.10) with $[1-\{(\phi+\phi_l')/\phi_w\}^2]^{v-1/2} C_m^v(\{(\phi+\phi_l')/\phi_w\})$ and integrating w.r.t to 'ϕ' from $(2l-5)\phi_w$ to $(2l-3)\phi_w$ gives:

$$\begin{aligned} &\frac{h}{q}\sum_{p=0}^{\infty}\chi_p^l \sum_{n=-\infty}^{\infty} \frac{Z_n(ka)}{kZ_n'(ka)} J_p\left(\frac{n\pi\phi_s}{2\phi_w}\right) J_m\left(\frac{n\pi\phi_s}{2\phi_w}\right) \\ &\times (1 + e^{-in\pi}(-1)^m) = \\ &\sum_{n=-\infty}^{\infty} a_n \left(\frac{2i}{ka\pi}\right) J_m(n\phi_s) e^{-in\phi_l'} + \sum_{x=1}^{3}\sum_{p=0}^{\infty}\chi_p^x \\ &\times \sum_{n=-\infty}^{\infty} \frac{kH_n^1'(ka)}{H_n^1(ka)} J_p(n\phi_s) J_m(n\phi_s) e^{in(\phi_k'-\phi_l')}; l = 1,2,3 \end{aligned} \tag{6.11}$$

Solving the linear system Eq. (6.11) for the unknown coefficients yields the scattered fields.

6.2.3 Numerical Results

The accuracy of the Neumann series solution is examined by checking the continuity of the tangential magnetic field across the interface between region 0 and region k(k=1,2,..N). Figure 6.2 presents the tangential magnetic field for ka=5, N=4, b=0.5a, $\phi_s=\phi_w$ and ϕ_{inc}=0 using field expressions for region 0 and region k(k=1,2,..N). It is seen that the condition of continuity of the tangential magnetic field is satisfied, and the feasibility of the proposed method and numerical code is verified.

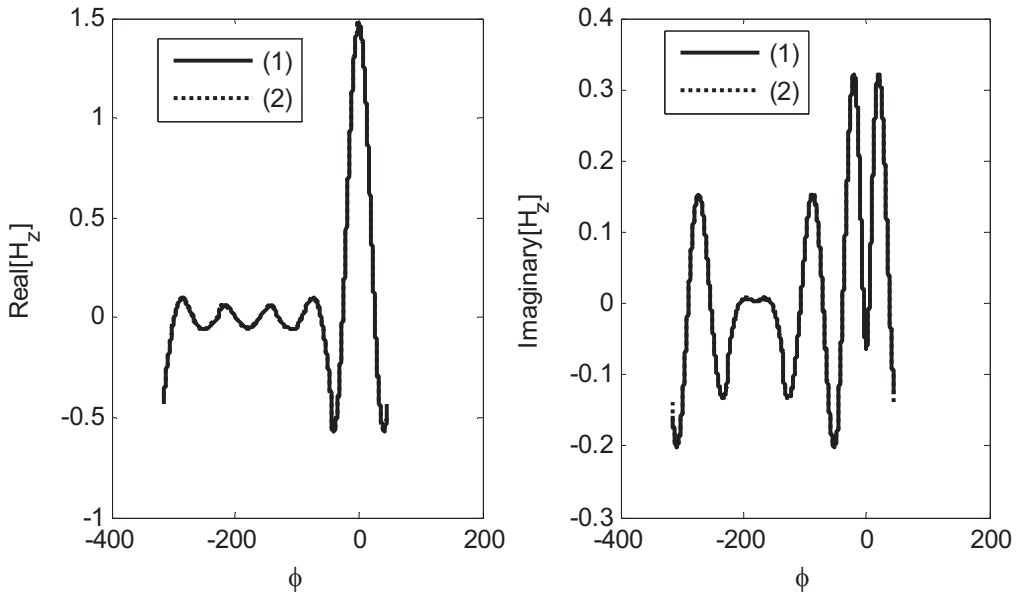

Figure 6.2. Tangential Magnetic field on the circle $r=a$ for N=4, b=0.5a, $\phi_s=\phi_w$ and ϕ_{inc}=0. (1) Using Eq. (6.1), (2) Using Eq.(6.2).

The directivity of a circular cylinder with 8 cavities (b=0.9a, ϕ_s =π/36) illuminated by a line source at r_s=1.2a, ϕ_{inc}=0 is shown in Figure 6.3. The maximum value of directivity is obtained at k_o=3.3. The size of the resonant cylinder needed to achieve high directivity is relatively large compared to earlier published results

[50][51][52]. The size of the structure needed to achieve the same directivity can be reduced since the resonant cavities not facing the source do not contribute to the directivity. Also, the cylinder portion of the structure does not contribute to the directivity. The analysis of the modified geometry is presented in the next section.

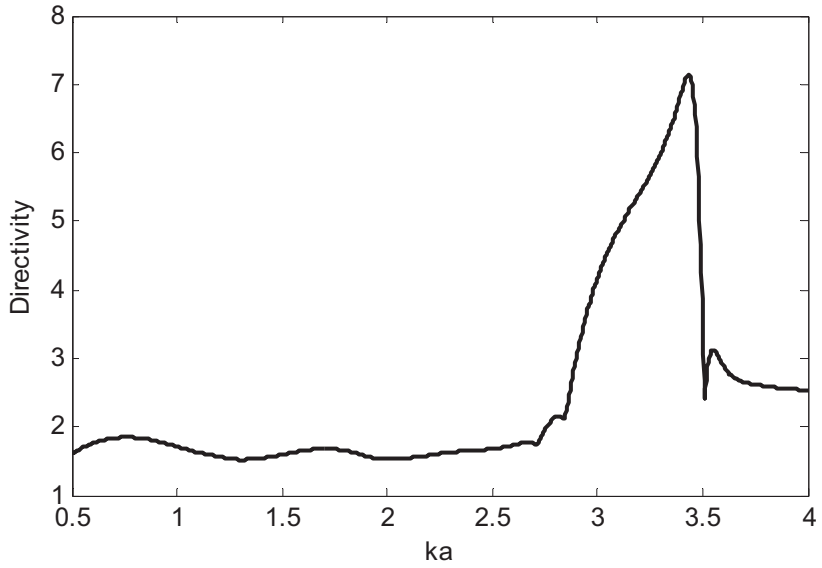

Figure 6.3. Directivity versus ka for a circular cylinder with 8 cavities(b=0.9a and $\phi_s=\pi/36$) illuminated by a line source excitation at $r_s=1.2a$, $\phi_{inc}=0$.

6.3 Scattering from cavities on a circular arc

6.3.1 Geometry of the problem

The geometry of a circular arc with N cavities illuminated by a line source is shown in Figure 6.4. The circular arc occupies the angular position $[0,2\pi]\backslash[-\phi_{w1},\phi_{w1}]$ where $\phi_{w1}=q\pi/(2h)$ and q, h are integers. The circular arc has N cavities, each of angular width $\phi_{w2}=(\pi/N)(2h-q)/2h$. The cavities are coupled to the outer region through a slit with

angular width $2\phi_s$ which are placed symmetrically w.r.t to the axis of the cavity. For analysis purposes, the entire space is divided into the following regions (1) Region $k(k=1..N)$ ($b<r<a$ and $-\phi_{w2}-\phi_k<\phi<\phi_{w2}-\phi_k$), where $-\phi_k$ is the axis of the cavity given by { $q\pi/(2h) + (\pi/N)(2h-q)(2k-1)/(2h)$}(2) Region $N+1$ (r<b) (3) Region $N+2$ ($b<r<a$ and $-\phi_{w1}<\phi<\phi_{w1}$) (4) Region $N+3(r>a)$.The line source excitation with position (r_s, ϕ_{inc}) is assumed to be in Region $N+1$. The time dependence assumed here is $\exp(-j\omega t)$. The field $u_k(k=1..N)$ is expressed in cylindrical harmonics as

$$u_k(r,\phi) = \sum_{n=-\infty}^{\infty} \{c_n^k J_{\left|\frac{Nhn}{2h-q}\right|}(kr) + d_n^k H^1_{\left|\frac{Nhn}{2h-q}\right|}(kr)\} \times$$
$$(e^{i\frac{Nhn}{2h-q}(\phi+\phi'_k)} + e^{-i\frac{Nhn}{2h-q}(\phi+\phi'_k-\frac{2h-q}{Nh}\pi)}); k=1..N. \tag{6.12}$$

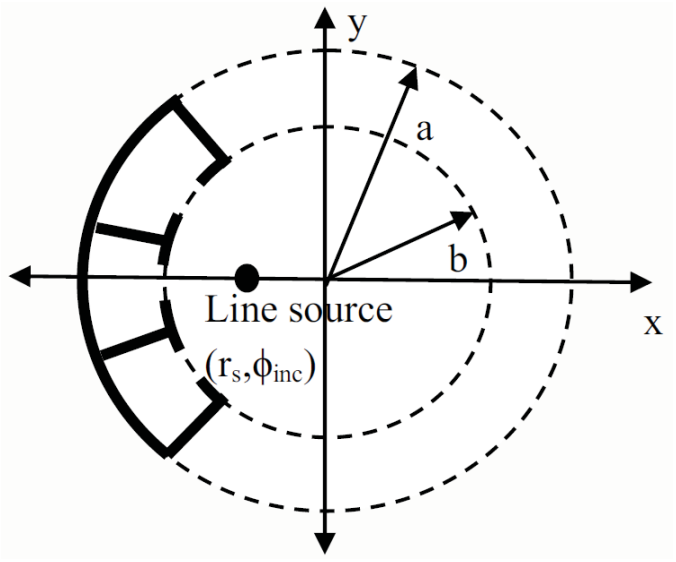

Figure 6.4. Circular arc with N cavities illuminated with line source

Each of the fields u_k has to satisfy the condition of zero tangential electric field on the circle $r=a$. This is achieved by the following relation between coefficients c_n^k and d_n^k :

$$d_n^k = -c_n^k \frac{J_{\left|\frac{Nhn}{2h-q}\right|}'(ka)}{H_{\left|\frac{Nhn}{2h-q}\right|}^1{}'(ka)} \tag{6.13}$$

Therefore, the field u_k is written as:

$$u_k(r,\phi) = \sum_{n=-\infty}^{\infty} c_n^k Z_n(kr) \times \left(e^{j\frac{Nhn}{2h-q}(\phi+\phi'_k)} + e^{-j\frac{Nhn}{2h-q}(\phi+\phi'_k-\frac{2h-q}{Nh}\pi)}\right); k = 1..N. \tag{6.14}$$

Where

$$Z_n(kr) = J_{\left|\frac{Nhn}{2h-q}\right|}(kr) - \frac{J_{\left|\frac{Nhn}{2h-q}\right|}'(kb)}{H_{\left|\frac{Nhn}{2h-q}\right|}^1{}'(kb)} H_{\left|\frac{Nhn}{2h-q}\right|}^1(kr) \tag{6.15}$$

The fields in regions N+1 to N+3 are given by

$$u_{N+1}(r,\phi) = \sum_{n=-\infty}^{\infty} \{e_n J_n(kr) + a_n H_n^1(kr)\} e^{jn\phi} \tag{6.16}$$

$$u_{N+2}(r,\phi) = \sum_{n=-\infty}^{\infty} \{c_n J_{\left|\frac{hn}{q}\right|}(kr) + d_n H_{\left|\frac{hn}{q}\right|}^1(kr)\} \times \left(e^{jn\frac{h}{q}\phi} + e^{-jn\frac{h}{q}(\phi-\frac{q}{h}\pi)}\right) \tag{6.17}$$

$$u_{N+3}(r,\phi) = \sum_{n=-\infty}^{\infty} b_n H_n^1(kr) e^{jn\phi} \tag{6.18}$$

Solving for the unknown coefficients b_n, c_n, d_n, e_n and c_n^k yields the scattered fields.

6.3.2 Neumann series solution of the problem

The Fourier coefficients of the electric field on the circle *r*='*a*' and *r*='*b*' are expanded in terms of Neumann series as

$$c_n^k kZ_n'(kb) = \frac{Nh}{2h-q} \sum_{p=0}^{\infty} \chi_p^k J_p(\frac{n\pi\phi_s}{2\phi_{w2}}) \tag{6.19}$$

$$\begin{aligned} &e_n kJ_n'(kb) + a_n kH_n^1{}'(kb) = \sum_{k=1}^{N} \sum_{p=0}^{\infty} \chi_p^k J_p(n\phi_s) e^{jn\phi_k'} \\ &+ \sum_{p=0}^{\infty} \chi_p^{N+1} J_p(n\phi_w) \end{aligned} \tag{6.20}$$

$$\begin{aligned} &c_n kJ_{\left|\frac{hn}{q}\right|}'(kb) + d_n kH_{\left|\frac{hn}{q}\right|}^1{}'(kb) \\ &= \frac{h}{q} \sum_{p=0}^{\infty} \chi_p^{N+1} J_p(\frac{n\pi}{2}) \end{aligned} \tag{6.21}$$

$$\begin{aligned} &c_n kJ_{\left|\frac{hn}{q}\right|}'(ka) + d_n kH_{\left|\frac{hn}{q}\right|}^1{}'(ka) \\ &= \frac{h}{q} \sum_{p=0}^{\infty} \chi_p^{N+2} J_p(\frac{n\pi}{2}) \end{aligned} \tag{6.22}$$

$$b_n kH_n^1{}'(ka) = \sum_{p=0}^{\infty} \chi_p^{N+2} J_p(n\phi_{w1}) \tag{6.23}$$

Expressing the magnetic field in each region in terms of unknown coefficients, yields

$$\begin{aligned} &u_k(r,\phi) = \sum_{n=-\infty}^{\infty} \{c_n^k J_{\left|\frac{Nhn}{2h-q}\right|}(kr) + d_n^k H_{\left|\frac{Nhn}{2h-q}\right|}^1(kr)\} * \\ &(e^{j\frac{Nhn}{2h-q}(\phi+\phi'_k)} + e^{-j\frac{Nhn}{2h-q}(\phi+\phi'_k-\frac{2h-q}{Nh}\pi)}); k = 1..N. \end{aligned} \tag{6.24}$$

$$u_{N+1}(r,\phi)=\sum_{n=-\infty}^{\infty}\frac{a_n}{kJ_n'(kb)}\{\frac{-2kj}{\pi ka}\}e^{jn\phi}+$$
$$\sum_{n=-\infty}^{\infty}\frac{J_n(kr)}{kJ_n'(kb)}e^{jn\phi}\sum_{k=1}^{N}\sum_{p=0}^{\infty}\chi_p^k J_p(n\phi_s)e^{jn\phi_k'} \tag{6.25}$$
$$+\sum_{n=-\infty}^{\infty}\frac{J_n(kr)}{kJ_n(kb)}e^{jn\phi}\sum_{p=0}^{\infty}\chi_p^{N+1}J_p(n\phi_{w1})$$

$$u_{N+2}(r,\phi)=\sum_{n=-\infty}^{\infty}\{\frac{Y_n(a,r)}{X_n}\sum_{p=0}^{\infty}\chi_p^{N+1}J_p(\frac{n\pi}{2})-$$
$$\frac{Y_n(b,r)}{X_n}\sum_{p=0}^{\infty}\chi_p^{N+2}J_p(\frac{n\pi}{2})\} \tag{6.26}$$
$$\times(e^{jn\frac{h}{q}\phi}+e^{-jn\frac{h}{q}(\phi-\frac{q}{h}\pi)})$$

$$u_{N+3}(r,\phi)=\sum_{n=-\infty}^{\infty}\frac{H_n^1(kr)}{kH_n^1{}'(kr)}e^{jn\phi}\sum_{p=0}^{\infty}\chi_p^{N+2}J_p(n\phi_{w1}) \tag{6.27}$$

where

$$X_n=k^2(H^1_{\left|\frac{hn}{q}\right|}{}'(kb)J_{\left|\frac{hn}{q}\right|}{}'(ka)-H^1_{\left|\frac{hn}{q}\right|}{}'(ka)J_{\left|\frac{hn}{q}\right|}{}'(kb)) \tag{6.28}$$

$$Y_n(x,r)=\frac{kh}{q}(H^1_{\left|\frac{hn}{q}\right|}(kr)J_{\left|\frac{hn}{q}\right|}{}'(kx)-H^1_{\left|\frac{hn}{q}\right|}{}'(kx)J_{\left|\frac{hn}{q}\right|}(kr)) \tag{6.29}$$

Once again, the selection of Neumann series as defined by Eq. (6.19), (6.20), (6.21), (6.22), and (6.23) satisfies the continuity of the tangential electric field across all interfaces. To achieve the continuity of tangential magnetic field, the following procedure is used. Multiplying Eq.(6.24) and (6.25) with $[1-\{(\phi+\phi_l)/\phi_s\}2]^{v-1/2}\ C_m{}^0\{(\phi+\phi_l)/\phi_s\}$, integrating w.r.t to ϕ from $-\phi_s+\phi_l$ to $-\phi_s+\phi_l$, and equating gives

$$\frac{Nh}{2h-q}\sum_{p=0}^{\infty}\chi_p^l\sum_{n=-\infty}^{\infty}\frac{Z_n(kb)}{kZ_n'(kb)}J_p(\frac{n\pi\phi_s}{2\phi_{w2}})J_m(\frac{n\pi\phi_s}{2\phi_{w2}})$$
$$\times(1+e^{-jn\pi}(-1)^m)=\sum_{n=-\infty}^{\infty}\frac{a_n}{kJ_n'(kb)}\{\frac{-2kj}{\pi ka}\}e^{-jn\phi_l'}$$
$$\times J_m(n\phi_s)+\sum_{n=-\infty}^{\infty}\frac{J_n(kb)}{kJ_n'(kb)}J_m(n\phi_s)\sum_{k=1}^{N}\sum_{p=0}^{\infty}\chi_p^k \tag{6.30}$$
$$\times J_p(n\phi_s)e^{jn(\phi_k'-\phi_l')}+\sum_{n=-\infty}^{\infty}\frac{J_n(kb)}{kJ_n(kb)}J_m(n\phi_s)e^{-jn\phi_l'}$$
$$\times\sum_{p=0}^{\infty}\chi_p^{N+1}J_p(n\phi_{w1})$$

Similarly, multiplying Eq. (6.25) and (6.26) by $[1-(\phi/\phi_{w1})^2]^{v-1/2}C_m^0(\phi/\phi_{w1})$, integrating w.r.t to ϕ from $-\phi_{w1}$ to ϕ_{w1}, and equating yields:

$$\sum_{n=-\infty}^{\infty}\frac{a_n}{kJ_n'(kb)}\{\frac{-2ki}{\pi ka}\}J_m(n\phi_{w1})+$$
$$\sum_{n=-\infty}^{\infty}\frac{J_n(kb)}{kJ_n'(kb)}J_m(n\phi_{w1})\sum_{k=1}^{N}\sum_{p=0}^{\infty}\chi_p^kJ_p(n\phi_s)e^{jn\phi_k'}$$
$$+\sum_{n=-\infty}^{\infty}\frac{J_n(kb)}{kJ_n(kb)}J_m(n\phi_{w1})\sum_{p=0}^{\infty}\chi_p^{N+1}J_p(n\phi_{w1}) \tag{6.31}$$
$$=\sum_{n=-\infty}^{\infty}\{\frac{Y_n(a,b)}{X_n}\sum_{p=0}^{\infty}\chi_p^{N+1}J_p(\frac{n\pi}{2})-$$
$$\frac{Y_n(b,b)}{X_n}\sum_{p=0}^{\infty}\chi_p^{N+2}J_p(\frac{n\pi}{2})\}*J_m(\frac{n\pi}{2})$$
$$\times(1+(-1)^me^{jn\pi})$$

Finally, multiplying Eq. (6.26) and (6.27) by $[1-(\phi/\phi_{w1})^2]^{v-1/2}C_m^0(\phi/\phi_{w1})$, integrating w.r.t to ϕ from $-\phi_{w1}$ to ϕ_{w1}, and equating yields

$$\sum_{n=-\infty}^{\infty} \frac{H_n^1(kr)}{kH_n^{1\prime}(kr)} J_m(n\phi_{w1}) \sum_{p=0}^{\infty} \chi_p^{N+2} J_p(n\phi_{w1})$$
$$= \sum_{n=-\infty}^{\infty} \{\frac{Y_n(a,a)}{X_n} \sum_{p=0}^{\infty} \chi_p^{N+1} J_p(\frac{n\pi}{2}) - \tag{6.32}$$
$$\frac{Y_n(b,a)}{X_n} \sum_{p=0}^{\infty} \chi_p^{N+2} J_p(\frac{n\pi}{2})\} * J_m(\frac{n\pi}{2})$$
$$\times (1+(-1)^m e^{jn\pi})$$

The linear system Eq. (6.30), (6.31), and (6.32) can be solved to obtain the solution.

6.3.3 Numerical results

The Neumann series solution is validated by comparing the magnetic field amplitude at (0,0) to the one obtained by EMP2LAB software. This comparison is shown in Figure 6.5 and the efficacy of the Neumann series is verified. The directivity for a semicircular arc with 7 cavities illuminated with line source is shown in Figure 6.6. It is observed that for similar values of directivity, the size of the semicircular arc with cavities is half the size of the circular cylinder with cavities.

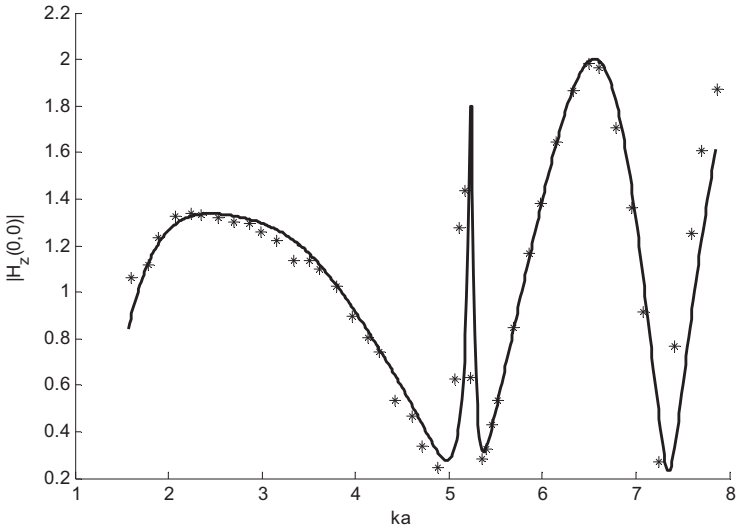

Figure 6.5. Comparison of magnitude of magnetic field (H_z) at (0,0) for a circular arc with plane wave incidence. (b=0.5a, h=2, q=3, $\phi_s=\pi/8$, and N=1) (1) Solid line – Neumann series (2) Asterisks - EMP2LAB.

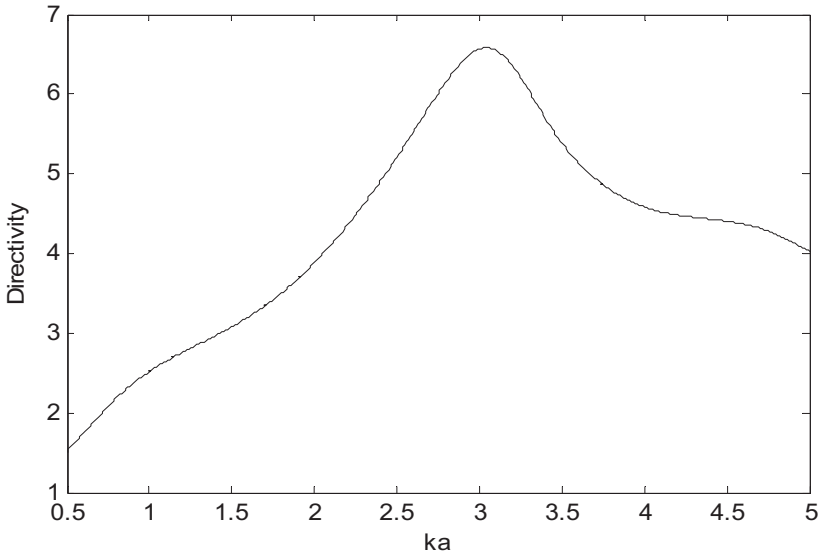

Figure 6.6. Directivity versus ka for a semicircular arc with 7 cavities. (b=0.9a, h=1, q=1, N=7, $r_s=0.5b$,$\phi_{inc}=\pi$ and $\phi_s=\pi/14$)

CHAPTER VII

CONCLUSIONS AND FUTURE WORK

7.1 Conclusions

The problem of plane wave scattering by a tandem slit loaded with a homogenous material has been solved via the Wiener-Hopf technique, where the waves are polarized parallel to the edges of the slit. The boundary value problem is formulated into a pair of simultaneous Wiener-Hopf equations, which are each reduced to a Fredholm integral equation of the second kind. The integral equations are then solved approximately to yield the Fourier transform of the diffracted fields. The inverse transform is evaluated asymptotically to yield the diffracted far field, which is dependent on the slit dimensions and material properties of the loading material. The results show that it is possible to reduce the beamwidth and increase power coupled through the tandem slit by changing the loaded tandem slit parameters such as dielectric constant, thickness, and width. The analytic solution concurs well with measured and simulated results. The above procedure is valid for '*l*' greater than or equal to $0.1\lambda_o$. Also, the method can be easily extended for the TE case.

Two methods for computing scattered fields from an eccentrically loaded cylinder with multiple slits are presented. The IE/NS technique is found to be accurate and efficient and is shown to exhibit much better convergence properties than the corresponding IE/CBC technique. Backscattered RCS results are examined for several different geometries. RCS variations with

respect to relative conductor size, conductor eccentricity, the number of slits, and cylinder loading are presented. The extension of Neumann series to scattering by a metallic strip and semicircular cylinder is presented. The method presented is numerically very efficient. The Neumann series method is applied for evaluating scattering from a circular cylinder with resonant cavities for analyzing the superdirective properties of the structure.

7.2 Future work

The applicability of Neumann series method for studying scattering from polygonal structures needs to be explored.

REFERENCES

[1] M. A. K. Hamid, S. C. Kashyap, A. Mohsen, W. M. Boerner and R. J. Boulanger," A Ray-Optical Approach to the Analysis of Microwave Filters," *European Microwave Conference* ,pp. 189-193, Oct-1969.

[2] S. C. Kashyap and M. A. K Hamid," Diffraction characteristics of a slit in a thick conducting screen," *IEEE Trans. Antennas and Propagat.,* vol. AP-19, no. 4, pp. 499-507, July 1971.

[3] S. C. Kashyap, M. A. K. Hamid, and N. J. Mostowy, "Diffraction patterns of a slit in a thick conducting screen," *J. Appl. Phys*., Feb. 1971.

[4] L. R. Alldredge, "Diffraction of microwaves by tandem slits,"*IRE Trans. Antennas Propagat*., vol. AP-4. Oct. 1956, pp.640-649.

[5] B. Polat, A. Buyukaksoy, and G. Cinar," Plane wave diffraction by tandem impedence slits," Progress in Electromagnetic Research, PIER-34, 29-61, 2001.

[6] Jean-Fu Kiang," Wave Penetration through Slits on Stacked Thick plates," *IEEE Trans. Microwave Theory Tech*. Vol. 46, No. 7, pp. 889-893,Jul-1998.

[7] D. T. Auckland and R. F. Harrington, "Electromagnetic transmission through a filled slit in a conducting plane of finite thickness, TE case," *IEEE Trans. Microwave Theory Tech*. MTT-26,499-505(1978).

[8] F.L. Neerhoff and G. Mur, "Diffraction of Plane Electromagnetic Waves by a Slit in a Thick Screen Placed between Two Different Media," *Appl. Sci. Res*. 28, pp. 78-88, 1973.

[9] J. M. Jin and J. L Volakis,"TE scattering by an inhomogeneous filled aperture in a thick conducting plane," *IEEE Trans. Antennas Propag*. 38,pp. 1280-1286 (1990).

[10] T.T. Fong," Radiation from the open ended waveguide with extended loading," *Radio Science,* vol 7, no 10, pp. 965-972, 1972.

[11] R. A. Hurd and B.K Sachdeva,"Scattering by a dielectric-loaded slit in a conducting plane,"*Radio Science*, vol 10, no 5, pp.565-572, 1975.

[12] B. Noble, *Methods Based on the Wiener-Hopf Technique*. NewYork: Pergamon, 1958.

[13] D. S. Jones,"Diffraction by waveguide of finite length,"*Proc Cambridge Phil . Soc.*,vol. 48, 1952,pp.118-134.

[14] EM Photonics, Inc [Online]. Available: http://www.emphotonics.com/products/fastfdtd. [Accessed: 17 February 2009].

[15] J.L. Volakis, A. Chatterjee and L. C. Kempel,"*Finite Element Method for Electromagnetics,*"IEEE Press-1998, pp. 127.

[16] J. B. Conway,"*Functions of One Complex Variable I*,"Springer-1978.

[17] R. Mittra and S. W. Lee, *Analytical Techniques in the theory of Guided waves*, The Macmillan Company, New-York-1971.

[18] İ.H. Tayyar and A. Büyükaksoy, "Plane wave diffraction by the junction of a thick impedance half-plane and a thick dielectric slab", *IEE Proc.-Sci. Meas. Technol.*, vol. 150, no. 4, pp. 169-176, 2003

[19] R. W. Ziolkowski and J. Grant, "Scattering from cavity-backed apertures: The generalized dual series solution of the concentrically loaded E-pol slit cylinder problem," *IEEE Trans. Antennas Propagat.,* Vol. AP-35, pp. 504-528, May 1987.

[20] L. B. Felsen and G. Vecchi, "Wave scattering from slit coupled cylindrical cavities with interior loading: Part II - Resonant mode expansion, "*IEEE Trans. Antennas Propagat.*, Vol. 39, No. 8, Aug 1991.

[21] E. Arvas, "Electromagnetic diffraction from a dielectric filled slit-cylinder enclosing a cylinder of arbitrary cross section: TM case," *IEEE Trans. Electromagn. Compat.*, Vol. 31, pp. 91-102, Feb. 1989.

[22] J.-W. Yu and N.-H. Myung, "Oblique scattering and coupling to a slit coaxial cable: TM case," *JEWA*, Vol. 14, pp. 931-942, 2000.

[23] J. R. Mautz and R. F. Harrington, "Electromganetic penetration into a conducting circular cylinder through a narrow slot, TE case," *JEWA*, Vol. 3, No. 4, pp. 307-336, 1989.

[24] J. R. Mautz and R. F. Harrington, "Electromganetic penetration into a conducting circular cylinder through a narrow slot, TM case," *JEWA*, Vol. 2, No. 3/4, pp. 269-293, 1988.

[25] J. D. Shumpert and C. M. Butler," Penetration through slots in conducting cylinders - Part 1: TE case," *IEEE Trans. Antennas Propag*., Vol. 46, No. 11, pp. 1612-1621, Nov. 1998.

[26] J. D. Shumpert and C. M. Butler," Penetration through slots in conducting cylinders - Part 1: TM case," *IEEE Trans. Antennas Propag.*, Vol. 46, No. 11, pp. 1621-1628, Nov. 1998.

[27] Colak, D., A. I. Nosich, and A. Altintas, "Radar cross-section study of cylindrical cavity-backed apertures with outer or inner material coating: The case of E-polarization," *IEEE Trans. Antennas Propag.*, Vol. AP-41, No. 11, pp. 1551-1559, Nov. 1993.

[28] Colak, D., A. I. Nosich, and A. Altintas, "Radar cross-section study of cylindrical cavity-backed apertures with outer or inner material coating: The case of H-polarization," *IEEE Trans. Antennas Propag.*, Vol. AP-43, No. 5, pp. 440-447, May 1995.

[29] F. Montiel and M. Neviere," Electromagnetic study of the diffraction of light by a mask used in photolithography," *Opt. Commun*, 101, pp. 151-156, 1993.

[30] B. Guizal and D. Felbacq, "Numerical computation of the scattering matrix of an electromagnetic resonator," *Phys. Rev. E,* 60, 026602 (2002).

[31] J. A. Stratton, Electromagnetic Theory. New York: McGraw Hill, 1941.

[32] V. V. Veremey and R. Mittra, "Scattering from structures formed by resonant elements," *IEEE Trans. Antennas Propag.*, Vol. AP-46, No. 4, pp. 494-501, April 1998.

[33] Y. A. Tucklin, "Wave Scattering by an open cylindrical screens of arbitrary profile with Dirichlet boundary value," *Soviet Phys. Doklady*, Vol. 30, pp. 1027-1030, April 1985.

[34] B. Guizal and D. Felbacq," Electromagnetic beam diffraction by a finite strip grating," *Opt Commun*, 165, pp. 1-6, 1999.

[35] F. Delfino, R. Procopio and M. Rossi, A new method for the solution of convolution-type dual integral-equation systems occurring in engineering electromagnetic, *J Eng Math,* 63, pp. 51-59, 2009.

[36] I. S. Gradshteyn and I. M. Ryzhik, "Table of Integrals, Series and products," 7th edition, 2007. Edited by A. Jeffrey and D. Zwillinger. Academic Press, New York.

[37] Scharstein R. W, M. L. Waller and T. H. Shumpert, "Near-field and plane-wave electromagnetic coupling into a slotted circular cylinder: Hard or TE polarization," *IEEE Trans. Electromagn. Compat.*, Vol. 48, No. 4, pp. 714-724, Nov. 2006.

[38] L. Glasser, ”A Class of Bessel Summations,” Mathematics of Computation, Vol 37, No. 156, p. 499, Oct. 1981.

[39] J. J. Bowman, T. B. A. Senior and P. L. E. Uslenghi, *Electromagnetic and Acoustic Scattering by Simple Shapes*, Newyork: Summa 1967.

[40] A. Z. Elsherbeni and M. Hamid,”Scattering by a perfectly conducting strip loaded with a dielectric cylinder(TM case),”*IEE Proceedings*, Vol. 136, No. 3, June 1989.

[41] S. Srikanth and P.H. Pathak,”Hybrid UTD-MM Analysis of the Scattering by a Perfectly Conducting Semicircular Cylinder,” *IEEE Trans. Antennas Propagat* .,Vol 34, No. 10, Oct 1986.

[42] R. A. Hurd and B. K. Sachdeva, ”Diffraction by a Composite Cylinder,” *J. Appl Phys*, Vol. 46, No. 4 April 1975.

[43] J. L. Tsalamengas, J. G. Fikioris and B. T. Babili,”Direct and efficient solution of integral equation for scattering from strips and slots,”*J. Appl. Phys*, Vol. 66, No. 1, Jul 1989.

[44] S Seran, J. P. Donohoe and E. Topsakal, “Scattering by an eccentrically loaded Cylindrical Cavity with multiple slits,” *submitted to IEEE Trans. Antennas Propagat* .

[45] R. Mittra and S. W. Lee, Analytical Techniques in the theory of Guided waves. New York:Macmillan, 1971.

[46] K. Barkeshli and J. L. Volakis,” Electromagnetic Scattering from thin strips-Part-II: Numerical Solution for strips of arbitrary size,” *IEEE Trans. Edu* .,Vol. 47, No. 1, Feb-2004.

[47] K. Barkeshli and J. L. Volakis,” Electromagnetic Scattering from thin strips – Part I: Numerical Solution for strips of arbitrary size,” IEEE Trans. Edu., Vol. 47, No. 1, pp 100-106, Feb-2004.

[48] F. Delfino, R. Procopio and M. Rossi, A new method for the solution of convolution-type dual integral-equation systems occurring in engineering electromagnetic, J Eng Math, 63, pp. 51-59, 2009.

[49] R.D. Graglia, G. Lombardi, "Singular higher order divergence-conforming bases of additive kind and Moments Method applications to 3D sharp-wedge structures," IEEE Trans. Antennas Propagat., vol. 56, n.12, pp. 3768-3788, 2008.

[50] V. V. Veremey and V. P. Shestopalov,”Superdirective radiation forming in antenna with passive resonant reflector,” *Radio Sci.*, vol 26, no 2, pp. 631-636, 1991.

[51] V. V. Veremey and R. Mittra ,"Scattering from Structures Formed by Resonant Elements," *IEEE Trans. Antennas Propagat* .,Vol 46, No. 4, April 1998.

[52] D. C. Skigin, V. V. Veremey and R. Mittra,"Superdirective Radiation from finite Gratings of Rectangular Grooves," *IEEE Trans. Antennas Propagat* .,Vol 47, No. 2, Feb 1999.

APPENDIX A

The factorized kernel is written as

$$L(\alpha) = L_1(\alpha)L_2(\alpha) \tag{A1}$$

where

$$L_1(\alpha) = \frac{\mu_r}{-j2K(\alpha)} \tag{A2}$$

and

$$L_2(\alpha) = \frac{2}{\mu_r \dfrac{K_0(\alpha)}{K(\alpha)} + j\cot[K(\alpha)b]}. \tag{A3}$$

The factorization for $L_1(\alpha)$ and $L_2(\alpha)$ is written as

$$L_{1+}(\alpha) = L_{1-}(-\alpha)\frac{1}{e^{-j\pi/4}\sqrt{2}\sqrt{k+\alpha}} \tag{A4}$$

$$L_{2+}(\alpha) = L_{2-}(-\alpha) = \sqrt{L_2(0)}e^{A_+(\alpha)-s} \tag{A5}$$

where

$$A_+(\alpha) = \frac{1}{2\pi i}\int_{-\infty-jc_+}^{\infty-jc_+} \frac{\ln[L_2(\beta)]}{(\beta-\alpha)}d\beta, \tag{A6}$$

and

$$s = \frac{1}{2\pi i}\int_{-\infty-jc_+}^{\infty-jc_+} \frac{\ln[L_2(\beta)]}{\beta}d\beta \tag{A7}$$

The integration contour for $A_+(\alpha)$ and s are modified as follows:

$$A_+(\alpha) = \frac{1}{2\pi j}\int_{k'-jd}^{\infty-jd} \frac{\ln[L_2(\beta)]}{(\beta^2-\alpha^2)}2\alpha d\beta + \frac{1}{2\pi j}\int_{c_2} \frac{\ln[L_2(\beta)]}{(\beta-\alpha)}d\beta \tag{A8}$$

and

$$s = \frac{1}{2\pi i} \int_{c_2} \frac{\ln[L_2(\beta)]}{\beta} d\beta \tag{A9}$$

The contour 'c_2' is shown in Figure A.1. The integral for s and the second integral of $A_+(\alpha)$ are finite integrals which can be evaluated accurately. The integrand of the first term of $A_+(\alpha)$ in (A8) decays as $(1/\alpha)^P$ as $\alpha \to \infty$ and $p>1$, so that the infinite integral can be accurately evaluated to the required precision. In order to factorize $M(\alpha)$, we follow the same procedure as $L(\alpha)$ with

$$M_1(\alpha) = \frac{\mu_r}{-j2K(\alpha)} \tag{A10}$$

$$M_2(\alpha) = \frac{2}{\mu_r \dfrac{K_0(\alpha)}{K(\alpha)} - j\tan[K(\alpha)b]} \tag{A11}$$

The poles of the kernels are obtained by applying the Cauchy integral formula [16] for counting the number of zeros in a domain and iteratively splitting the domain untill the number of zeros in the domain is one. Then, the Cauchy integral formula is applied to obtain the location of the zero. The kernel could be reduced to the form given by Bates [17] as done by Tayyar [18], but there is no advantage in doing so since the Bates expression is useful only when the absolute value of the factors are necessary, in which case the integrals reduce to finite integrals.

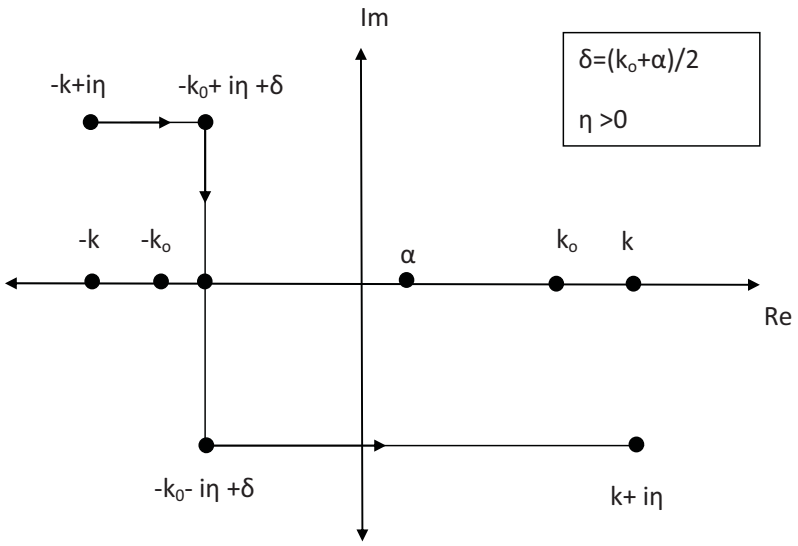

Figure A.1. Contour C_2

The time taken to compute the factors is significantly reduced if we can approximate the infinite integral in (A8) with a finite one. For large α, the kernel Log (L_2 (α)) is approximated by

$$Log(L_2(\alpha)) = \log(1 - e^{-2\alpha b}) - \log(1 + \delta/2) = -e^{-2\alpha b} - \delta/2 \tag{A12}$$

Where

$$\delta = \frac{k^2 - k_0^2}{2\alpha^2} \tag{A13}$$

For large α, the first term becomes very small, and the infinite integral can be reduced to a finite integral and the second term of (A12) when substituted in the infinite integral of (A8) has a closed form solution. The finite integral upper limit that we have used for computation is '100k_o'. The exponential term in (A12) decays faster for a higher value of

‘d’, and therefore, the computation time for the finite integral is inversely proportional to the thickness. A similar procedure can be applied to the other kernel M(α).

APPENDIX B

Consider the integration term in (16a)

$$\frac{\lambda}{2\pi j}\int_{-\infty+ja}^{\infty+ja}\frac{F_+^*(\tau)L_-(\tau)e^{j\tau l}d\tau}{(\tau+\alpha)}=\frac{\lambda}{2\pi j}\int_{-\infty+ja}^{\infty+ja}\frac{F_+(\tau)L_-(\tau)e^{j\tau l}d\tau}{(\tau+\alpha)}$$
$$+\frac{\lambda h e^{-jk_o l\cos\phi_o}}{2\pi j\sqrt{2\pi}}\int_{-\infty+ja}^{\infty+ja}\frac{L_-(\tau)e^{j\tau l}d\tau}{(\tau-k_o\cos\phi_o)(\tau+\alpha)} \qquad \text{(A14)}$$
$$-\frac{\lambda^2 h}{2\pi j\sqrt{2\pi}}\int_{-\infty+ja}^{\infty+ja}\frac{L_-(\tau)e^{j\tau l}d\tau}{(\tau+k_o\cos\phi_o)(\tau+\alpha)}$$

The integration contour of the last term in (A13) is deformed along path P_1+P_2 as shown in Figure 2.2.

$$-\frac{\lambda^2 h}{2\pi j\sqrt{2\pi}}\int_{-\infty+ja}^{\infty+ja}\frac{L_-(\tau)e^{j\tau l}d\tau}{(\tau+k_o\cos\phi_o)(\tau+\alpha)}$$
$$=-\frac{\lambda^2 h}{\sqrt{2\pi}}\sum_{n=1}^{p}\frac{\mathrm{Re}\,s\{L_-(s_n)\}e^{js_n l}}{(s_n+k_o\cos\phi_o)(s_n+\alpha)} \qquad \text{(A15)}$$
$$-\frac{\lambda^2 h}{2\pi j\sqrt{2\pi}}\int_{P_1+P_2}\frac{L_-(\tau)e^{j\tau l}d\tau}{(\tau+k_o\cos\phi_o)(\tau+\alpha)}$$

The integral is then written as

$$-\frac{\lambda^2 h}{2\pi j\sqrt{2\pi}}\int_{P_1+P_2}\frac{L_-(\tau)e^{i\tau l}d\tau}{(\tau+k_o\cos\phi_o)(\tau+\alpha)}=$$
$$-\frac{\lambda^2 h}{2\pi j\sqrt{2\pi}L_+(k)}\int_{P_1+P_2}\frac{L(\tau)e^{j\tau l}d\tau}{(\tau+k_o\cos\phi_o)(\tau+\alpha)}=-\frac{\lambda^2 h\mu_r}{2\pi j\sqrt{2\pi}L_+(k)}* \qquad \text{(A16)}$$
$$\int_{P_1+P_2}\frac{e^{j\tau l}d\tau}{(\tau+k_o\cos\phi_o)(\tau+\alpha)\{-jK_0(\tau)\mu_r+K(\tau)\cot[K(\tau)d]\}}$$

By substituting τ-k_o=ju, $(\tau\text{-}k_o)^{1/2}$=-$u^{1/2}e^{j\pi/4}$ on P_1 and $(\tau\text{-}k_o)^{1/2}$=$u^{1/2}e^{j\pi/4}$ on P_2, the integral in (A16) becomes

$$\int_{P_1+P_2} \frac{e^{j\tau l}d\tau}{(\tau+k_o\cos\phi_o)(\tau+\alpha)\{-jK_0(\tau)\mu_r+K(\tau)\cot[K(\tau)d]\}} =$$
$$\frac{-2j\mu_r e^{jk_o l}e^{j\pi/4}}{(\alpha-k_o\cos\phi_o)}\left[\int_0^\infty \frac{e^{-ul}u^{1/2}\sqrt{2k_o+ju}du}{(k_o+ju+k_o\cos\phi_o)A(u)} - \int_0^\infty \frac{e^{-ul}u^{1/2}\sqrt{2k_o+ju}du}{(k_o+ju+\alpha)A(u)}\right] \quad \text{(A17)}$$

where

$$A(u) = -{\mu_r}^2 ju(2k_o+ju)+[k^2-(k_o+ju)^2]\{\cot[d\sqrt{k^2-(k_o+ju)^2}]\}^2 \quad \text{(A18)}$$

Equation (A15) is then written as

$$-\frac{\lambda^2 h}{2\pi j\sqrt{2\pi}}\int_{-\infty+ja}^{\infty+ja}\frac{L_-(\tau)e^{j\tau l}d\tau}{(\tau+k_o\cos\phi_o)(\tau+\alpha)}$$
$$=-\frac{\lambda^2 h}{\sqrt{2\pi}}\sum_{n=1}^{p}\frac{\mathrm{Re}\,s\{L_-(s_n)\}e^{js_n l}}{(s_n+k_o\cos\phi)(s_n+\alpha)}$$
$$+\frac{\lambda^2 h{\mu_r}^2 e^{jk_o l}e^{j\pi/4}}{\pi\sqrt{2\pi}L_+(k_o)(\alpha-k_o\cos\phi)}* \quad \text{(A19)}$$
$$\left[\int_0^\infty \frac{e^{-ul}u^{1/2}\sqrt{2k_o+ju}du}{(k_o+ju+k_o\cos\phi)A(u)} - \int_0^\infty \frac{e^{-ul}u^{1/2}\sqrt{2k_o+ju}du}{(k_o+ju+\alpha)A(u)}\right]$$

In a similar fashion, we find

$$\frac{\lambda h e^{-jlk_o\cos\phi_o}}{2\pi j\sqrt{2\pi}}\int_{-\infty+ja}^{\infty+ja}\frac{L_-(\tau)e^{j\tau l}d\tau}{(\tau-k_o\cos\phi_o)(\tau+\alpha)}$$
$$=\frac{\lambda h e^{-jk_o l\cos\phi_o}}{\sqrt{2\pi}}\sum_{n=1}^{p}\frac{\mathrm{Re}\,s\{L_-(s_n)\}e^{js_n l}}{(s_n-k_o\cos\phi_o)(s_n+\alpha)}$$
$$-\frac{\lambda h\mu_r{}^2 e^{-jk_o l\cos\phi_o}e^{jk_o l}e^{j\pi/4}}{\pi\sqrt{2\pi}L_+(k_o)(\alpha+k_o\cos\phi_o)}*$$
$$\left[\int_0^{\infty}\frac{e^{-ul}u^{1/2}\sqrt{2k_o+ju}du}{(k_o+ju-k_o\cos\phi_o)A(u)}-\int_0^{\infty}\frac{e^{-ul}u^{1/2}\sqrt{2k_o+ju}du}{(k_o+ju+\alpha)A(u)}\right] \quad \text{(A20)}$$
$$+\frac{\lambda h L_-(k_o\cos\phi_o)}{\sqrt{2\pi}(\alpha+k_o\cos\phi_o)}$$

and

$$\frac{\lambda}{2\pi i}\int_{-\infty+ja}^{\infty+ja}\frac{F_+(\tau)L_-(\tau)e^{j\tau l}d\tau}{(\tau+\alpha)}=\lambda\sum_{n=1}^{p}\frac{F_+(s_n)\,\mathrm{Re}\,s\{L_-(s_n)\}e^{js_n l}}{(\alpha+s_n)}$$
$$-\frac{\lambda F_+(k)\mu_r{}^2 e^{jk_o l}e^{j\pi/4}}{\pi L_+(k_o)}\int_0^{\infty}\frac{e^{-ul}u^{1/2}\sqrt{2k_o+ju}du}{(k_o+ju+\alpha)A(u)} \quad \text{(A21)}$$

APPENDIX C

Using Eqs. (4.2) and (4.8), the tangential magnetic field on the circle $r= a$ for TM excitation can be written as

$$H_\phi = \sum_{n=-\infty}^{\infty} \left\{ -\frac{a_n 2kj}{H_n^{(1)}(ka)\pi ka} e^{jn\phi} + \frac{kH_n^{(1)}{}'(ka)}{H_n^{(1)}(ka)} e^{jn\phi} \times \right.$$
$$\left. \sum_{p=0}^{\infty} (\chi_p^1 + e^{-jn\pi} \chi_p^2) \frac{J_{p+1}(n\pi/2)}{(n\pi/2)} \right\}. \tag{A22}$$

The Hankel function large order form yields the following approximation for the ratio found in (A22) for large n:

$$\frac{kH_n^{(1)}{}'(ka)}{H_n^{(1)}(ka)} \approx -\frac{n}{a}. \tag{A23}$$

Rearranging Eq. (A22), H_ϕ can be given as,

$$H_\phi \approx -\sum_{n=-\infty}^{\infty} \sum_{p=0}^{\infty} (\chi_p^1 + e^{-jn\pi} \chi_p^2) \frac{J_{p+1}(n\pi/2)}{(a\pi/2)} e^{jn\phi}$$
$$-\sum_{n=-\infty}^{\infty} \frac{a_n 2kj}{H_n^{(1)}(ka)\pi ka} e^{jn\phi} + \sum_{n=-L}^{L} \left[\frac{kH_n^{(1)}{}'(ka)}{H_n^{(1)}(ka)} + \frac{n}{a} \right] \times \tag{A24}$$
$$\sum_{p=0}^{\infty} (\chi_p^1 + e^{-jn\pi} \chi_p^2) \frac{J_{p+1}(n\pi/2)}{(n\pi/2)} e^{jn\phi},$$

where L is a positive integer such that the asymptotic value in (A23) is satisfied for any $n > L$. The second and third terms of Eq. (A24) are finite for all values of ϕ. Using Eq.(3.27), the first term in Eq. (A24) may be written as

$$
\begin{aligned}
&-\sum_{p=0}^{\infty} \chi_p^1 \, T_p^1 \left[1-\left\{ \frac{2\phi}{\pi} \right\}^2 \right]^{-\frac{1}{2}} C_{p+1}^0 \left\{ \frac{2\phi}{\pi} \right\} + \\
&-\sum_{p=0}^{\infty} \chi_p^2 \, T_p^2 \left[1-\left\{ \frac{2(\phi-\pi)}{\pi} \right\}^2 \right]^{-\frac{1}{2}} C_{p+1}^0 \left\{ \frac{2(\phi-\pi)}{\pi} \right\}.
\end{aligned}
\tag{A25}
$$

where T_p^1 and T_p^2 are constants independent of ϕ. Eq. (A25) shows that the magnetic field satisfies the required edge conditions.